NORTHWESTERN UNIVERSITY

Linear Decomposition of Atomic Orbitals: Mapping the Electronic Properties of Crystalline Materials

A DISSERTATION

SUBMITTED TO THE GRADUATE SCHOOL

IN PARTIAL FULFILLMENT OF THE REQUIREMENTS

for the degree

DOCTOR OF PHILOSOPHY

Field of Materials Science and Engineering

By

Maxwell T. Dylla

EVANSTON, ILLINOIS

September 2020

ABSTRACT

Linear Decomposition of Atomic Orbitals:

Mapping the Electronic Properties of Crystalline Materials

Maxwell T. Dylla

An extensive set of functional electronic properties depends on the electronic structure. These properties are directly connected to the reciprocal-space representation of electronic structure. However, there is a complementary, real-space perspective that is described by combinations of atomic orbitals. Atomic orbitals are the components of electronic structures, analogous to how elements are the components of crystal structures. To further the analogy, relevant portions of the electronic structure are described by atomic orbital *compositions*. Within a material family, the atomic orbital compositions can explain the variety of electronic structures expressed by each phase. An orbital phase diagram, which maps each phase according to its atomic orbital composition, can differentiate different classes of electronic structure. In thermoelectric applications, the relevant portions of the electronic structure are the valence and conduction band edges (the highest-performing materials are semiconductors). The location, shape, and number of carrier pockets near the band edge determine their transport properties. In light of recent developments in structure-matching algorithms, which can group databases of electronic structure calculations into material families, the orbital phase diagram approach will be useful for identifying promising candidate materials within different structure families. However, since many materials are synthesized as polycrystalline samples, it is important to identify whether the measured properties are a result of the intrinsic electronic structure or micro-structural defects. In particular, grain boundaries can confound the interpretation of the transport properties.

Acknowledgments

I'm eternally grateful to my advisors, colleagues, friends, and family who helped me get this far. I wouldn't have completed my Ph.D. studies without you. Your advice, support, openness, and especially your kindness are the reasons I'm here today. From the bottom of my heart, I sincerely thank you.

To my advisors, thank you for all of your guidance. Jeff, thank you for fostering such a wonderful group environment. You played a major role in my development as a scientist. Scott, Anubhav, Eric, and my committee members, thank you for challenging me to interpret my research in new and creative ways. Finally, thank you Matt. You kindled my interest in research while I was a wee-undergrad and sent me on this path.

To my colleagues, thank you for helping me navigate academic life. The former members of the Snyder group, Stephen, Sanyuki, Thomas, Sam, and Riley, thank you for mentoring me in the ways of the lab. The members from my year, Max, Shash, Ian, and Matthias, thank you for being my constant companions on this journey. The "new" group members, Jimmy, Kazuki, James, Ramya, Moath, and Maddie, thank you for the bright energy you brought to the lab. I continued to learn new things from you. To my colleagues from Berkeley, Alireza, Alex, and Junsoo, you helped me see different perspectives in the field of materials.

To my friends, thank you for keeping me balanced in graduate school. The comp-sci cry-squad, you've been on this journey with me from coursework to graduation. To my family, Tom, Brenda, Tori, Maddie, and Kim, thank you for your unconditional love and support that made all of this possible.

Much of this thesis is formed from reproductions of peer-reviewed articles. The sections on Landauer transport in Chapter 1 are reproduced from *Applied Physics Reviews* 5, 021303 (2018), with the permission of AIP Publishing. Sections on the electronic transport and band structure of $SrTiO_3$ in Chapters 1 and 2 are reproduced from *Angew. Chem.* 131, 5557-5566 (2019), with the permission of Wiley On-line Library. Chapter 3 is reproduced from *Adv. Mater. Interfaces* 1900222 (2019), with the permission of Wiley On-line Library. The sections on half-Heuslers in Chapter 2 are reproduced from an article in preparation.

I would like to acknowledge funding from the National Science Foundation (DMREF-1729487 and DMREF-1333335), which helped support this research and fund my visiting work at Berkeley National Laboratory.

Special thanks to Stephen, who's wordsmithing inspired the title of this thesis.

Table of Contents

List of Figures

1.4 The distinct Fermi surfaces of perovskite oxides heavily influence their transport properties. **a)** Fermi surfaces of $SrTiO_3$ exhibit low-dimensional character, which is exemplified by a highly-elongated shape that intersects the Brillouin zone boundary. **b)** Cylindrical Fermi surfaces capture the low-dimensional character of the band structure, and the intersection of the three cylinders accounts for the two nearly spherical Fermi surfaces observed in (a). This band structure model is distinct from the isotropic (spherical) dispersion typically invoked to convert experimental data to quantities such as effective mass. **c)** The low-dimensional model is consistent with the experimental effective mass of doped $SrTiO_3$ single crystals; it properly reproduces the temperature and carrier dependence of the effective mass extracted from the Seebeck coefficient. Strongly varying effective masses may be a useful experimental signature for identifying other low-dimensional electronic structures in three-dimensional materials. 25

1.5 The two-dimensional density of states of perovskite oxides is responsible for their carrier-density insensitive scattering (solid lines). For reference, the relaxation times of most three-dimensional semiconductors decrease with increasing carrier-density (dashed line). Data for $SrTiO_3$ [9] and $KTaO_3$ [10] are at 200 K. 28

1.6 The two-dimensional Fermi surfaces of perovskite oxides lead to temperature squared resistivity. **a)** The resistivities of $KTaO_3$,[10] $SrTiO_3$,[7,9] and Ba(x)Sr(1-x)TiO_3 [11] are proportional to temperature-squared (except at the lowest carrier-densities, where it is temperature-cubed due to the temperature dependence of the Fermi level). **b)** The relaxation time extracted with the two-dimensional model is dominated by acoustic phonons below room-temperature and optical phonons at higher temperatures. Furthermore, even at low carrier-densities, the relaxation time follows temperature-squared behavior. **c)** The additional source of temperature dependence in the resistivities and relaxation times (T^2 v.s. T^1) comes from their Fermi-surface dimensionality, as the number of accessible final scattering states for electrons (states within the radius of a phonon Bose sphere) increases with increasing

temperature. The additional temperature dependency from increasing final states, along with increasing phonon occupation, leads to temperature-squared resistivity.

2.1 There are three crystallographic sites in the half-Heusler structure: X (blue), Y (red), and Z (green). The Y-site is in a body-centered-cubic coordination environment formed by the X- and Z-sites. The X- and Z-sites are in tetrahedral coordination environments formed by the Y-sites (in the first nearest-neighbor shell) and octahedral coordination environments formed by X- and Z-sites (in the second nearest-neighbor shell).

2.2 **a)** The valence band edges of half-Heusler electronic structures are primarily composed of d-orbitals from the X- and Y-sites, and secondarily, p-orbitals from the Z-site. The relative contributions of these basis orbitals describe the type of carrier pockets observed in this structure family. **b)** Electronic structures with higher concentrations of Z-p orbitals at the band edge have carrier pockets at the W-point with high degeneracy. **c)** Phases with valence band edges dominated by X-d states have carrier pockets at the Γ-point, and **d)** band edges dominated by Y-d states have carrier pockets at the L-point.

2.3 The difference in valence electron configuration (encoded in group number) and electronegativity of the X- and Y-species determines the energy offset between the Γ- and L-points. Engineering the relative energies of these k-points controls the degeneracy (four in the case of L-pockets and one for Γ-pockets).

2.4 The W-point is at or near the valence band maximum for compounds with *both* a Group IV element on the Z-site (Sn, Ge) and a Group IX on the Y-site (Co, Rh, or Ir). Furthermore, in six of the seven W-pocket materials, the L-point is converged within 100 meV of the band edge (total degeneracy of ten).

2.5 The electronic structure of $SrTiO_3$ is described by two-dimensional crystal orbitals, even though the crystal structure is three-dimensional and cubic. **a)** In the unitcell, local Ti-d and O-p orbitals hybridize via covalent bonds; an octahedral crystal field splits the anti-bonding Ti-d states into two subsets. Each hybrid state is visualized by maximally localized Wannier

functions and exhibits strong anti-bonding character in the conduction states and subtle bonding character in the valence states. **b)** Each hybrid orbital state broadens into bands in momentum (k) space when they mix with adjacent unitcells. Crystal orbitals are formed from the mixing of Wannier functions from all crystal sites, and the introduction of a Bloch phase factor between neighboring orbital hybrids specifies a particular k-state. For the lowest-lying conduction bands (labeled by 1 and 2), mixing only exists between t_{2g}^* orbitals of the same x/y/z symmetry. **c)** There are two interactions between adjacent t_{2g}^* orbitals that dictate the strength of dispersion in k-space. **(1)** The strong π-interactions in the plane of each basis orbital give dispersive character to the bands. **(2)** The weak, out-of-plane δ-interactions give non-dispersive character, which is a signature of its low-dimensional electronic structure along the Γ-X directions (parallel to the $\langle 100 \rangle$ family of crystallographic directions).

3.1 Grain boundary resistance has a particular signature in transport data. **a)** The experimental conductivities of polycrystalline $SrTiO_3$ are heavily affected and become activated with temperature in extreme cases of grain boundary resistance (green). **b)** The Seebeck coefficients of polycrystalline samples are not affected by the grain boundary (there is only one sample with a higher carrier concentration, which decreases the magnitude of the Seebeck), and their temperature dependence is the same as single crystal samples. **c)** The degraded conductivities result in lower power factors in polycrystalline samples. **d)** Any doping dependence in the transport properties can be removed by analyzing the weighted mobility, where all polycrystalline samples (dashed) fall below the single crystal properties (solid). Experimental data from red to green:[6,7,11,12]. The polycrystalline samples shown are the median samples from the different grain boundary phases in Figure 3.3a. This set of samples demonstrates the range of expected grain boundary behaviors.

3.2 **a)** The lower oxygen vacancy concentrations ($V_O^{\cdot\cdot}$) in the vicinity of the grain boundary are responsible for grain boundary resistance in $SrTiO_3$ (the vacancy profile reflects the simulated data in[13]). **b)** The depletion of positively charged oxygen vacancies induces a

CHAPTER 1

Modeling Electronic Transport in Thermoelectric Applications

Thermoelectric devices are appealing, solid-state energy conversion technologies because they can operate in two distinct modes—as generators and coolers. Regardless of operating mode, a high-performing thermoelectric material has both a high conductivity (σ) and Seebeck coefficient (α), and a low thermal conductivity (κ). These intrinsic requirements define the figure of merit ($zT = \alpha^2\sigma T/\kappa$) for thermoelectric materials (Appendix A).[23] Developing new thermoelectric materials with higher performance, wider ranges of operating temperatures, and different chemical compatibilities are active areas of research.[7,8,24–30]

The identification of promising thermoelectric materials is accelerated by guidance from first principles calculations.[31–39] Many of these computational efforts have focused on predicting the electronic terms of zT (the power factor, $\alpha^2\sigma$) for bulk materials.[40] Colloquially, materials with high power factors have several, parallel conducting channels for electrons or holes to transport through; these channels should also have high mobility. Materials that meet these requirements have complex Fermi surfaces with multiple carrier pockets, such that the Fermi surface can be used as a visual search strategy for high-performance.[41] The multiplicity of carrier pockets satisfies the requirement for parallel channels, and so long as these carrier pockets have low band effective masses, they will likely have high mobilities. This intuitive, visual description for high performance can be quantified by computing the complexity factor from first principles calculations.[42] The complexity factor is a powerful descriptor for predicting the peak power factor (assuming that the correct carrier concentration can be achieved through doping) and is an effective screening metric for high thermoelectric performance. Materials with complex Fermi surfaces and high complexity factors are among the most promising thermoelectric materials, because of their high power factors (Figure 1.1).[3–5,7]

While electronic transport and thermoelectric performance is intimately tied to the electronic structure, there are several aspects of transport that only depend on the distribution function of the carriers (Fermi-Dirac). It is instructive to first discuss how charge carriers behave in electric fields and temperature gradients without

discussing the details of the electronic structure. Treating transport in a general way at first will help highlight how electronic structure is involved in transport later on. The information carried by the electronic structure is encoded in the *transport function*, which can be treated as a simple function of energy in this analysis. Afterwards, functional forms for the transport function can be derived using a simple toy-model for an electronic band structure. When the electronic structure of a solid significantly deviates from the simple toy-model, our expectations for transport properties will have to be revisited.

1.1. Influence of the Fermi-Dirac Distribution Function on Electronic Transport

To describe transport, we will take the Landauer approach. In 1957, Landauer sought to explain the diffusive transport of charges in disordered metals containing polarizable point defect scattering sources.[43–48] At the time, Boltzmann transport theory was the dominant approach to describe transport in crystalline solids, and Landauer's developments were largely ignored. However, the emergence of nanostructured and molecular electronics in the mid-1980s rekindled interest in Landauer's transport framework.[49–52]

The Landauer approach is easily understood by considering a quantum system where we track the transport of individual charge carriers. As an example, consider a benzene ring attached between two gold electrodes.

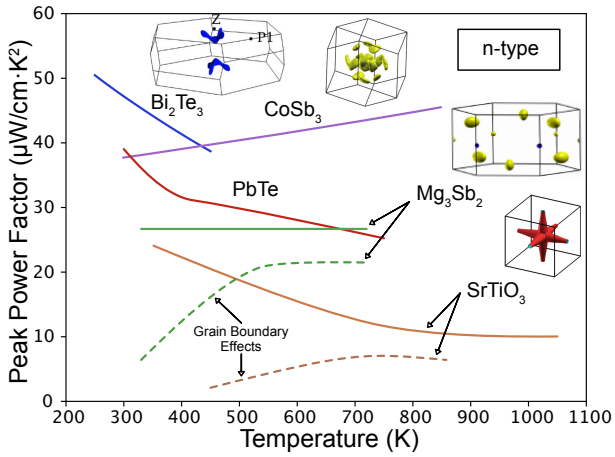

Figure 1.1. The experimental power factors of materials with complex Fermi surfaces are high, but grain boundary resistance can degrade the electronic properties from those predicted by transport models and measured in single crystal samples. Peak power factor at each temperature is assessed from experimental transport properties with an effective mass model.[1] The peak power factor at each temperature corresponds to an optimized carrier concentration. Bi_2Te_3,[2] $CoSb_3$,[3] PbTe,[4] Mg_3Sb_2 (solid line assumes no grain boundary resistance),[5] and $SrTiO_3$ (dashed line[6]).[7] Fermi surfaces adapted from: $CoSb_3$,[3] Mg_3Sb_2.[8]

The Landauer approach specifies boundary conditions at the gold electrodes on either side of the benzene ring: fixed electron chemical potentials μ and temperatures T. The boundary conditions set the electron occupation statistics f of the gold electrodes, which are a function of energy E. As an aside, the Fermi-level E_f is used interchangeably with the electron chemical potential μ in some sources (here, we reserve "Fermi-energy" for 0 K),

$$f(E) = \frac{1}{e^{\frac{E-\mu}{kT}} + 1} \, . \tag{1.1}$$

Transport through the benzene ring occurs via an integer number of *parallel transport channels*, $M(E)$, with well-defined *transition probabilities*, $T(E)$, through the channels. The current is given by a sum over the transitions, weighted by the difference in occupation statistics between the electrodes. Electrons are always hopping in both directions; there is only a net current, I, if the electron occupation is higher at one electrode ($\Delta f = f_2 - f_1 \neq 0$) so that there are more particles making transitions from that electrode,

$$I = -\frac{2q}{h} \int_{-\infty}^{\infty} T(E) M(E) \Delta f dE \, . \tag{1.2}$$

The transport between the reservoirs can be modeled as ballistic, diffusive, or anywhere in between by tuning the transition probability.

Extending the Landauer approach to bulk systems involves considering the current density, J, through an infinitesimal slice of bulk material. The finite difference in particle occupation statistics becomes a *gradient* in occupation ∇f, induced by a gradient in chemical potential or temperature. The transport channels and their associated transition probabilities ($T(E)$ and $M(E)$) can be combined into a positive-valued, *energy-dependent transport function* $G(E)$,

$$J = -q \int_{-\infty}^{\infty} G(E) \nabla f dE \, . \tag{1.3}$$

Note that the charge associated with a carrier q includes its sign (e.g., q for an electron is $-e$). This equation can be generalized to treat more than just charge transport by electrons. The current density, J, in Eq. 1.3 is the product of a particle flux and the charge per particle q; we can treat the heat flux from charge carriers by considering the heat carried per particle. In addition, Eq. 1.3 is applicable to more than just electrons; if the suitable particle distribution function is used, the equation is equally valid for fermions, bosons, and Boltzmann-like

particles. Therefore, we can treat more than just conductivity and the Seebeck coefficient with Landauer theory; contributions to the thermal conductivity from electrons and vibrational quanta are accessible (Appendix B).

Without specifying any material details—metal or semiconductor, crystalline or amorphous—we can begin to understand charge transport induced from electric fields and temperature gradients; these gradients will induce gradients in the particle distribution function, which drives transport. Derivations in these sections will focus on understanding the underlying transport of measurable quantities such as conductivities and the Seebeck coefficient without specifying any functional form for $G(E)$. In all cases, we will see that transport can be understood from gradients in particle occupation statistics.

1.1.1. Charge transport in an electric field

Characterizing electronic transport induced from electric fields is a typical situation in a thermoelectric laboratory; conductivity measurements are carried out by applying a voltage across a sample at isothermal conditions. An external bias results in a gradient in the electron chemical potential ($\nabla\mu = q\nabla V$), which in turn induces a gradient in the electron occupation statistics. The electron distribution functions near the contacts of a sample under applied bias (at isothermal conditions) are depicted in Fig. 1.2a. The high energy states near contact two have a greater occupation than those states near contact one. The difference in electron occupation constitutes a driving force to transfer electrons from contact two to contact one.

If we can find a relationship between the spacial gradient of the occupation statistics ($\nabla f = \partial f/\partial x$) and the spacial gradient of the electron chemical potential ($\nabla\mu = \partial\mu/\partial x$), we can determine the current density induced by an applied voltage. A chain rule relates the gradient of the occupation statistics and the gradient of the chemical potential ($\partial f/\partial x = \partial f/\partial\mu \cdot \partial\mu/\partial x$). However, it is far more convenient to formulate the derivative of the carrier statistics with respect to energy, E, instead of chemical potential μ, since the integral for current density is over energy-space. The derivative of the Fermi-Dirac function (Eq. 1.1) with respect to chemical potential and energy are opposite in sign ($\partial f/\partial\mu = -\partial f/\partial E$). Therefore, a succinct chain-rule relates the spacial gradient of the occupation statistics and the spacial gradient of chemical potential ($\nabla f = -\partial f/\partial E \cdot \nabla\mu$); applying this chain-rule to the general current density equation informs us how a material responds to an applied

voltage,

$$J_{\nabla V} = -q^2 \nabla V \int_{-\infty}^{\infty} G(E) \frac{-\partial f}{\partial E} dE \ . \tag{1.4}$$

The negative derivative of the Fermi-Dirac function (see Fig. 1.2) and $G(E)$ are positive-valued functions. This means that current flows down a voltage gradient regardless of material type (i.e., metal, n/p-type semiconductor, or insulator). The details of $G(E)$ and the temperature determine the magnitude of the current density.

Conductivity is the thermoelectric property of interest when we apply a voltage to a sample. Ohms law ($J = -\sigma \nabla V$) relates the current density to the magnitude of the applied bias,

$$\sigma = q^2 \int_{-\infty}^{\infty} G(E) \frac{-\partial f}{\partial E} dE \ . \tag{1.5}$$

A material's conductivity, σ, is always positive regardless of whether a semiconductor is n- or p-type. The derivative of the electron distribution function ($-\partial f / \partial E$) acts as a *selection function* that determines which

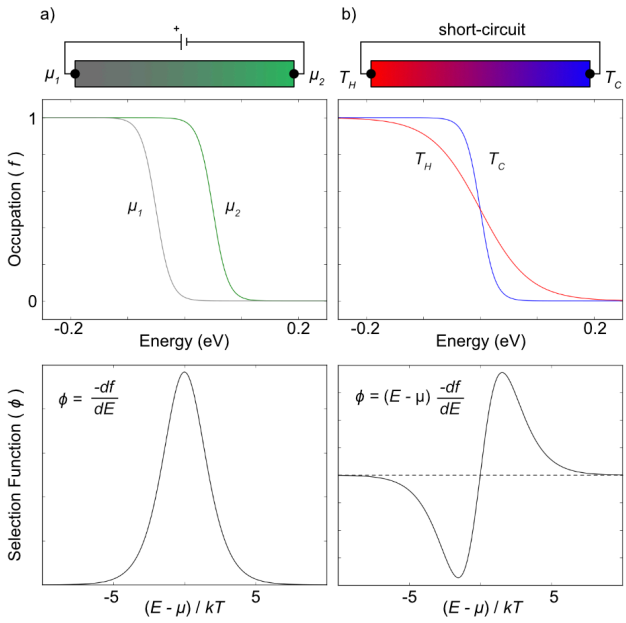

Figure 1.2. a) A gradient in chemical potential shifts the Fermi-Dirac distribution. The infinitesimal difference between neighboring occupations is positive for all carrier energies. Transport proceeds down the chemical potential gradient. b) In contrast, a temperature gradient changes the curvature of the Fermi-Dirac distribution. The selection function is odd around the chemical potential. Carriers above the chemical potential diffuse from hot to cold, while carriers below flow in opposition.

carriers are involved in transport (see Fig. 1.2). At high temperatures, particles in a wider energy range participate in transport.

1.1.2. Charge transport in a temperature gradient

The Seebeck effect is a phenomenon where a temperature gradient in a material induces a voltage gradient. Applying a temperature gradient across a sample and measuring the induced voltage in an *open-circuit* condition defines the Seebeck coefficient, α. There are two driving forces for carrier transport during a Seebeck measurement: a temperature gradient and the induced voltage gradient. In the linear regime, we can treat the current density from these two stimuli additively. To understand the Seebeck measurement, we need to first understand transport induced from a temperature gradient in a *short-circuit* condition (i.e., the electron chemical potential is constant throughout the sample).

1.1.2.1. Short-circuit condition. Applying a temperature gradient to a sample induces a gradient in the carrier occupation statistics; with increasing temperature, the carrier distribution function broadens around the electron chemical potential. The carrier occupation statistics near the contacts of a sample in a temperature gradient (under *short-circuit* conditions) are depicted in Fig. 1.2b. Regions of the sample at high temperature have more electrons occupying high energy states, and fewer occupying low energy states; there is thus a driving force to transfer high energy electrons from hot to cold, and low energy electrons from cold to hot. This intuitive picture will be confirmed below by Landauer theory.

Again we use a chain rule to relate the spacial gradient of the occupation statistics with the spacial gradient of the temperature ($\nabla f = \partial f/\partial T \cdot \nabla T = (E-\mu)/T \cdot -\partial f/\partial E \cdot \nabla T$). Using Eq. 1.3, the Landauer solution to current density induced from a temperature gradient becomes:

$$J_{\nabla T} = -q\nabla T \int_{-\infty}^{\infty} G(E) \left(\frac{E-\mu}{T}\right) \frac{-\partial f}{\partial E} dE. \tag{1.6}$$

While the negative derivative of Fermi-Dirac function and $G(E)$ are positive-valued functions, $\frac{E-\mu}{T}$ is an odd function around the electron chemical potential (see Fig. 1.2b). An electron above the chemical potential will transport from hot-side to cold-side, while electrons with energies less than the chemical potential will transport

from cold-side to hot-side. This asymmetry allows us to distinguish n- or p-type semiconductors; the electrons in n-type transport are predominantly above the chemical potential, while the opposite is true for p-type materials.

A temperature analog to Ohm's law ($J = -\nu\nabla T$) relates the current density to the magnitude of the temperature gradient.

$$\nu = q\int_{-\infty}^{\infty} G(E)\left(\frac{E-\mu}{T}\right)\frac{-\partial f}{\partial E}dE \tag{1.7}$$

The intensive, material quantity, ν, is an Onsager coefficient that determines the current response from a temperature gradient. Materials may respond differently depending on the nature of $G(E)$. If $G(E)$ is symmetric around the chemical potential, there will be no net current. The *selection function* for transport from a temperature gradient is $(E-\mu)\cdot(-\partial f/\partial E)$. Most of the carriers involved in transport will have energies 1.5 k_BT above or below the chemical potential (Fig. 1.2). It is important (though somewhat unfortunate) that the energy range for temperature driven transport overlaps with the voltage driven transport.

1.1.2.2. Open-circuit condition. Having derived transport from a temperature gradient under short-circuit conditions, we can now revisit the Seebeck effect where both temperature and voltage gradients are present in a material. In the linear regime, the current densities induced by the temperature and voltage gradients are additive. Historically, these two contributions were termed the diffusion and drift currents, respectively,

$$J = J_{\nabla T} + J_{\nabla V} = -\nu\nabla T - \sigma\nabla V\ . \tag{1.8}$$

A Seebeck measurement is defined at open-circuit conditions where the net current density is zero ($J = 0$). The Seebeck coefficient, α, is given by the ratio of the voltage difference and the temperature difference through the thickness, l, of the sample,

$$\alpha = -\frac{\Delta V}{\Delta T} = -\frac{l\nabla V}{l\nabla T} = \frac{\nu}{\sigma}\ . \tag{1.9}$$

Recall that ν and σ determine how readily a material responds to a temperature and voltage gradient, respectively. From Eq. 1.9, we see that materials with a large Seebeck coefficient respond more readily to a temperature gradient than an electric field. To have an ideally large Seebeck, a material would not respond to an electric field at all. However, it is impossible for electrons in a real material to respond to a temperature gradient and not a

voltage gradient because the carriers involved in the two transport processes are in overlapping energy ranges; this is apparent when one examines the selection functions in Fig. 1.2.

1.2. Connection between Electronic Structure and Transport Properties

In the previous sections, we found that carriers in particular energy ranges set by selection functions are involved in transport. Now, we will explore the role of the energy-dependent transport function $G(E)$ in determining both conductivity and the Seebeck coefficient in crystalline materials. First, we need to explore the microscopic origins of $G(E)$. Throughout this section, we will examine crystalline materials in the diffusive transport regime; different material classes may have different functional forms for $G(E)$.

1.2.1. The energy-dependent transport function

In crystalline materials, $G(E)$ can be derived from the band structure and scattering theory. To determine $G(E)$, we must consider the collective motion of all the particles at a given energy. Conveniently, the band structure organizes all of the particles by energy in reciprocal space. Each particle travels with a group velocity determined by the slope of the band structure ($v_g = \partial E/\partial k$) in the transport direction. If we consider the average squared-velocity $\langle v^2 \rangle$ of the particles at a given energy, then we can account for their collective transport with the density of states g. On average, each particle scatters after a characteristic relaxation time τ (Appendix C). The diffusivity of each individual particle is described by $\langle v^2 \rangle \tau$. $G(E)$ is the sum of the individual particle diffusivities, since transport occurs in parallel conducting channels.

$$G(E) = \langle v(E)^2 \rangle \tau(E) g(E) \tag{1.10}$$

In crystalline inorganic materials, band edges are modeled as spherical carrier pockets with a parabolic dispersion. The dispersion curvature is parameterized by an effective mass m^* ($E = \hbar^2|k|^2/2m^*$). This model is referred to as the single parabolic band or effective mass model[53] and determines the energy dependence of both the average velocity $\langle v^2 \rangle$ and density of states, g, in $G(E)$. Qualitatively, the *slope* of the parabolic dispersion increases into the band, so $\langle v^2 \rangle$ must be an increasing function; the *surface-area* of the spherical pocket also increases into the band, so g must be an increasing function. Specifically, $\langle v^2 \rangle$ increases linearly into a band, while g increases

as the square-root of energy. At temperatures greater than 300 K, the relaxation time, τ, is typically limited by phonon scattering, which scales inversely with g. Since the energy dependence of g and τ cancel, the electron energy-dependent transport function is linear ($G_{el}(E) = G_0 \cdot E$). Fig. 1.3 depicts the constituent terms in G(E).

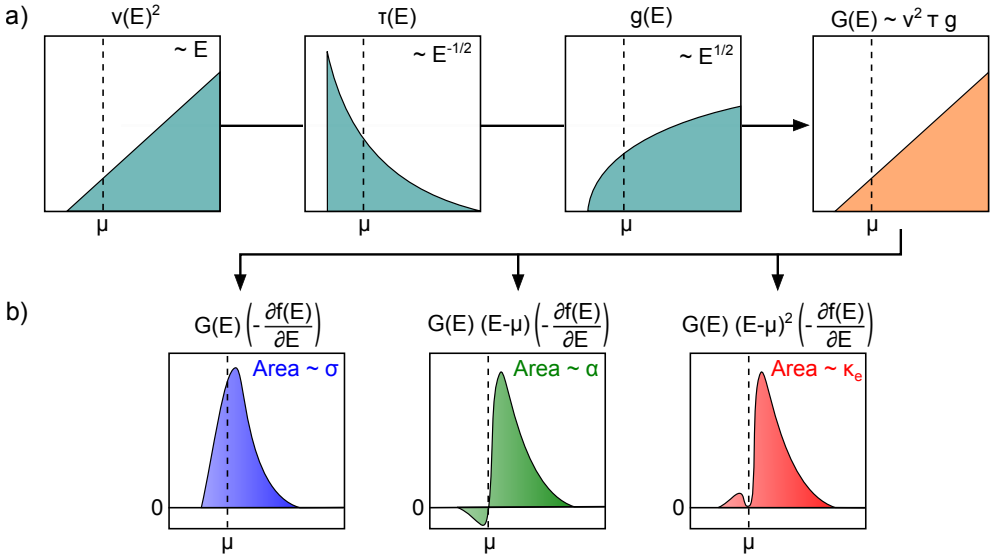

Figure 1.3. a) For a crystalline semiconductor, the energy dependence of the transport function $G(E)$ is derived from its constituent terms. A spherical, parabolic band edge determines the charge carrier group velocity (v) and density of states (g). The energy dependence of electron-phonon relaxation times (τ) is inversely proportional to g. b) The convolution of $G(E)$ with selection functions determines thermoelectric transport coefficients: including, conductivity σ, the Seebeck coefficient α, and the electronic contribution to thermal conductivity κ_e.

1.2.2. Location of the Fermi Level

Now that we have a functional form for $G(E)$, we can see how it interacts with selection functions to produce the variety of transport properties seen in metals, insulators, and semiconductors. Since $G(E)$ is zero inside of a band gap, the most important difference between these three classes of materials is the proximity of a band gap to the electron chemical potential. As we will see, the chemical potential should be located near a band edge to maximize power factor.

1.2.2.1. Insulators/Semiconductors. The electron chemical potential in insulators and semiconductors is located in proximity to a band gap. The difference between insulators and semiconductors is the size of the band gap. When either material is degenerately doped, the electron chemical potential resides just inside the band edge

(as illustrated in Fig. 1.3). The voltage induced selection function (conductivity) partially samples the band edge. Only half of the temperature induced selection function (Seebeck coefficient) samples the band edge; since the temperature selection function is odd, this prevents transport cancellation between electrons above and below the chemical potential. In this configuration, we get both high Seebeck coefficient and sufficiently high conductivity. Materials with the electron chemical potential near a band edge tend to make the best thermoelectric materials due to the compromise between temperature and voltage driven transport. Optimizing the location of the chemical potential with respect to the band edge optimizes the power factor.

1.2.2.2. Metals. By contrast, the electron chemical potential in metals is deep inside a band. As a result, the voltage selection function samples $G(E)$ where it is largest. However, the temperature selection function induces cancellation between carriers below and above the chemical potential. While the conductivity of metals tends to be high, their low Seebeck coefficients make them poor thermoelectric materials. In addition, a metal's electronic contribution to the thermal conductivity is high because carriers on both sides of the chemical potential are contributing.

1.2.3. Parameterization of High Power Factor

An important quantity for thermoelectric device performance is the power factor, $\alpha^2\sigma$. Mathematically, we can write the power factor in terms of the Onsager coefficients (ν and σ) that we derived in previous sections. A material's power factor is a competition between temperature (the numerator) and voltage (the denominator) driven transport,

$$\alpha^2\sigma = \frac{\left[\int_{-\infty}^{\infty} G(E)\left(\frac{E-\mu}{T}\right)\frac{-\partial f}{\partial E}dE\right]^2}{\int_{-\infty}^{\infty} G(E)\frac{-\partial f}{\partial E}dE}\ . \tag{1.11}$$

We have established that placing the electron chemical potential near a band edge optimizes a material's power factor; this placement offers a compromise between the temperature/voltage driven transport integrals in Eq. 1.11. However, experimentally-realized optimum power factors are highly variable between material systems. The slope (G_0) of $G(E)$ explains the wide range of power factors observed experimentally. Examine Eq. 1.11, G_0 can be pulled from the integrals since it is energy-independent. Optimized power factor is roughly proportional to G_0, the slope of the transport function. In the thermoelectric literature this constant is refered to

interchangably as the weighted mobility, $\mu_0 \left(m^*/m_e\right)^{3/2}$, or sigma-sub-E-not, σ_{E_0}.[54] While μ can be tuned by doping, the transport function is material dependent, and can thus be controlled by clever design of the band structure.

1.3. Anomolous Transport Properties From Low-Dimensional Electronic Structures

The band structures of many perovskite oxides deviate considerably from the isotropic dispersion assumed in the previous section. Therefore, we will need to revisit some of our expectations for transport in these systems. While these systems still have a linear transport function, we will need to revisit how to interpret effective mass and the relaxation time. A new toy-model for the band structure will help us understand the experimental transport properties (Appendix D). The Fermi-surfaces of this band structure are cylinders as opposed to spheres. This band structure is in essence, two-dimensional, since there is no dispersion along the length of the cylinder.

Perovskite oxides span numerous compositions and are heavily studied as materials for catalytic,[55–58] fuel cell,[59–62] thermoelectric,[63–66] and oxide electronics.[67–70] $SrTiO_3$ is a particularly promising candidate for electronics, because it supports two-dimensional electron gases at its surfaces and interfaces,[71–73] which may lead to new device applications.[74] In many of the aforementioned applications, perovskite oxides are n-type electronic conductors with a tunable carrier-density, but they can also be made insulating or as p-type conductors.[75] Understanding their mobility-limiting scattering mechanism is crucial for engineering their transport properties.

The discussion of electron scattering in perovskite oxides centers on the peculiar temperature dependence of the electrical resistivity, which is not well understood. While the resistivities of typical heavily-doped semiconductors and metals are proportional to temperature,[76,77] the resistivities of many perovskite oxides ($SrTiO_3$,[9,78,79] $SrMoO_3$,[80] $KTaO_3$,[10] $SrNbO_3$,[81] and $SrCoO_3$)[82] are proportional to temperature-squared (T^2). Electron-electron scattering, which is known to give T^2 at low temperatures in strongly correlated materials, is typically invoked to explain the anomalous temperature dependence.[83] If the results of low temperature experiments are analyzed in isolation, electron-electron scattering may be a sufficient explanation for T^2 behavior. However, T^2 resistivity persists above room temperature in many perovskite oxide semiconductors,[7,9–11] which calls into question whether electron-electron scattering is truly the dominant mechanism in these materials. Furthermore, recent first principles calculations have indicated that transport is dominated by electron-phonon scattering.[84,85]

The peculiar T^2 resistivity can be explained by the remarkable Fermi surfaces of the d-bonding perovskite oxides (other perovskite oxides, such as $BaSnO_3$, do not share these features). These Fermi surfaces are assemblies of ellipsoids with high aspect ratios that are nearly cylindrical (they are often described as "warped" or having a "jack" shape), can intersect the Brillouin zone boundary at low energies in high carrier density samples, and are distinct from the Fermi surfaces invoked in standard transport models for semiconductors and metals, from which the expectation of linear-temperature resistivity originates. Cylindrical Fermi surfaces reflect the low-dimensional electronic structures of these materials, which is discussed in the literature but not included in transport analyses of bulk samples.[86] Low-dimensional Fermi surfaces explain several other transport phenomenon in addition to T^2 resistivity, such as the temperature and carrier-density dependence of the effective mass and the carrier-density dependence of scattering.

1.3.1. A Low-Dimensional Fermi-Surface Model

The transport properties of semiconductors are typically characterized by an effective mass. The effective mass relates experimental transport properties to the band-edge electronic structure. For semiconductors with simple, nearly-spherical Fermi surfaces, an isotropic mass (m^*) is often sufficient to describe the transport properties.[1,87] However, the Fermi surfaces of perovskite oxides are more complicated, and the effective mass description must reflect the anisotropic Fermi surfaces of the three sets of t_{2g}^* states. From the preceding chemical analysis, the effective mass in one direction (the δ-interaction direction) should be heavier than the other two, which are comparatively lighter because of the strong π-interactions ($m_h \gg m_l$). The carrier pockets described by this anisotropic description are prolate, ellipsoidal carrier pockets.

$$E_{xy} = \frac{\hbar^2 \left(k_x^2 + k_y^2\right)}{2m_l} + \frac{\hbar^2 k_z^2}{2m_h} \tag{1.12}$$

The anisotropic limit of this carrier pocket ($m_h \to \infty$ when the δ-interactions are negligible) captures the cylindrical shape of $SrTiO_3$ Fermi surfaces, which intersect the Brillouin zone boundary at energies close to the conduction band edge energy (Fig. 1.4a).

A cylindrical Fermi surface has two-dimensional character, since the $E - k$ relationship now only depends on the k-vector in two of the three dimensions. The absence of dispersion in one direction leads to an electron

density-of-states (DOS) that is independent of energy, like a free electron in two dimensions. Energy independent DOS is a signature of low-dimensional electronic structures, and is qualitatively different than a typical three-dimensional DOS, which is proportional to the square-root of energy. The energy dependence of the DOS is reduced in the perovskite oxides, because the number of states in the heavy mass direction saturates once the Fermi surface intersects the Brillouin zone boundary.

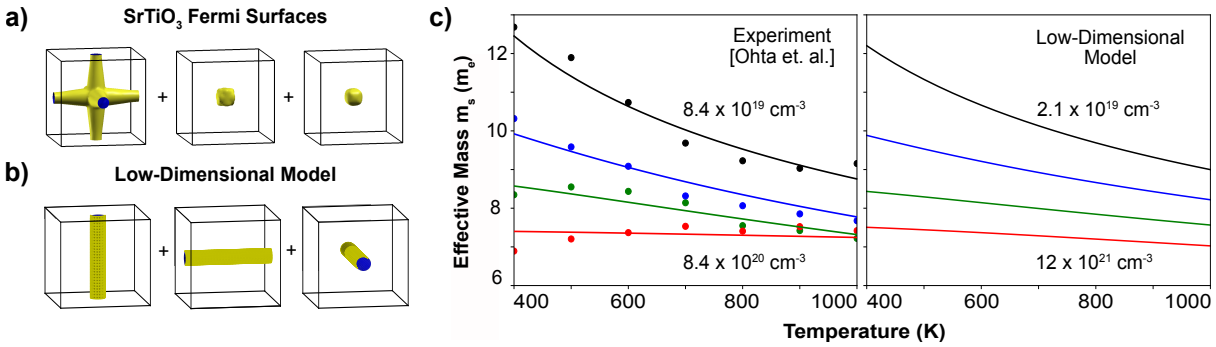

Figure 1.4. The distinct Fermi surfaces of perovskite oxides heavily influence their transport properties. **a)** Fermi surfaces of $SrTiO_3$ exhibit low-dimensional character, which is exemplified by a highly-elongated shape that intersects the Brillouin zone boundary. **b)** Cylindrical Fermi surfaces capture the low-dimensional character of the band structure, and the intersection of the three cylinders accounts for the two nearly spherical Fermi surfaces observed in (a). This band structure model is distinct from the isotropic (spherical) dispersion typically invoked to convert experimental data to quantities such as effective mass. **c)** The low-dimensional model is consistent with the experimental effective mass of doped $SrTiO_3$ single crystals; it properly reproduces the temperature and carrier dependence of the effective mass extracted from the Seebeck coefficient. Strongly varying effective masses may be a useful experimental signature for identifying other low-dimensional electronic structures in three-dimensional materials.

The combination of the three orthogonal, anisotropic carrier pockets results in isotropic electrical conductivity and Seebeck coefficients. For example, the isotropic conductivity is the sum of conductivities from two pockets in the light mass direction and one pocket in the heavy mass direction ($\sigma = 2\sigma_l + \sigma_h$). Since the charge carrier group velocity ($v_g \propto \partial E/\partial k$) is zero in the heavy mass direction, only two cylinders effectively contribute to transport ($\sigma = 2\sigma_l$) along each crystallographic axis. Combining the three, anisotropic carrier pockets leads to isotropic transport behavior but does not affect the energy dependence of the DOS, which remains a constant. A low-dimensional, three-cylinder model (Fig. 1.4b) reflects the interwoven, crystal orbital sheets that form the conduction band states of many perovskite oxides (Fig. 2.5c). Each cylindrical band of states is formed from one t_{2g}^* crystal orbital.

Perovskite oxides are not the only compounds with this peculiar band-edge structure; first principle calculations have shown that some Heusler compounds share these features.[88] As in the perovskite oxides, low-dimensional features in the Heusler compounds are attributed to d-orbital chemistry, so there may be even more structure families with these low-dimensional features. The transport coefficients of the three-cylinder band model are derived in the SI, and might be useful when modeling the transport properties of Heuslers in addition to perovskite oxides.

1.3.2. 2D Transport in Bulk Perovskite Oxides

A two-dimensional electronic structure explains many of the unconventional trends in transport properties observed in semi-conducting perovskite oxides. It explains the dependence of the experimental effective masses on temperature and carrier concentration, the carrier-density dependence of scattering, and the temperature dependence of resistivity. The measurements that characterize these anomalous properties are direct-current or stationary transport studies of n-type materials, in which $SrTiO_3$ is a band conductor.[89] Deformation potential phonon scattering[90] is successful in modeling all three of these experimental transport properties, which suggests that electron-phonon scattering limits the intrinsic mobility of single crystalline $SrTiO_3$ and other perovskite oxide semiconductors with d-p hybridization. While $SrTiO_3$ can exhibit a polaron transport response at very low carrier-densities in very pure samples[91] and in optical measurements,[92] the properties studied here are overwhelmed by band transport. Furthermore, grain boundaries in polycrystalline samples can cause deviations from the transport responses characterized here for single crystal samples.[93]

1.3.2.1. Effective Mass Behavior. The concept of "effective mass" is useful for connecting experimental transport properties to the properties of an underlying electronic structure. For example, the Seebeck effective mass (m_s^*) aggregates the Seebeck coefficient and carrier-density into one term that characterizes the density of states effective mass of electronic charge carriers. The Seebeck mass is the effective mass that reproduces the experimental Seebeck and carrier concentration using a simple, three-dimensional, free-electron model (a single, isotropic, parabolic, rigid band model).[1,87] If a system is described well by a three-dimensional free-electron model (such as most common metals and semiconductors), then the Seebeck mass will be largely constant for different temperatures and charge carrier concentrations. Changes in the extracted effective mass with temperature or

carrier-density can signal that the underlying band structure is different. In the case of $SrTiO_3$ and perovskite oxides in general, these changes (Fig. 1.4c) can be modeled by their assembly of two-dimensional, cylindrical Fermi surfaces.

The Seebeck masses of doped $SrTiO_3$ single crystals were determined in this way using carrier concentrations estimated from the chemical doping concentrations (either Lanthanum or Niobium).[7] The Seebeck mass decreases with increasing temperature and carrier concentration (Fig. 1.4c). Theoretical transport from a three-cylinder model validates that this complex behavior is explained by the low-dimensional electronic structure. When calculating the theoretical transport, an energy-independent relaxation time was used, the cylindrical length was set by the experimental lattice constant ($l = 2\pi/a = 1.6 \cdot 10^{10}$ m^{-1}), and an effective radial mass (m_l) of 1.5 m_e was estimated by fitting the experimental transport properties. The carrier and temperature dependent Seebeck mass observed in the experimental data is captured by the low-dimensional band model (Fig. 1.4c). A strongly temperature and carrier dependent Seebeck mass (or any other experimentally determined effective mass) is a useful experimental signature for identifying low-dimensional electronic structures in three-dimensional materials. Changing effective masses in these cases do not correspond to a changing band curvature.

1.3.2.2. Carrier-Density Dependence of Scattering. The underlying two-dimensional DOS of perovskite oxides can also explain unusual aspects of their electron scattering. Hall effect measurements of electron-doped $SrTiO_3$ demonstrate that phonon scattering is dominant at temperatures greater than 10 K.[94] In the phonon-dominated regime, the relaxation time is largely independent of carrier-density.[95] This anomalous behavior is qualitatively different from the behavior of typical three-dimensional semiconductors and metals, where the relaxation time decreases with increasing carrier-density.[76,77] For both $SrTiO_3$ and $KTaO_3$, the same trend in scattering frequency is observed from analyzing a combination of the Seebeck coefficient and conductivity;[89] the relaxation time of each material is found to be largely independent of carrier-density (Fig. 1.5).

The three-cylinder transport model predicts that the relaxation time should be independent of carrier-density. To understand this result, it is important to recognize that transport measurements investigating scattering only probe the behavior of electronic carriers near the Fermi level (E_f), which shifts in response to changes in carrier-density. For example in an n-type semiconductor, increasing the carrier-density increases the Fermi level. Therefore, transport measurements of samples with different carrier-densities measure the relaxation time

(τ) of electronic carriers at different energy levels. For materials dominated by non-polar phonon scattering (deformation potential scattering), the relaxation time is inversely proportional to the electron density of states (g) at the Fermi level,[90] because the density of states determines the number of states a given electron can scatter into. In a three-dimensional material ($g \propto E^{1/2}$), the relaxation time decreases with increasing carrier-density ($\tau \propto E_f^{-1/2}$). However, the two-dimensional density of states of perovskite oxides ($g \propto E^0$) makes the relaxation time insensitive to carrier-density, since the density of states does not change with Fermi level position.

$$\tau_{2D}\left(E_f, T\right) = \tau_0\left(T\right) \tag{1.13}$$

The absolute magnitude of the relaxation time (τ_0) physically depends on the temperature, primarily through the number of excited phonons (proportional to temperature at high temperatures). However, the temperature dependency can be quite complicated at lower temperatures, where all the scattering phonons modes are not appreciably excited.

1.3.2.3. Temperature-Squared Resistivity. The two-dimensional Fermi surfaces of d-bonding perovskite oxides explain the anomalous temperature dependence of their resistivity. This resistivity is typically proportional to T^2 (which is typically associated with electron-electron scattering at low temperatures)[83] and is quite ubiquitous in metallic perovskite oxides.[10,78–81] In many semi-conducting compounds including $SrTiO_3$,[7,9] $KTaO_3$,[10]

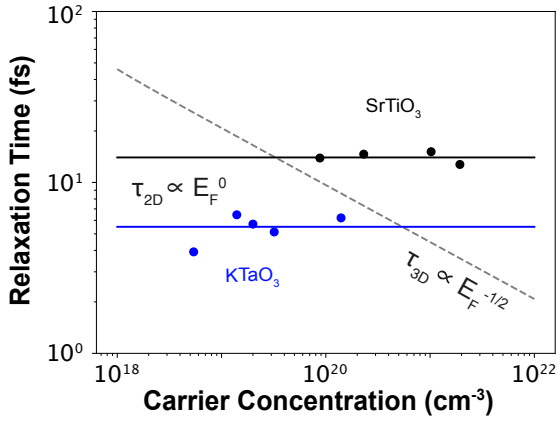

Figure 1.5. The two-dimensional density of states of perovskite oxides is responsible for their carrier-density insensitive scattering (solid lines). For reference, the relaxation times of most three-dimensional semiconductors decrease with increasing carrier-density (dashed line). Data for $SrTiO_3$ [9] and $KTaO_3$ [10] are at 200 K.

and Ba(x)Sr(1-x)TiO_3 solid-solutions[96] this behavior persists to high temperatures (Fig. 1.6a), where phonon scattering dominates transport and electron-electron interactions are expected to be comparably weaker.[94] There is a slight carrier-density dependence to the temperature dependency, where the resistivity is T^3 at the lowest carrier-densities (see the most resistive $KTaO_3$ sample in Fig. 1.6a and).[97] Application of the three-cylinder model to Seebeck-conductivity data shows that all of these samples (including the lowest carrier-density samples) have a T^2 relaxation time (Fig. 1.6b). For high carrier-density samples, the classic Drude model ($\rho^{-1} = ne^2\tau/m^*$) illustrates how the relaxation time is inversely related to the resistivity. For the low carrier-density samples, the additional temperature dependence in the resistivity originates from the Fermi level shifting with temperature, since the Fermi level is more sensitive to temperature at low carrier-densities. The T^3 resistivity at low carrier-densities has also been explained through first principles calculations of electron-phonon coupling, which is consistent with our model interpretation.[85] The relaxation times of all $SrTiO_3$ and $KTaO_3$ samples are the same within each compound, and the relaxation times of Ba(x)Sr(1-x)TiO_3 samples change monotonically through the solid solution. The shorter relaxation times at the $BaTiO_3$ end of the solid-solution are likely due to stronger electron-phonon coupling in $BaTiO_3$. The relaxation times extracted for $SrTiO_3$ at 300 K are similar in magnitude to those calculated in first-principles simulations of electron-phonon scattering.[84]

Several discussions in the literature suggest that elongated Fermi surfaces, such as those observed in elemental Bismuth,[98] can induce T^2 scattering and resistivity through electron-phonon interactions.[89,99,100] Typically, the scattering rate from electron-phonon scattering is expected to be proportional to temperature, because the number of phonons ($n_q \sim kT$) increases linearly with temperature.[76,77] At high temperatures, where all phonons have nearly equal occupation (above the Debye temperature), this leads to electrical resistivity proportional to T^1. However at lower temperature, when not all phonon modes are equally available for scattering electrons, additional temperature dependencies arise. At a given temperature, only phonon modes with energy less than the thermal energy are substantially occupied ($q_{thermal} = kT/v_s$); these phonons occupy a volume of *k*-space enclosed in a Bose sphere with radius $q_{thermal}$. The phonons can scatter an electron on the Fermi surface into another electron state on the Fermi surface enclosed within the radius of the Bose sphere (centered on the initial electron state, Fig 1.6c). Due to increasing temperature, the radius of the Bose sphere increases, which increases the number of accessible final electron states (n_{final}) and therefore increases the scattering. For cylindrical

Fermi surfaces, when the radius of the Bose sphere is greater than the cylindrical radius, the number of final states increases linearly with $q_{thermal}$, which is roughly along the linear dimension of the cylinder. The combined temperature dependencies from phonon occupation and the number of accessible final, scattered states results in temperature squared scattering rates ($\tau^{-1} \sim n_q \cdot n_{final} \sim T^2$). As the temperature increases and the phonon energy exceeds that of the acoustic branch, the dispersive optical modes then extend the T^2 temperature

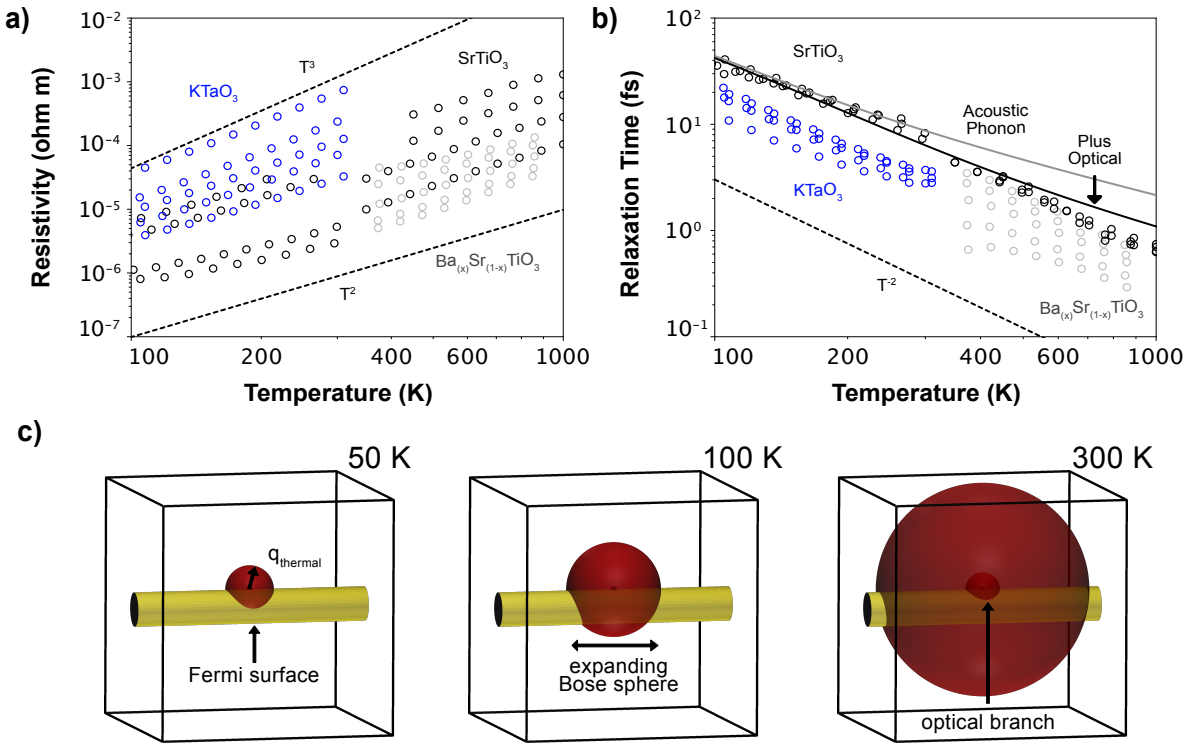

Figure 1.6. The two-dimensional Fermi surfaces of perovskite oxides lead to temperature squared resistivity. **a)** The resistivities of $KTaO_3$,[10] $SrTiO_3$,[7,9] and Ba(x)Sr(1-x)TiO_3 [11] are proportional to temperature-squared (except at the lowest carrier-densities, where it is temperature-cubed due to the temperature dependence of the Fermi level). **b)** The relaxation time extracted with the two-dimensional model is dominated by acoustic phonons below room-temperature and optical phonons at higher temperatures. Furthermore, even at low carrier-densities, the relaxation time follows temperature-squared behavior. **c)** The additional source of temperature dependence in the resistivities and relaxation times (T^2 v.s. T^1) comes from their Fermi-surface dimensionality, as the number of accessible final scattering states for electrons (states within the radius of a phonon Bose sphere) increases with increasing temperature. The additional temperature dependency from increasing final states, along with increasing phonon occupation, leads to temperature-squared resistivity.

dependence to higher temperatures in perovskite oxides.[101] For less curved Fermi surfaces, at extremely low temperatures, the phonon Bose sphere is so small that it would "see" the Fermi surface as a plane, so the number of accessible final states increases as temperature-squared (a q^2 area of final states). Combining this with a forward-scattering T^2 term results in the T^5 temperature dependence of resistivity predicted by Block.[102] However, the resistivities of most metals[103,104] and perovskite oxides in particular do not show T^5 temperature dependence, because of other scattering mechanisms at these temperatures.[94] The full range of temperature dependencies for typical and two-dimensional Fermi surfaces are illustrated in Figure D.1.

A scattering model (D.36) that includes both acoustic phonon and optical phonon deformation potential scattering confirms this intuitive phase space explanation for temperature-squared relaxation times (Fig. 1.6b). This model considers two phonon branches (populated following the Bose-Einstein distribution function) scattering an electron on a cylindrical Fermi surface. The first phonon branch models the acoustic modes, while the second models the dispersive soft optical modes, which have minimum energy at Gamma but are offset higher in energy from the acoustic modes.[101] The relaxation time below 300 K is dominated by the acoustic scattering modes, while the non-polar optical modes become the dominant scattering source above room temperature. The deformation potential scattering implemented in this physical model is consistent with the experimentally observed relaxation time from 100 K to 1000 K, and the model might be improved at higher temperatures by including scattering from higher-energy optical modes. In fact, recent first-principles evidence suggests that there are at least three optical branches that contribute to the electron-phonon scattering.[85] Furthermore, this model predicts that the relaxation time should become T^1 at very high temperatures (Fig. S1), when all optical modes are appreciably excited. The temperature at which this occurs corresponds to an apparent Debye temperature as measured from the specific heat capacity,[105] which accounts for the excitation of the optical modes. By contrast, a Debye temperature estimated from the speed of sound would underestimate this transition temperature, because this method only considers the acoustic modes.

CHAPTER 2

Electronic Structures as Linear Combinations of Atomic Orbitals

When discussing electronic structure in crystalline materials, there are dual aspects to consider. On one hand is the reciprocal-space representation—that of electronic band diagrams—where electronic states are indexed by their wave-vector k and band-index n. We found that this representation explains the differences in thermoelectric performance between different materials. The complementary perspective of the electronic structure is represented in real-space, where the electronic states correspond to combinations of atomic orbitals.[106,107] Linear combination of atomic orbitals (LCAO) and tight binding theory describe the connection between these two aspects of electronic structure, which facilitates connections between electronic properties and crystal chemistry.[108–111] Small variations in the fractional contribution from each orbital type (s/p/d/f) on each crystal site can have an enormous impact on the electronic band structure. For example, in the diamond-like semiconductors, small variations in orbital character explain whether their band gaps are direct or indirect.[112] While information on electronic properties are more directly encoded within the reciprocal-space representation,[40,113] the atomic orbital representation is effective when explaining the variance among multiple electronic structures. In particular, atomic orbitals are powerful when analyzing electronic structures within a structure family, because the crystallographic sites are fixed and only the fractional orbital contributions are changing.

2.1. Motivation for Mapping Electronic Structures within the half-Heusler Family

The half-Heusler structure family (Figure 2.1) is an excellent test-case for exploring the variance in electronic structure with an atomic orbital basis-set. These materials are strong candidates for thermoelectric applications because of their large peak power factors, which are a result of weak electron-phonon coupling and high valley degeneracy imposed by the symmetry of the Brillouin zone.[114–118] However, these materials suffer from high lattice thermal conductivities. To reduce the thermal conductivity, half-Heuslers are synthesized as complex

solid-solutions, which scatter lattice vibrations through alloy scattering.[29,116,119–124] Isovalent substitutions primarily lower the lattice thermal conductivity, and aliovalent substitutions tune the carrier-density in addition to suppressing thermal conductivity. The highest-performing systems can involve five or more atomic-components, but to simplify their description, these systems can be expressed as pseudo-binaries, pseudo-ternaries, and *ect.* of end-member half-Heusler phases. For example, the quarternary system $Nb_{(1-x)}Ta_xFeSb$ is the pseudo-binary NbFeSb—TaFeSb.

While lattice thermal conductivities in solid-solutions are quantitatively described by empirical models,[125–127] changes in electronic properties are understood more qualitatively. One main effect to consider is band structure engineering—how changes in stoichiometry affect aspects of the electronic structure. To first order, the apparent band structure in a solid-solution (inferred from electronic transport measurements) is a linear interpolation between the end-member electronic structures.[128–134] For example in the Zintl structure family, the band gap and effective mass in n-type Mg_3Sb_2-Mg_3Bi_2 change linearly with composition between Mg_3Sb_2 and Mg_3Bi_2. To begin to understand how changes in atomic-composition (and atomic orbitals) affect electronic structure in the half-Heusler family, we calculated the electronic structures of the stable, semi-conducting (18 valence electrons)

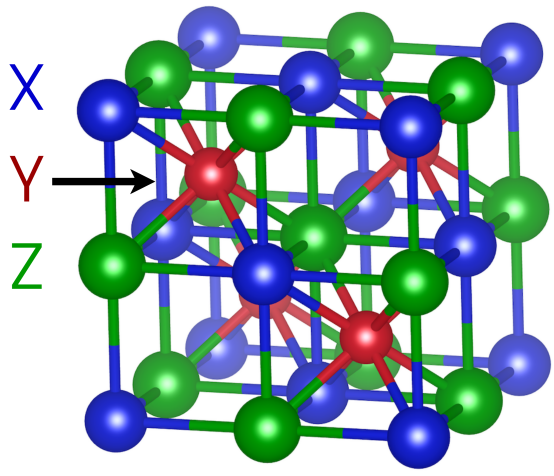

Figure 2.1. There are three crystallographic sites in the half-Heusler structure: X (blue), Y (red), and Z (green). The Y-site is in a body-centered-cubic coordination environment formed by the X- and Z-sites. The X- and Z-sites are in tetrahedral coordination environments formed by the Y-sites (in the first nearest-neighbor shell) and octahedral coordination environments formed by X- and Z-sites (in the second nearest-neighbor shell).

phases reported in the ICSD.[135] To quantitatively compare the calculated phases, we decomposed their near band-edge electronic structures into their natural components—atomic orbitals. Information on atomic orbitals in solids are encoded in the projected density of states,[136,137] which we use to construct a map of the valence band electronic structures. Based on this map, we find that there are three distinct classes of electronic structure. The valence band maximum is at a different k-point in the Brillouin zone for each electronic structure class. Phases that are intermediates of the extreme cases have increased valley degeneracy from the energy convergence of multiple k-points at the band edge. Similar to the valence rules developed to predict the stability of half-Heusler phases,[135] we develop several valence rules that predict the relative energies of k-points in the Brillouin zone. Instead of considering the total valence electron count (rules for stability), these rules consider the relative valence electron configurations of the elements on each site of the crystal structure.

2.2. Orbital Phase Diagram of the half-Heusler Valence Band Electronic Structures

In p-type semiconductors, charge-transporting holes occupy states in the valence bands according to the distribution function for holes ($h = 1 - f$, where f is the Fermi-Dirac distribution function).[138] These valence states are ascribed to particular atomic orbitals in the projected density of states (g_i). The number of occupied holes from a particular atomic orbital (p_i) is accumulated from the valence band states.

$$p_i = \int_{VB} g_i(E) \cdot h(E) \cdot dE \tag{2.1}$$

The fractions of atomic-like holes ($x_i = p_i / \Sigma_i p_i$) describe the composition of the system of holes in a particular phase. This composition depends on the electron chemical potential (Fermi-level) and temperature, but for consistency across multiple p-type phases, standard conditions can be chosen. In this work, the Fermi-level is placed at the valence band edge and the temperature is 700 K, which is near the temperature at the peak power-factor for these materials. Between the three crystallographic sites ($X/Y/Z$) and three orbital characters (s/p/d) there are nine components to consider. However, only several of the components contribute meaningfully to the valence states, and 97% of the variation in orbital character is accounted for by the X-d, Y-d, and Z-p components alone. Therefore, the phases can be represented in a Gibbs phase triangle (Figure 2.2a). In contrast to a

conventional phase diagram, which represents the stable phases within a composition region, the “orbital phase diagram” represents the diverse electronic structures expressed by phases within a structure family.

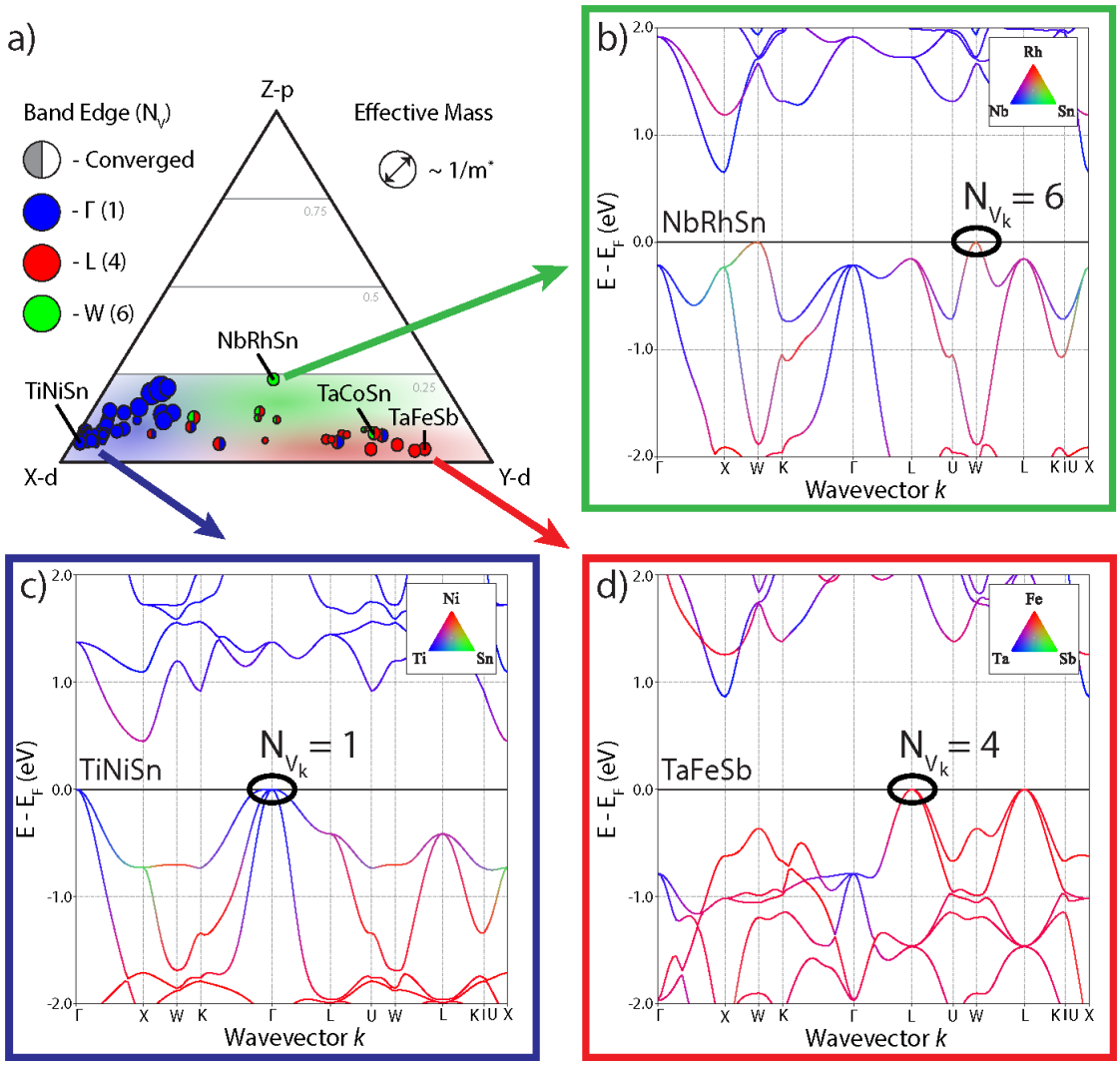

Figure 2.2. **a)** The valence band edges of half-Heusler electronic structures are primarily composed of d-orbitals from the X- and Y-sites, and secondarily, p-orbitals from the Z-site. The relative contributions of these basis orbitals describe the type of carrier pockets observed in this structure family. **b)** Electronic structures with higher concentrations of Z-p orbitals at the band edge have carrier pockets at the W-point with high degeneracy. **c)** Phases with valence band edges dominated by X-d states have carrier pockets at the Γ-point, and **d)** band edges dominated by Y-d states have carrier pockets at the L-point.

There are three limiting cases of valence band electronic structures (indicated by blue, red, and green). The first class of electronic structure (blue) has the valence band maximum at Γ, which has a degeneracy of one in the first Brillouin zone (N_{v_k}). To clarify, we are considering the degeneracy imposed by the symmetry of the Brillouin zone, which does not include the number of degenerate bands (N_{v_o}, orbital degeneracy) at that k-point ($N_v = N_{v_k} \cdot N_{v_o}$). TiNiSn is an example compound from this class, where the valence band edge is dominated by Ti-d states (Figure 2.2c). The second electronic structure class (red) has its valence band maximum at the L-point—a degeneracy of four. TaFeSb exemplifies this class, where the band edge states are dominated by Fe-d (Figure 2.2d). In the last class of electronic structure (green), the valence band maximum is at the W-point (degeneracy of six). These electronic structures ($e.g.$ NbRhSn in Figure 2.2b) have relatively higher band-edge contributions from Z-p orbitals, which originates from the states along the X-W path (green-orange hue). Each of the other electronic structures are intermediates of the three limiting cases. For example, NbCoSn is an intermediate between the W-point (green) and L-point (red) extremes, with both carrier pockets within 100 meV of the band edge. Irrespective of the electronic structure class, the type of atomic orbitals contributing to each k-point (within the first valence band) are similar among all of the half-Heusler materials—the Γ-point is dominated by X-d states, the L-point is dominated by Y-d states, and Z-p states are mixed into the X-W path. Therefore, the chemical bonding is similar among all the materials. The primary source of variance among their electronic structures is the relative energies of the Γ-, L-, and W-points, which are linked to the relative energies of their constituent atomic orbitals.

2.2.1. Valence Rules for Engineering Γ-L Carrier Pockets

Engineering the Γ-L energy offset tunes the valley degeneracy and the thermoelectric performance of half-Heusler materials.[116] The relative energies of the Γ- and L-points are described by simple, chemical differences between the X- and Y-species. The dominant, first-order effect is the difference in valence between the X- and Y-species, which is encoded in their group (column) number on the periodic table. In a linear model, differences in valence account for over 85% of the variation in the Γ-L energy offset (Figure 2.3). Compounds with larger differences in valence have valence band maxima at Γ (*e.g.* TiNiSn, where Ni has six more valence electrons than Ti), while compounds with smaller differences in valence have valence band maxima at L (*e.g.* NbFeSb, where Fe

has only three more valence electrons than Nb). A second-order descriptor is the difference in electronegativity between the X- and Y-species, which can account for differences in the Γ-L energy offset between compounds with isovalent species (*e.g.* NbCoSn and NbRhSn). Furthermore, elemental characteristics of the Z-species do not improve the prediction of the Γ-L energy offset, likely because the energies are properties of the X- and Y-species orbitals. Recall that the Γ- and L-point states are formed from the X-d and Y-d orbitals.

The valence difference rule extends beyond the semiconducting phases to metastable phases with 17 and 19 valence electrons, which are p- and n-type metals (Figure E.1). For example, while the energy difference between the Γ- and L-points is nearly zero for TiCoSb, the Γ-pocket dominates the valence band maximum in the Ni-substituted analog; TiNiSb has a larger valence difference and 19 valence electrons. Conversely, in the Fe-substituted analog, the L-pocket dominates; TiFeSb has 17 valence electrons and a smaller difference in

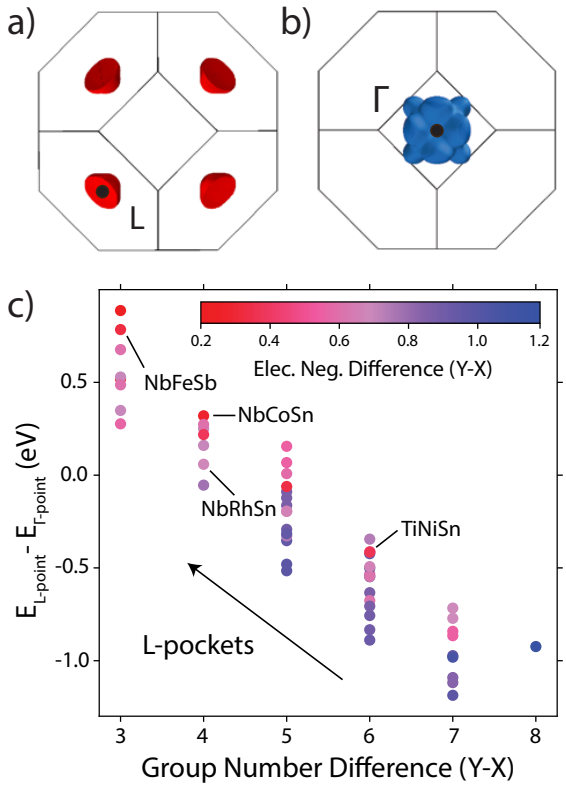

Figure 2.3. The difference in valence electron configuration (encoded in group number) and electronegativity of the X- and Y-species determines the energy offset between the Γ- and L-points. Engineering the relative energies of these k-points controls the degeneracy (four in the case of L-pockets and one for Γ-pockets).

valence. While TiNiSb and TiFeSb are not stable themselves, there are implications for forming solid-solutions between TiCoSb and and either of the metallic end-members (electronic doping)—the relative energies of the Γ- and L-points may change.

2.2.2. Engineering Highly-Degenerate W-pocket Alloys

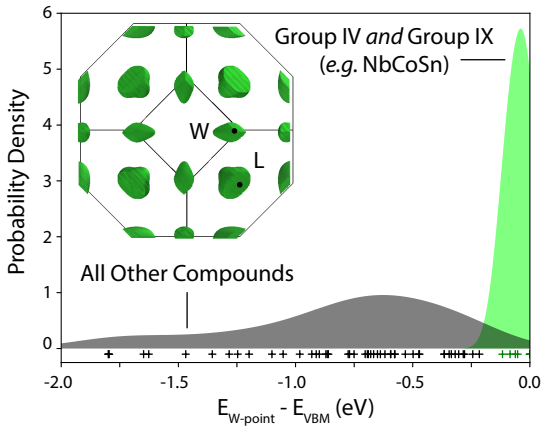

Figure 2.4. The W-point is at or near the valence band maximum for compounds with *both* a Group IV element on the Z-site (Sn, Ge) and a Group IX on the Y-site (Co, Rh, or Ir). Furthermore, in six of the seven W-pocket materials, the L-point is converged within 100 meV of the band edge (total degeneracy of ten).

Materials that contain *both* group-IV (*e.g.* Sn) and group-IX (*e.g.* Co) elements adopt a distinct class of electronic structure, where the W-point is at or near the valence band edge (Figure 2.4). In six of these seven phases, the W-point and L-point are both within 100 meV of the valence band edge, effectively converged at 1200 K. While only Sn- and Ge-containing end-member phases are reported stable in the literature, the calculation of metastable NbCoPb confirms that this valence rule extends beyond Sn- and Ge-containing compounds (Figure E.2). Entropy-stabilized solid-solutions between NbCoSn and NbCoPb could benefit from reduced lattice thermal conductivity from alloy scattering and retain valley-high degeneracy throughout the solid-solution. However, the carrier-density must be tuned to optimize the thermoelectric transport properties. There are three sites where aleovalent substitution can introduce additional holes in the system and tune the carrier-density. We have computed several site-substituted end-members to investigate the potential changes in band structure induced by candidate dopant elements (Figure E.2). Substituting on the X- and Y-sites has the expected behavior

of tuning the Γ-L energy offset, based on the valence difference rules developed in the previous section. Substituting Ti on the Nb-site raises the relative energy of the Γ point, since the valence difference between Ti and Co is larger than between Nb and Co. Introducing Fe on the Co-site has the opposite effect, and pushes the L-point above the W-point, un-converging the bands. However, substituting In on the Sn-site has an entirely new effect. In NbCoIn, the X-point is at the valence band edge. This compound has entirely different class of electronic structure, distinct from the three archetypal band structures identified in Figure 2.2. The band structure has flat and dispersive character between the X- and W-points, which is similar to the band character found in $SrTiO_3$ and some full-Heusler phases.[88,139] There may be differences in transport properties between materials doped on each of the three sites.

2.3. Alternatives to an Atomic-Limit Representation: Hybrid Orbital Basis Sets

In the preceding section, we found that atomic orbital representations clearly separate different classes of electronic structure within a family of compounds. Plotting each phase within an orbital phase diagram helps elucidate the primary sources of variance among the reciprocal-space electronic structures. However, the atomic orbital representation fails to capture the role of bonding within the electronic structure. For example, in half-Heusler phases that are dominated by a combination of X-d and Y-d character, do the d-orbitals from each site form a bond? or are they non-bonding? Upon inspection of the band structure, it is clear that they are non-bonding, because there is relatively little mixing of the orbital character at individual k-points, but this is not explicitly clear from the orbital scores. The atomic orbital representation does not describe how the individual orbitals interact with one another. Hybrid orbital basis-sets can overcome this shortcoming. In the solid-state, Wannier orbitals are a powerful option for investigating orbital hybridization. The specific hybridization of the atomic orbitals can help explain the dispersion of the electronic bands in the reciprocal-space representation of the electronic structure.

The valence and conduction band structures of many perovskite oxides (including $SrTiO_3$) are composed of d-orbitals from the B-site (Ti-site) and p-orbitals from the oxygen sites.[86] The specific mixing of the d/p-orbitals is complicated, but can be simplified by constructing maximally localized Wannier functions. Wannier functions are the crystal equivalent of localized molecular orbitals and visually embodies hybridization of the constituent

atomic orbitals.[140] Furthermore, the dispersion of electronic bands in momentum (k) space is readily rationalized by the mixing of Wannier functions from all crystal sites, which creates a crystal orbital—the extension of molecular units to periodic systems. We find that the conduction bands are composed of two-dimensional crystal orbitals, which is reflected in two-dimensional dispersion at the conduction band edge.

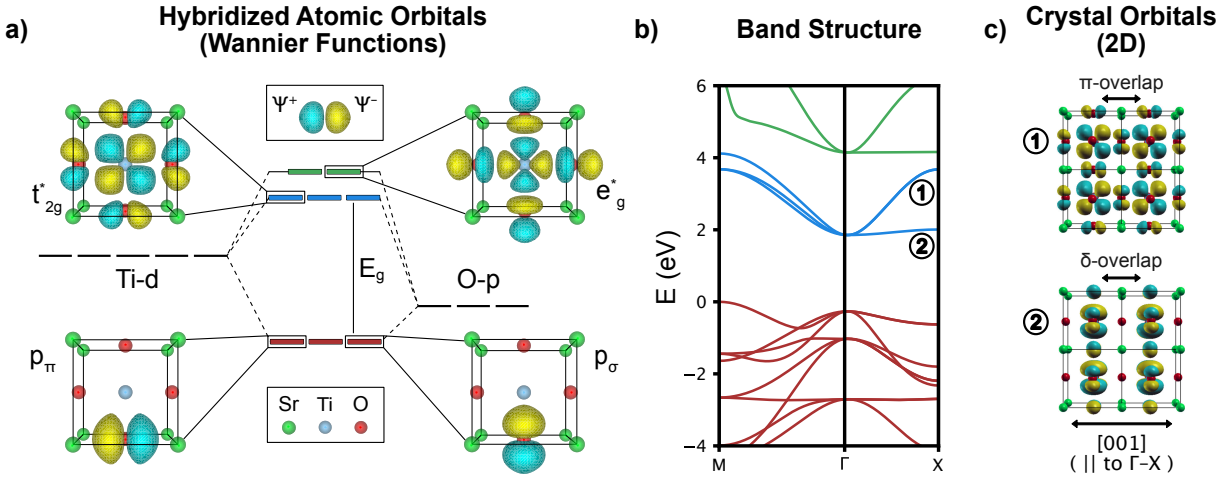

Figure 2.5. The electronic structure of $SrTiO_3$ is described by two-dimensional crystal orbitals, even though the crystal structure is three-dimensional and cubic. **a)** In the unitcell, local Ti-d and O-p orbitals hybridize via covalent bonds; an octahedral crystal field splits the anti-bonding Ti-d states into two subsets. Each hybrid state is visualized by maximally localized Wannier functions and exhibits strong anti-bonding character in the conduction states and subtle bonding character in the valence states. **b)** Each hybrid orbital state broadens into bands in momentum (k) space when they mix with adjacent unitcells. Crystal orbitals are formed from the mixing of Wannier functions from all crystal sites, and the introduction of a Bloch phase factor between neighboring orbital hybrids specifies a particular k-state. For the lowest-lying conduction bands (labeled by 1 and 2), mixing only exists between t^*_{2g} orbitals of the same x/y/z symmetry. **c)** There are two interactions between adjacent t^*_{2g} orbitals that dictate the strength of dispersion in k-space. **(1)** The strong π-interactions in the plane of each basis orbital give dispersive character to the bands. **(2)** The weak, out-of-plane δ-interactions give non-dispersive character, which is a signature of its low-dimensional electronic structure along the Γ-X directions (parallel to the $\langle 100 \rangle$ family of crystallographic directions).

At the unit cell level, Wannier functions for $SrTiO_3$ show strong hybridization of titanium d-states (Ti-d) and oxygen p-states (O-p), which create bonding or anti-bonding covalent interactions (Fig. 2.5a). The bonding character of the valence states is expressed by distortions of the O-p orbitals toward the titanium atoms. By contrast, the Ti-d and O-p orbitals in the conduction states have opposite phase, which represents anti-bonding character. The anti-bonding t_{2g} hybrids (t^*_{2g}) are lower in energy than the anti-bonding e_g hybrids (e^*_g), because

π-anti-bonding interactions are relatively weaker than σ-anti-bonding interactions. The degeneracy of the anti-bonding states is determined by the octahedral symmetry of the crystal field. Furthermore, the anti-bonding states retain the symmetry representations of pure d-states, even though they are hybridized with O-p—their symmetry properties, including mutual orthonormality, are not affected.

Wannier functions on neighboring crystal sites overlap and mix, which creates dispersive bands of energy states. The electron states in these bands are well known as the Bloch wavefunctions. Individual Bloch states (k-states) are constructed from a sum of Wannier functions from all the crystal sites, with appropriate phase factors (set by k) between neighboring orbitals. The set of Wannier functions required to represent a Bloch state (not accounting for the phase factors) defines what can be understood as a crystal orbital. The Bloch states of the lowest-lying conduction bands (blue in Fig. 2.5b, which determine n-type transport) can be grouped into three bands based on their crystal orbital symmetry (an alternative ordering to energy). Each band of states is described by a single crystal orbital, which is composed of a single t_{2g}^* Wannier function (tiled over all lattice sites). While the typical band ordering by energy (Fig. 1.4a) is convenient from a computational standpoint, the alternative grouping by crystal orbital (Fig. 1.4b) facilitates a chemical interpretation of the electronic structure, because the dispersion of bands in k-space is explained by the changes in the crystal orbital bonding interactions as a Bloch phase is introduced. The k-space dispersion can be explained by the crystal orbitals themselves.

Consider the band of states described by the x-y t_{2g}^* crystal orbital (d_{xy}^*, states dominated by the Ti-d_{xy} atomic orbitals). In the x-y plane, the neighboring Wannier functions overlap via strong π-interactions, while in the z-direction, they overlap via weak δ-interactions (Fig. 2.5c). Again in the x-y plane, notice that the O-p orbitals within one Wannier function are in a bonding configuration to the Ti-d orbitals in a neighboring Wannier function. Thus the π-interaction is bonding at Γ ($k = 0$), whereas if there was no d/p-hybridization and only Ti-d_{xy} character, the interaction would be anti-bonding at Γ. The energies of the electronic states increase as k moves from Γ to X; orbitals become more anti-bonding with their neighbors as a Bloch phase is introduced. Therefore, the conduction band minimum is at Γ. The bridging oxygen character is essential for the strong π-interactions in the x-y plane, but there is a lack of bridging oxygen character in the z-direction. Hybridization between Ti-d_{xy} and O-p orbitals in the z-direction is symmetry forbidden, since those orbitals are orthogonal. The weak interactions in the z-direction makes this crystal orbital two-dimensional, since only two directions

have substantive interactions. The weaker orbital overlap along the z-direction leads to anisotropic dispersion, which is so weak that Fermi surfaces of this carrier pocket resemble a cylindrical shape.

Each of the three conduction bands are composed of symmetry equivalent t_{2g}^* crystal orbitals. For each crystal orbital, there is a direction where p/d-hybridization is forbidden, which weakens the dispersion in that crystallographic direction, and creates cylindrical Fermi surfaces in the Brillouin zone. All three of the t_{2g}^* Fermi surfaces intersect to create the complex Fermi surfaces predicted by first-principles electronic structure calculations[141,142] and observed in ARPES measurements.[71–73] These Fermi surfaces are often described as "warped" or having a "jack shape" (Fig. 1.4a). The Fermi surfaces of two-dimensional electron gases observed by ARPES are projections of bulk Fermi surfaces onto planes in the Brillouin zone (planes parallel to the surface plane), which indicates that the surface electronic structure is controlled by the same orbital basis.[73] Other perovskite oxides with the same orbital interactions as $SrTiO_3$ have electronic structures with similar character and dispersion. By contrast, other perovskite oxides, such as $BaSnO_3$, will not have these features, because they lack d-p hybridization (it is weak s-p hybridization) in the valence and conduction bands.[143]

The crystal orbital analysis is relatively straightforward for $SrTiO_3$, because the Bloch states can be divided into three bands based on their crystal orbital symmetry. The crystal orbitals for each band of k-states do not depend on k. In systems where the Bloch states can not be divided into crystal orbital invariant bands, this analysis may be significantly more complicated. Nevertheless, the maximum localization criteria for Wannier functions naturally leads to crystal orbital representations that do not vary strongly with k,[140] so this method of analysis may be generalized to other crystals.

CHAPTER 3

Thermoelectric Material Performance in Polycrystalline Systems

In practice, defects are introduced into either the lattice or micro-structure of promising thermoelectric materials to suppress their thermal conductivities. The creation of grain boundary interfaces through nanostructuring is one of the most promising strategies.[144–146] However, grain boundaries can limit the electronic performance of some thermoelectric materials such as Mg_3Sb_2 and $SrTiO_3$ (Figure 1.1).[5,6] Treating the grain boundary as a secondary phase (sometimes termed a grain boundary complexion) explains the rich transport behavior observed in polycrystalline samples and is conceptually appealing for considering thermodynamic design principles for tuning these properties, since the grain boundary phase itself can be changed (phase transitions) or engineered.[147,148] Furthermore, this conceptual framework is compatible with recently developed ab-initio defect calculations,[149] which could be used to study and explain grain boundary resistance on a microscopic level. Optimizing the interfacial properties of $SrTiO_3$ using grain boundary engineering could lead to higher thermoelectric performance than previously realized, especially near room temperature (Appendix F).

3.1. The Effect of Grain Boundaries on Electronic Transport

Comparing the response of polycrystalline ceramics and single crystals of $SrTiO_3$ highlights the effect of grain boundaries on the conductivity and Seebeck coefficient. While the temperature dependence of polycrystalline samples show activated conductivity to varying degrees (Figure 3.1a), which is qualitatively different from the behavior of heavily-doped single crystal samples; the Seebeck coefficients only gradually increase with temperature (Figure 3.1b), which is the same Seebeck behavior as the single crystals.[7] Therefore, grain boundary effects have a particular signature in transport data: conductivity is heavily affected, while the Seebeck coefficient is not. The same phenomenon is observed in the Mg_3Sb_2 material system and is explained by a series circuit model, where the grain and grain boundary are treated as separate phases that contribute to the overall properties,[5] without invoking energy filtering at the interface.[150,151]

In the series circuit model, the resistances from the grain and grain boundary regions are additive. Therefore, the apparent resistivity is the sum of the individual resistivities, weighted by the relative thickness of the grain and grain boundary regions ($\rho = (1 - t_{GB})\rho_G + t_{GB}\rho_{GB}$). While the thickness of the grain boundary is typically much smaller than the grain size ($t_{GB} \ll 1$, because the grain size is on the order of microns and the

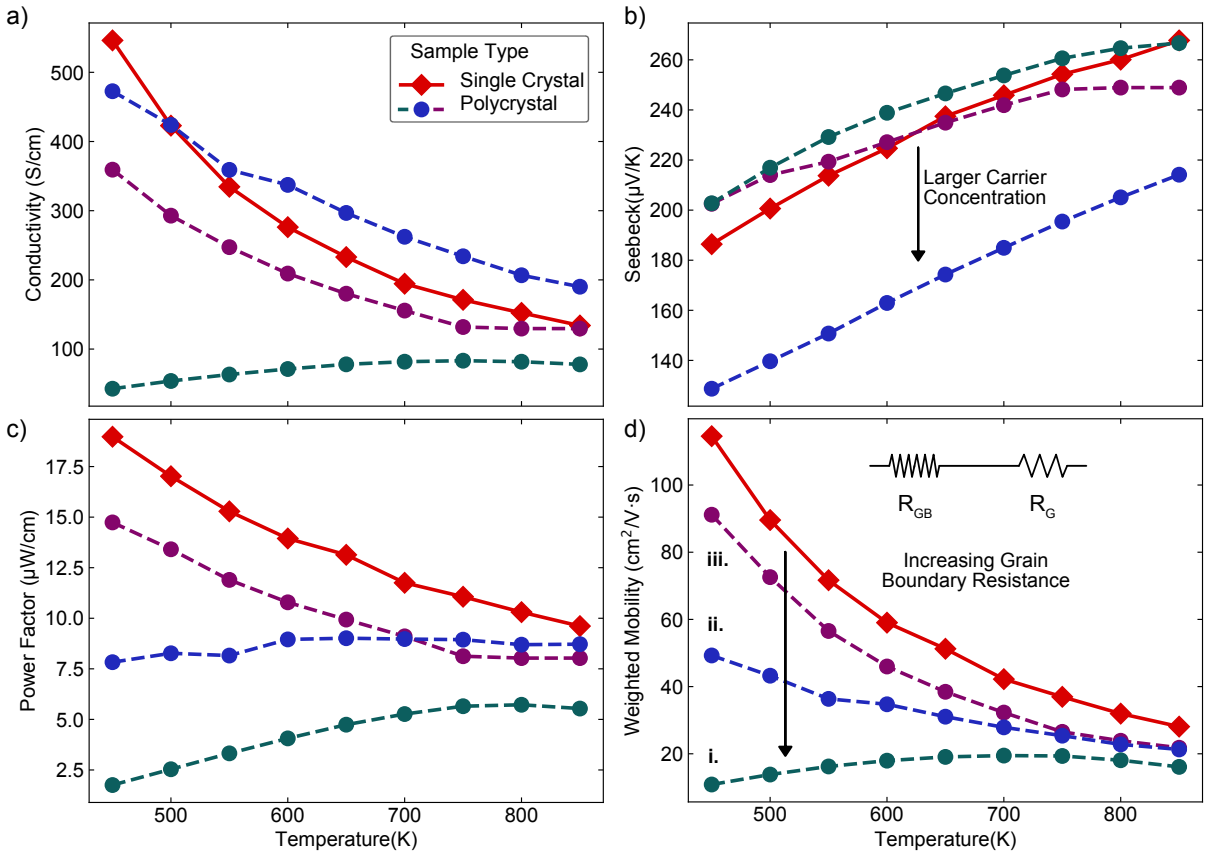

Figure 3.1. Grain boundary resistance has a particular signature in transport data. **a)** The experimental conductivities of polycrystalline $SrTiO_3$ are heavily affected and become activated with temperature in extreme cases of grain boundary resistance (green). **b)** The Seebeck coefficients of polycrystalline samples are not affected by the grain boundary (there is only one sample with a higher carrier concentration, which decreases the magnitude of the Seebeck), and their temperature dependence is the same as single crystal samples. **c)** The degraded conductivities result in lower power factors in polycrystalline samples. **d)** Any doping dependence in the transport properties can be removed by analyzing the weighted mobility, where all polycrystalline samples (dashed) fall below the single crystal properties (solid). Experimental data from red to green:[6,7,11,12]. The polycrystalline samples shown are the median samples from the different grain boundary phases in Figure 3.3a. This set of samples demonstrates the range of expected grain boundary behaviors.

grain boundary is on the order of nanometers), the resistivity of the grain boundary can be much greater than the resistivity of the grains ($\rho_{GB} \gg \rho_G$). In this case, the grain boundary contribution to the transport is still non-negligible ($\rho \neq \rho_G$). In fact, the grain boundary can dominate the transport response at low temperature (green in Figure 3.1a). By contrast, the Seebeck coefficient is typically not dominated by the grain boundary phase. When the thermal conductivities of the grain and grain boundary are similar in magnitude (because a significant amount of heat is transported through the interface by phonons), the total Seebeck coefficient is a weighted sum of the individual Seebeck coefficients of the grain and grain boundary regions ($\alpha = (1 - t_{GB})\alpha_G + t_{GB}\alpha_{GB}$). For a grain size of 1 μm and a grain boundary thickness of 10 nm, the Seebeck coefficient of the grain boundary would need to be greater than ~10,000 $\mu V/K$ to have the same magnitude of effect as observed in the resistivity. Therefore, the total Seebeck coefficient is dominated by the grain properties ($\alpha \sim \alpha_G$), which is typically on the order of ~100 $\mu V/K$. For a polycrystalline sample with conductivity dominated by grain boundary resistance, the Seebeck behavior is remarkably similar to the single crystal properties (green in Figure 3.1b).

Due to the carrier concentration dependence of transport properties, the sample-to-sample variation in grain boundary effects is difficult to quantify in polycrystalline ceramics. One solution is to analyze Seebeck-conductivity data with an effective mass model.[1] In the effective mass model, the weighted mobility ($\mu_0(m^*/m_e)^{3/2}$) quantifies both the number (characterized by the effective Seebeck mass, m^*) and mobility (characterized by the mobility parameter, μ_0) of conduction channels for thermoelectric transport—it is a carrier concentration independent quantity, similar to mobility in the Drude model ($\sigma = n\mu$). The weighted mobility is correlated to the potential for high power factor, can be used to directly compare the electronic properties of samples with different carrier concentrations, and shows that the electronic properties of all the polycrystalline samples are worse than single crystals in terms of thermoelectric performance (Figure 3.1d, although they could be equal in the case of no grain boundary resistance). This analysis reveals that transport properties at lower temperatures are affected by grain boundaries the most, since the weighted mobility is degraded by a lesser fraction at high temperatures. Optimizing the carrier concentration in samples not affected by grain boundary resistance will result in high power factors, even near room-temperature, which are comparable to other high-performing thermoelectric materials (Figure 1.1). In samples dominated by grain boundary resistance, high power factors are only achieved at high temperatures (green in Figure 3.1c).

3.2. Microscopic Origins of High Grain Boundary Resistance

The accumulation of excess charge near grain boundaries is the origin of high grain boundary resistance in $SrTiO_3$.[152] The electric potential induced by these charges is directly observed in electron holography experiments of bi-crystals and polycrystalline ceramics,[153–156] and is indirectly measured by electrical impedance measurements.[153,157–160] These experiments indicate that the grain boundary potential is negative. A negative grain boundary potential suggests that there is either a depletion of positively charged defects or an excess of negatively charged defects near the boundary. In n-type materials, a dominant point defect to consider is the positively-charged oxygen vacancy ($V_O^{\cdot\cdot}$), which is an electron-donating defect. Molecular dynamics simulations indicate that the concentration of $V_O^{\cdot\cdot}$ is depleted in regions near dislocation cores, which form the substructure of grain boundaries.[13] Furthermore, oxygen vacancy depletion has been observed in tracer diffusion experiments near free-surfaces.[161] Depleted $V_O^{\cdot\cdot}$ concentrations near interfaces (Figure 3.2a) are consistent with the negative potentials (Figure 3.2b). The induced potential bends the conduction bands upwards, which produces a barrier for electron conduction (Figure 3.2c). The electronic resistance is high, due to the lack of free carriers in the grain boundary region (Figure 3.2d). Transport models indicate that a low carrier concentration at the interface explains the high resistivities of polycrystalline samples.[5]

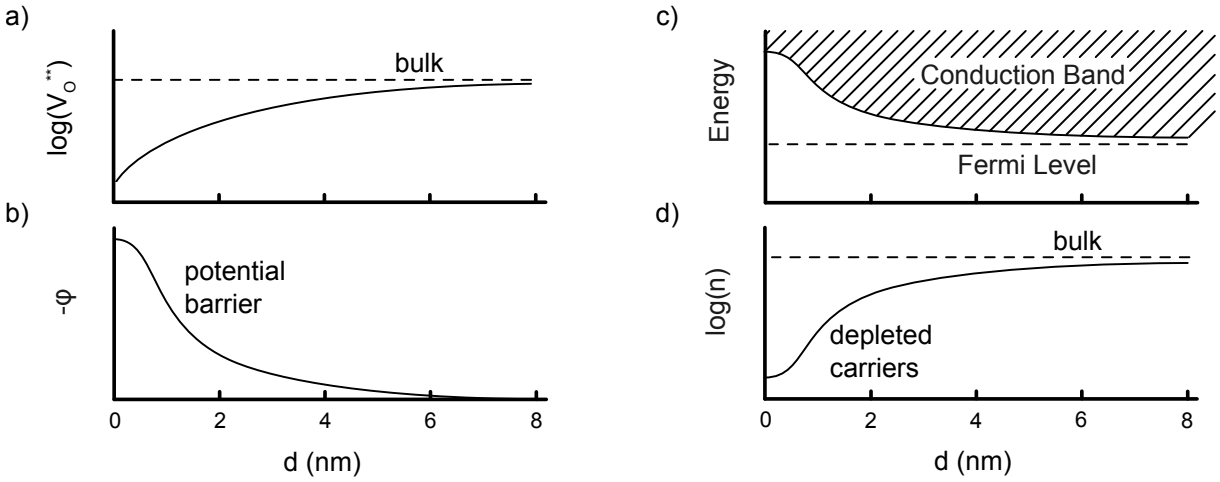

Figure 3.2. **a)** The lower oxygen vacancy concentrations ($V_O^{\cdot\cdot}$) in the vicinity of the grain boundary are responsible for grain boundary resistance in $SrTiO_3$ (the vacancy profile reflects the simulated data in[13]). **b)** The depletion of positively charged oxygen vacancies induces a negative potential (ϕ) that **c)** perturbs the electronic states in the conduction band. **d)** As a result, the grain boundary phase is depleted of free carriers (n) and is resistive.

Depleted $V_O^{\cdot\cdot}$ concentrations in grain boundary phases indicate that their point defect formation energy is higher than in the bulk phase ($\Delta E_{f,gb} > \Delta E_{f,b}$). However, it is well known that these defect energetics and concentrations are controlled by the chemical potential of oxygen, which is set by the partial pressure of oxygen in experiments.[75] The oxygen partial pressure may even control the relative defect concentrations of the interface and bulk phases (not just their individual magnitudes), because polycrystalline samples show less grain boundary resistance at low oxygen partial pressures, compared to high oxygen partial pressures.[93] A second consideration for the relative defect formation energies is the grain boundary phase itself, because the grain boundary interface undergoes phase transitions with temperature.[14] At these phase transition temperatures (near 1490, 1545, and 1605 ℃), the coarsening kinetics of the boundary and the grain boundary width change discontinuously, and each phase may have different defect formation energies. Polycrystalline ceramics from the literature are typically sintered at either 1400, 1500, or 1600 ℃.[6,7,11,12,15–19] Each sintering temperature falls within a different grain boundary phase region, and therefore, each sintering temperature likely produces a different grain boundary phase. Analyzing fifty samples from the literature shows that the (assumed) different grain boundary phases have statistically different amounts of grain boundary resistance (Figure 3.3a). Insight into the microscopic differences between these grain boundary phases might be enhanced by first-principles defect calculations.[149] Several first-principles studies have already treated neutral point defects in interface structures.[162–164]

3.3. Extrinsic Grain Boundary Engineering Strategies

Several extrinsic strategies have been used to control grain boundary phases and grain boundary resistance. One such strategy for controlling grain boundary resistance is adding layers of graphene into the grain boundary structure.[20,21] Samples with the addition of graphene show far less activated conductivity near room temperature (Figure 3.3b). Mechanistically, there is some EELS evidence that indicates that the graphene acts as a reducing agent, where oxygen vacancy formation is promoted in regions adjacent to the interfacial graphene.[21] However, it is not yet clear whether the addition of graphene could also provide a conductive network that shorts areas of the grain boundary with high resistance or whether it screens the localized interface charges. Furthermore, the addition of graphene inhibits coarsening of the grain structure and has been shown to increase interfacial thermal

resistance in other material families, such as skutterudite.[165] Decorating grain boundaries with graphene appears to be a robust strategy for optimizing both the electronic and thermal properties of thermoelectric materials.

A second strategy has sought to control the grain boundary orientation angles of ceramic samples by first synthesizing nanocrystalline precursors stabilized by different weak acids.[166] The choice of acid stabilizes different surface planes in the nanocrystals, which results in different populations of grain boundaries in the sintered samples. Samples with more $\Sigma 3$ boundaries, a twin grain boundary with high atomic registry, showed lower grain boundary resistance. Oxygen diffusion experiments of $\Sigma 3$ bicrystals have indicated that this grain boundary orientation does not accumulate a potential barrier,[167] which has been confirmed by first-principles supercell calculations of that interface.[168]

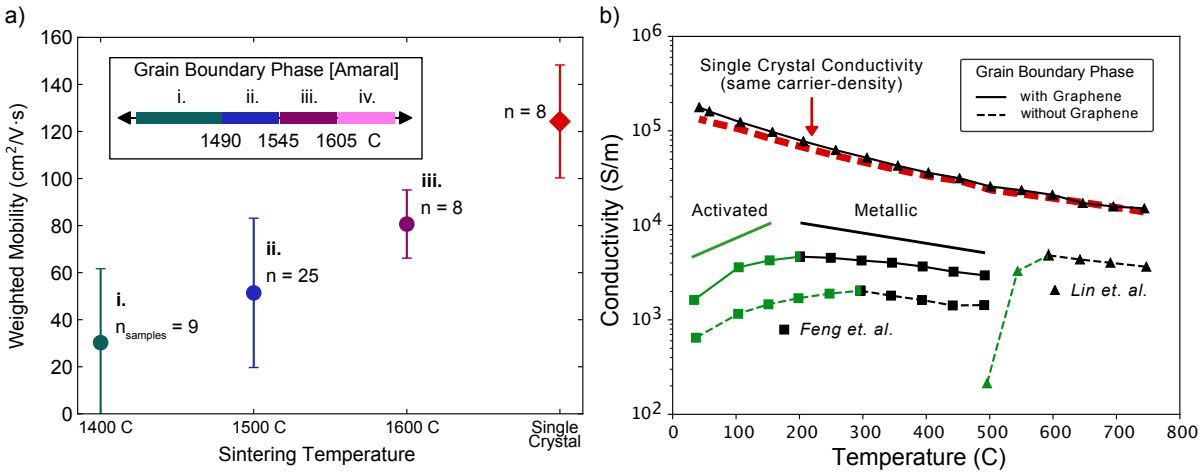

Figure 3.3. **a)** The grain boundary phase undergoes transitions near temperatures that ceramic samples are sintered.[14] Analyzing the transport of fifty samples near room temperature (450 K) reveals that these phase transitions may be changing the defect energetics in the grain boundary phase and therefore the observed grain boundary resistance.[6,7,11,12,15–19] Error bars indicate one standard deviation for the distribution of weighted mobilities. **b)** Grain boundary resistance is responsible for conductivity that is activated with temperature (highlighted in green). Grain boundary engineering with graphene decreases the effect of grain boundary resistance, and samples show metallic-like behavior (conductivity that decreases with temperature, highlighted in black) at lower temperatures.[20,21] Single crystal electronic properties are achieved by Lin et al..

CHAPTER 4

Looking Forward: Mapping Properties in Calculation Databases

Due to the efficiency of density functional theory in high-throughput computing paradigms[137,169], the properties of many crystalline materials are readily available in open-source databases, such as the *Open Quantum Materials Database* and the *Materials Project*.[143,170,171] Applying the orbital phase diagram technique to structures in these databases could be a powerful strategy for exploring their electronic properties. However, this technique is most powerful when applied to material families, where each phase has the same crystal sites. Recent advances in assessing the local coordination environments in crystal structures show promise for organizing materials databases into structure families.[172,173] Since each structure is composed of a set of sites, we can use the distribution of local coordination environments in a structure as quantitative measure of that structure. For example, all of the sites in the rock-salt structure have octahedral local coordination environments, while all the sites in a diamond-like material are in tetrahedral environments. The difference between the distributions of coordination environments in two structures measures their similarity. Structures within a similarity threshold may belong to the same family. A prototype of this database organization is implemented on the *Materials Project*.

When measuring the structural similarity between two phases, we are measuring whether those two phases transform into one another through the introduction of one or more site-substituting defects. This can be taken one step further by considering whether two phases are similar when introducing either vacancy or interstitial defects (Figure 4.1). For example, placing an interstitial atom in the diamond primitive unit-cell transforms it into the half-Heusler structure. Recent work on half-Heusler materials has shown that there are new phases to be discovered between material families in this fashion, where the new phases are described as intermediate defect structures.[135,174] The 19-electron half-Heusler phases are between diamond-like and half-Heusler structures. Since these phases share a set of common sub-lattices with their respective end-members, the orbital phase diagram approach would also be useful for exploring the electronic properties between defect-related material families.

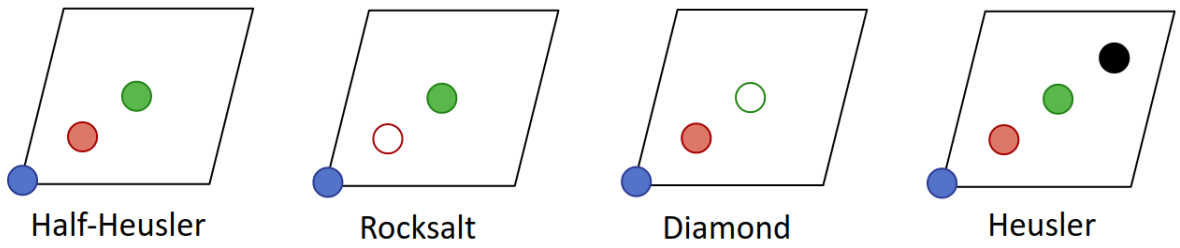

Figure 4.1. Illustration of the FCC primitive unit cells of several crystal structures. The structures are related by defects. For example, the half-Heusler structure transforms into the rock-salt and diamond structures when vacancies (open circles) are introduced. In addition, adding an interstitial atom (black circle) to the half-Hesuler structure produces the Heusler structure.

References

[1] Andrew May and G Snyder. Introduction to Modeling Thermoelectric Transport at High Temperatures. pages 1–18. April 2012.

[2] I Witting, T Chasapis, F Ricci, M Peters, M Heinz, G Hautier, and G J Snyder. Performance of Bi2te3 for thermoelectrics. *Unpublished*.

[3] Yinglu Tang, Zachary M. Gibbs, Luis A. Agapito, Guodong Li, Hyun-Sik Kim, MarcoÂăBuongiorno Nardelli, Stefano Curtarolo, and G. Jeffrey Snyder. Convergence of multi-valley bands as the electronic origin of high thermoelectric performance in CoSb3 skutterudites. *Nature Materials*, 14(12):1223–1228, December 2015.

[4] Aaron D. LaLonde, Yanzhong Pei, and G. Jeffrey Snyder. Reevaluation of pbte1-xix as high performance n-type thermoelectric material. *Energy & Environmental Science*, 4(6):2090, 2011.

[5] Jimmy Jiahong Kuo, Stephen Dongmin Kang, Kazuki Imasato, Hiromasa Tamaki, Saneyuki Ohno, Tsutomu Kanno, and G. Jeffrey Snyder. Grain boundary dominated charge transport in Mg_3Sb_2 -based compounds. *Energy & Environmental Science*, 11(2):429–434, 2018.

[6] Iqbal Mahmud, Man-Soon Yoon, Il-Ho Kim, Moon-Kwan Choi, and Soon-Chul Ur. Thermoelectric properties of the ceramic oxide Sr1-x La x TiO3. *Journal of the Korean Physical Society*, 68(1):35–40, January 2016.

[7] Shingo Ohta, Takashi Nomura, Hiromichi Ohta, and Kunihito Koumoto. High-temperature carrier transport and thermoelectric properties of heavily La- or Nb-doped SrTiO3 single crystals. *Journal of Applied Physics*, 97(3):034106, February 2005.

[8] Jiawei Zhang, Lirong Song, Steffen Hindborg Pedersen, Hao Yin, Le Thanh Hung, and Bo Brummerstedt Iversen. Discovery of high-performance low-cost n-type Mg3sb2-based thermoelectric materials with

multi-valley conduction bands. *Nature Communications*, 8:13901, January 2017.

[9] T. Okuda, K. Nakanishi, S. Miyasaka, and Y. Tokura. Large thermoelectric response of metallic perovskites: Sr 1 - x La x TiO 3 (0 <~ x <~ 0 . 1). *Physical Review B*, 63(11), March 2001.

[10] Akihiro Sakai, Tsutomu Kanno, Satoshi Yotsuhashi, Hideaki Adachi, and Yoshinori Tokura. Thermoelectric Properties of Electron-Doped KTaO $_3$. *Japanese Journal of Applied Physics*, 48(9):097002, September 2009.

[11] Hiroaki Muta, Ken Kurosaki, and Shinsuke Yamanaka. Thermoelectric properties of reduced and La-doped single-crystalline SrTiO3. *Journal of Alloys and Compounds*, 392(1-2):306–309, April 2005.

[12] A. V. Kovalevsky, A. A. Yaremchenko, S. Populoh, P. Thiel, D. P. Fagg, A. Weidenkaff, and J. R. Frade. Towards a high thermoelectric performance in rare-earth substituted SrTiO $_3$: effects provided by strongly-reducing sintering conditions. *Phys. Chem. Chem. Phys.*, 16(48):26946–26954, October 2014.

[13] Dario Marrocchelli, Lixin Sun, and Bilge Yildiz. Dislocations in SrTiO $_3$: Easy To Reduce but Not so Fast for Oxygen Transport. *Journal of the American Chemical Society*, 137(14):4735–4748, April 2015.

[14] Luis Amaral, Manuela Fernandes, Ian M. Reaney, Martin P. Harmer, Ana M. R. Senos, and Paula M. Vilarinho. Grain Growth Anomaly and Dielectric Response in Ti-rich Strontium Titanate Ceramics. *The Journal of Physical Chemistry C*, 117(47):24787–24795, November 2013.

[15] A. V. Kovalevsky, A. A. Yaremchenko, S. Populoh, A. Weidenkaff, and J. R. Frade. Effect of A-Site Cation Deficiency on the Thermoelectric Performance of Donor-Substituted Strontium Titanate. *The Journal of Physical Chemistry C*, 118(9):4596–4606, March 2014.

[16] Hiroaki Muta, Ken Kurosaki, and Shinsuke Yamanaka. Thermoelectric properties of rare earth doped SrTiO3. *Journal of Alloys and Compounds*, 350(1-2):292–295, February 2003.

[17] Peng-Peng Shang, Bo-Ping Zhang, Yong Liu, Jing-Feng Li, and Hong-Min Zhu. Preparation and Thermoelectric Properties of La-Doped SrTiO3 Ceramics. *Journal of Electronic Materials*, 40(5):926–931, May 2011.

[18] H.C. Wang, C.L. Wang, W.B. Su, J. Liu, H. Peng, J.L. Zhang, M.L. Zhao, J.C. Li, N. Yin, and L.M. Mei. Substitution effect on the thermoelectric properties of reduced Nb-doped Sr0.95la0.05tio3 ceramics. *Journal of Alloys and Compounds*, 486(1-2):693–696, November 2009.

[19] H.C. Wang, C.L. Wang, W.B. Su, J. Liu, Y. Zhao, H. Peng, J.L. Zhang, M.L. Zhao, J.C. Li, N. Yin, and L.M. Mei. Enhancement of thermoelectric figure of merit by doping Dy in La0.1sr0.9tio3 ceramic. *Materials Research Bulletin*, 45(7):809–812, July 2010.

[20] Yue Lin, Colin Norman, Deepanshu Srivastava, Feridoon Azough, Li Wang, Mark Robbins, Kevin Simpson, Robert Freer, and Ian A. Kinloch. Thermoelectric Power Generation from Lanthanum Strontium Titanium Oxide at Room Temperature through the Addition of Graphene. *ACS Applied Materials & Interfaces*, 7(29):15898–15908, July 2015.

[21] Xiaopeng Feng, Yuchi Fan, Naoyuki Nomura, Keiko Kikuchi, Lianjun Wang, Wan Jiang, and Akira Kawasaki. Graphene promoted oxygen vacancies in perovskite for enhanced thermoelectric properties. *Carbon*, 112:169–176, February 2017.

[22] Maria Teresa Buscaglia, Filippo Maglia, Umberto Anselmi-Tamburini, Daniele Marre, Ilaria Pallecchi, Adelina Ianculescu, Giovanna Canu, Massimo Viviani, Monica Fabrizio, and Vincenzo Buscaglia. Effect of nanostructure on the thermal conductivity of La-doped SrTiO3 ceramics. *Journal of the European Ceramic Society*, 34(2):307–316, February 2014.

[23] G. Jeffrey Snyder and Eric S. Toberer. Complex thermoelectric materials. *Nature Materials*, 7:105, February 2008.

[24] Uzma Hira, Li Han, Kion Norrman, Dennis Valbjorn Christensen, Nini Pryds, and Falak Sher. High-temperature thermoelectric properties of Na- and W-Doped Ca $_3$ Co $_4$ O $_9$ system. *RSC Advances*, 8(22):12211–12221, 2018.

[25] Gangjian Tan, Shiqiang Hao, Jing Zhao, Chris Wolverton, and Mercouri G. Kanatzidis. High Thermoelectric Performance in Electron-Doped AgBi $_3$ S $_5$ with Ultralow Thermal Conductivity. *Journal of the American Chemical Society*, 139(18):6467–6473, May 2017.

[26] Brenden R. Ortiz, Prashun Gorai, Lakshmi Krishna, Rachel Mow, Armando Lopez, Robert McKinney, Vladan StevanoviÄĞ, and Eric S. Toberer. Potential for high thermoelectric performance in n-type Zintl compounds: a case study of Ba doped KAlSb $_4$. *Journal of Materials Chemistry A*, 5(8):4036–4046, 2017.

[27] Hyun-Sik Kim, Nicholas A. Heinz, Zachary M. Gibbs, Yinglu Tang, Stephen D. Kang, and G. Jeffrey Snyder. High thermoelectric performance in (Bi 0.25 Sb 0.75) 2 Te 3 due to band convergence and improved by

carrier concentration control. *Materials Today*, 20(8):452–459, October 2017.

[28] Min Ho Lee, Ka-Ryeong Kim, Jong-Soo Rhyee, Su-Dong Park, and G. Jeffrey Snyder. High thermoelectric figure-of-merit in Sb $_2$ Te $_3$ /Ag $_2$ Te bulk composites as Pb-free p-type thermoelectric materials. *Journal of Materials Chemistry C*, 3(40):10494–10499, 2015.

[29] Chenguang Fu, Shengqiang Bai, Yintu Liu, Yunshan Tang, Lidong Chen, Xinbing Zhao, and Tiejun Zhu. Realizing high figure of merit in heavy-band p-type half-Heusler thermoelectric materials. *Nature Communications*, 6(1), December 2015.

[30] Shawna R. Brown, Susan M. Kauzlarich, Franck Gascoin, and G. Jeffrey Snyder. Yb $_{14}$ MnSb $_{11}$: New High Efficiency Thermoelectric Material for Power Generation. *Chemistry of Materials*, 18(7):1873–1877, April 2006.

[31] Dongyang Wang, Wenke He, Cheng Chang, Guangtao Wang, Jinfeng Wang, and Li-Dong Zhao. Thermoelectric transport properties of rock-salt SnSe: first-principles investigation. *Journal of Materials Chemistry C*, 2018.

[32] Georgy Samsonidze and Boris Kozinsky. Accelerated Screening of Thermoelectric Materials by First-Principles Computations of Electron-Phonon Scattering. *Advanced Energy Materials*, 8(20):1800246, July 2018.

[33] Ruiqiang Guo, Xinjiang Wang, Youdi Kuang, and Baoling Huang. First-principles study of anisotropic thermoelectric transport properties of IV-VI semiconductor compounds SnSe and SnS. *Physical Review B*, 92(11), September 2015.

[34] Yongsheng Zhang, Eric Skoug, Jeffrey Cain, Vidvuds Ozolins, Donald Morelli, and C. Wolverton. First-principles description of anomalously low lattice thermal conductivity in thermoelectric Cu-Sb-Se ternary semiconductors. *Physical Review B*, 85(5), February 2012.

[35] L. Xi, Y. B. Zhang, X. Y. Shi, J. Yang, X. Shi, L. D. Chen, W. Zhang, Jihui Yang, and D. J. Singh. Chemical bonding, conductive network, and thermoelectric performance of the ternary semiconductors Cu 2 Sn X 3 (X = Se, S) from first principles. *Physical Review B*, 86(15), October 2012.

[36] Zhiting Tian, Jivtesh Garg, Keivan Esfarjani, Takuma Shiga, Junichiro Shiomi, and Gang Chen. Phonon conduction in PbSe, PbTe, and PbTe 1 - x Se x from first-principles calculations. *Physical Review B*, 85(18),

May 2012.

[37] David Parker and David J. Singh. First principles investigations of the thermoelectric behavior of tin sulfide. *Journal of Applied Physics*, 108(8):083712, October 2010.

[38] S. J. Youn and A. J. Freeman. First-principles electronic structure and its relation to thermoelectric properties of Bi 2 Te 3. *Physical Review B*, 63(8), February 2001.

[39] Seong-Gon Kim, I. I. Mazin, and D. J. Singh. First-principles study of Zn-Sb thermoelectrics. *Physical Review B*, 57(11):6199–6203, March 1998.

[40] Georg K.H. Madsen and David J. Singh. BoltzTraP. A code for calculating band-structure dependent quantities. *Computer Physics Communications*, 175(1):67–71, July 2006.

[41] Guangzong Xing, Jifeng Sun, Khuong P. Ong, Xiaofeng Fan, Weitao Zheng, and David J. Singh. Perspective: n-type oxide thermoelectrics via visual search strategies. *APL Materials*, 4(5):053201, May 2016.

[42] Zachary M. Gibbs, Francesco Ricci, Guodong Li, Hong Zhu, Kristin Persson, Gerbrand Ceder, Geoffroy Hautier, Anubhav Jain, and G. Jeffrey Snyder. Effective mass and Fermi surface complexity factor from ab initio band structure calculations. *npj Computational Materials*, 3(1), December 2017.

[43] R. Landauer. Spatial variation of currents and fields due to localized scatterers in metallic conduction. *IBM Journal of Research and Development*, 1(3):223–231, 1957.

[44] S. Datta. *Electronic Transport in Mesoscopic Systems*, volume 3. Cambridge University Press, Cambridge; New York, 1995.

[45] S. Datta. *Lessons from Nanoelectronics: A new Perspective on Transport.* World Scientific Publishing Co. Pte. Ltd., Singapore, 2012.

[46] P. A. Lee and T. V. Ramakrishnan. Disordered electronic systems. *Rev. Mod. Phys.*, 57:287–337, Apr 1985.

[47] M. Lundstrom and J. Changwook. *Near-Equilibrium Transport.* World Scientific, 2012.

[48] M. Lundstrom, S. Datta, M. A. Alam, M. Baldo, and G. Chen. *Lessons from Nanoscience: A Lecture Notes Series.* World Scientific, 2012.

[49] B. J. van Wees, H. van Houten, C. W. J. Beenakker, J. G. Williamson, L. P. Kouwenhoven, D. van der Marel, and C. T. Foxon. Quantized conductance of point contacts in a two-dimensional electron gas. *Phys. Rev. Lett.*, 60:848–850, 1988.

[50] A. Nitzan and M. A. Ratner. Electron transport in molecular wire junctions. *Science*, 300(5624):1384–1389, 2003.

[51] N. Agraït, A. L. Yeyati, and J. M. van Ruitenbeek. Quantum properties of atomic-sized conductors. *Physics Reports*, 377(2):81–279, 2003.

[52] H. Ohnishi, Y. Kondo, and K. Takayanagi. Quantized conductance through individual rows of suspended gold atoms. *Nature*, 395(6704):780–783, 1998.

[53] Andrew F. May and G. J. Snyder. *Introduction to Modeling Thermoelectric Transport at High Temperatures*, pages 1–18. CRC Press, 2012.

[54] Stephen Dongmin Kang and G. Jeffrey Snyder. Charge-transport model for conducting polymers. *Nature Materials*, 16(2):252–257, February 2017.

[55] Jonathan Hwang, Reshma R. Rao, Livia Giordano, Yu Katayama, Yang Yu, and Yang Shao-Horn. Perovskites in catalysis and electrocatalysis. *Science*, 358(6364):751–756, November 2017.

[56] Chao Su, Xiaoguang Duan, Jie Miao, Yijun Zhong, Wei Zhou, Shaobin Wang, and Zongping Shao. Mixed Conducting Perovskite Materials as Superior Catalysts for Fast Aqueous-Phase Advanced Oxidation: A Mechanistic Study. *ACS Catalysis*, 7(1):388–397, January 2017.

[57] Ewelina Grabowska. Selected perovskite oxides: Characterization, preparation and photocatalytic properties-A review. *Applied Catalysis B: Environmental*, 186:97–126, June 2016.

[58] Sebastien Royer, Daniel Duprez, Fabien Can, Xavier Courtois, Catherine Batiot-Dupeyrat, Said Laassiri, and Houshang Alamdari. Perovskites as Substitutes of Noble Metals for Heterogeneous Catalysis: Dream or Reality. *Chemical Reviews*, 114(20):10292–10368, October 2014.

[59] Sihyuk Choi, Chris J. Kucharczyk, Yangang Liang, Xiaohang Zhang, Ichiro Takeuchi, Ho-Il Ji, and Sossina M. Haile. Exceptional power density and stability at intermediate temperatures in protonic ceramic fuel cells. *Nature Energy*, 3(3):202–210, March 2018.

[60] You Zhou, Xiaofei Guan, Hua Zhou, Koushik Ramadoss, Suhare Adam, Huajun Liu, Sungsik Lee, Jian Shi, Masaru Tsuchiya, Dillon D. Fong, and Shriram Ramanathan. Strongly correlated perovskite fuel cells. *Nature*, 534(7606):231–234, June 2016.

[61] Areum Jun, Junyoung Kim, Jeeyoung Shin, and Guntae Kim. Perovskite as a Cathode Material: A Review of its Role in Solid-Oxide Fuel Cell Technology. *ChemElectroChem*, 3(4):511–530, April 2016.

[62] Bin Zhu, Yizhong Huang, Liangdong Fan, Ying Ma, Baoyuan Wang, Chen Xia, Muhammad Afzal, Bowei Zhang, Wenjing Dong, Hao Wang, and Peter D. Lund. Novel fuel cell with nanocomposite functional layer designed by perovskite solar cell principle. *Nano Energy*, 19:156–164, January 2016.

[63] H. Somaily, S. Kolesnik, B. Dabrowski, and O. Chmaissem. Thermoelectric and structural correlations in (S r 1 - x - y C a x N d y) Ti O 3 perovskites. *Physical Review B*, 96(6), August 2017.

[64] H. Nakatsugawa, M. Saito, and Y. Okamoto. High-Temperature Thermoelectric Properties of Perovskite-Type Pr0.9Sr0.1Mn1-x Fe x O3 (0 < x < 1). *Journal of Electronic Materials*, 46(5):3262–3272, May 2017.

[65] Hongchao Wang, Wenbin Su, Jian Liu, and Chunlei Wang. Recent development of n-type perovskite thermoelectrics. *Journal of Materiomics*, 2(3):225–236, September 2016.

[66] Zhilun Lu, Huairuo Zhang, Wen Lei, Derek C. Sinclair, and Ian M. Reaney. High-Figure-of-Merit Thermoelectric La-Doped A-Site-Deficient $SrTiO_3$ Ceramics. *Chemistry of Materials*, 28(3):925–935, February 2016.

[67] Wan Shen, Regina Dittmann, and Rainer Waser. Reversible alternation between bipolar and unipolar resistive switching in polycrystalline barium strontium titanate thin films. *Journal of Applied Physics*, 107(9):094506, May 2010.

[68] Ruth Muenstermann, Regina Dittmann, Krzysztof Szot, Shaobo Mi, Chun-Lin Jia, Paul Meuffels, and Rainer Waser. Realization of regular arrays of nanoscale resistive switching blocks in thin films of Nb-doped SrTiO3. *Applied Physics Letters*, 93(2):023110, July 2008.

[69] Rainer Waser and Masakazu Aono. Nanoionics-based resistive switching memories. *Nature Materials*, 6:833–840, November 2007.

[70] Krzysztof Szot, Wolfgang Speier, Gustav Bihlmayer, and Rainer Waser. Switching the electrical resistance of individual dislocations in single-crystalline SrTiO3. *Nature Materials*, 5(4):312–320, April 2006.

[71] S. McKeown Walker, A. de la Torre, F. Bruno, A. Tamai, T. Kim, M. Hoesch, M. Shi, M. Bahramy, P. King, and F. Baumberger. Control of a Two-Dimensional Electron Gas on SrTiO 3 (111) by Atomic Oxygen. *Physical Review Letters*, 113(17), October 2014.

[72] T. Rodel, C. Bareille, F. Fortuna, C. Baumier, F. Bertran, P. Le Fevre, M. Gabay, O. Hijano Cubelos, M. Rozenberg, T. Maroutian, P. Lecoeur, and A. Santander-Syro. Orientational Tuning of the Fermi Sea of Confined Electrons at the SrTiO 3 (110) and (111) Surfaces. *Physical Review Applied*, 1(5), June 2014.

[73] P. D. C. King, S. McKeown Walker, A. Tamai, A. de la Torre, T. Eknapakul, P. Buaphet, S.-K. Mo, W. Meevasana, M. S. Bahramy, and F. Baumberger. Quasiparticle dynamics and spin-orbital texture of the SrTiO3 two-dimensional electron gas. *Nature Communications*, 5, February 2014.

[74] J. Mannhart and D.G. Schlom. Oxide Interfaces–An Opportunity for Electronics. *Science*, 327(5973):1607–1611, March 2010.

[75] N H Chan, R K Sharma, and D M Smyth. Nonstoichiometry in SrTiO. *J. Electrochem. Soc.*, 128(8):1762–1769, 1981.

[76] Victor Fistul. *Heavily Doped Semiconductors*, volume 1 of *Monographs in Semiconductor Physics*. Plenum Press, 1969.

[77] A.H. Wilson. *The Theory of Metals*. Cambridge University Press, 2 edition, 1958.

[78] X. Lin, B. Fauque, and K. Behnia. Scalable T2 resistivity in a small single-component Fermi surface. *Science*, 349(6251):945–948, August 2015.

[79] Evgeny Mikheev, Burak Himmetoglu, Adam P. Kajdos, Pouya Moetakef, Tyler A. Cain, Chris G. Van de Walle, and Susanne Stemmer. Limitations to the room temperature mobility of two- and three-dimensional electron liquids in $SrTiO_3$. *Applied Physics Letters*, 106(6):062102, February 2015.

[80] Ichiro Nagai, Naoki Shirakawa, Shin-ichi Ikeda, Ryusuke Iwasaki, Hiroshi Nishimura, and Masashi Kosaka. Highest conductivity oxide SrMoO3 grown by a floating-zone method under ultralow oxygen partial pressure. *Applied Physics Letters*, 87(2):024105, July 2005.

[81] Daichi Oka, Yasushi Hirose, Shoichiro Nakao, Tomoteru Fukumura, and Tetsuya Hasegawa. Intrinsic high electrical conductivity of stoichiometric SrNb O 3 epitaxial thin films. *Physical Review B*, 92(20), November 2015.

[82] Youwen Long, Yoshio Kaneko, Shintaro Ishiwata, Yasujiro Taguchi, and Yoshinori Tokura. Synthesis of cubic $SrCoO_3$ single crystal and its anisotropic magnetic and transport properties. *Journal of Physics: Condensed Matter*, 23(24):245601, June 2011.

[83] W. G. Baber. The Contribution to the Electrical Resistance of Metals from Collisions between Electrons. *Proceedings of the Royal Society A: Mathematical, Physical and Engineering Sciences*, 158(894):383–396, January 1937.

[84] Burak Himmetoglu, Anderson Janotti, Hartwin Peelaers, Audrius Alkauskas, and Chris G. Van de Walle. First-principles study of the mobility of SrTiO 3. *Physical Review B*, 90(24), December 2014.

[85] Jin-Jian Zhou, Olle Hellman, and Marco Bernardi. Electron-Phonon Scattering in the Presence of Soft Modes and Electron Mobility in SrTiO3 Perovskite from First Principles. *Physical Review Letters*, 121(22), November 2018. arXiv: 1806.05775.

[86] T. Wolfram. Two-Dimensional Character of the Conduction Bands of d -Band Perovskites. *Physical Review Letters*, 38(6):298–298, February 1977.

[87] Stephen Dongmin Kang and G. Jeffrey Snyder. Transport property analysis method for thermoelectric materials: material quality factor and the effective mass model. *arXiv:1710.06896 [cond-mat]*, October 2017. arXiv: 1710.06896.

[88] Daniel I. Bilc, Geoffroy Hautier, David Waroquiers, Gian-Marco Rignanese, and Philippe Ghosez. Low-Dimensional Transport and Large Thermoelectric Power Factors in Bulk Semiconductors by Band Engineering of Highly Directional Electronic States. *Physical Review Letters*, 114(13), March 2015.

[89] Stephen Dongmin Kang, Maxwell Dylla, and G. Jeffrey Snyder. Thermopower-conductivity relation for distinguishing transport mechanisms: Polaron hopping in CeO 2 and band conduction in SrTiO 3. *Physical Review B*, 97(23), June 2018.

[90] J. Bardeen and W. Shockley. Deformation Potentials and Mobilities in Non-Polar Crystals. *Physical Review*, 80(1):72–80, October 1950.

[91] D Keroack, Y Lepine, and J L Brebner. Drift mobility measurements of small-polaron transport in $SrTiO_3$. *Journal of Physics C: Solid State Physics*, 17(5):833–842, February 1984.

[92] Woo Seok Choi, Hyang Keun Yoo, and Hiromichi Ohta. Polaron Transport and Thermoelectric Behavior in La-Doped $SrTiO_3$ Thin Films with Elemental Vacancies. *Advanced Functional Materials*, 25(5):799–804, February 2015.

[93] Peter A. Sharma, Harlan J. Brown-Shaklee, and Jon F. Ihlefeld. Oxygen partial pressure dependence of thermoelectric power factor in polycrystalline *n* -type $SrTiO_3$: Consequences for long term stability in thermoelectric oxides. *Applied Physics Letters*, 110(17):173901, April 2017.

[94] Amit Verma, Adam P. Kajdos, Tyler A. Cain, Susanne Stemmer, and Debdeep Jena. Intrinsic Mobility Limiting Mechanisms in Lanthanum-Doped Strontium Titanate. *Physical Review Letters*, 112(21), May 2014.

[95] Evgeny Mikheev, Santosh Raghavan, Jack Y. Zhang, Patrick B. Marshall, Adam P. Kajdos, Leon Balents, and Susanne Stemmer. Carrier density independent scattering rate in SrTiO3-based electron liquids. *Scientific Reports*, 6(1), August 2016.

[96] Hiroaki Muta, Ken Kurosaki, and Shinsuke Yamanaka. Thermoelectric properties of doped BaTiO3 - SrTiO3 solid solution. *Journal of Alloys and Compounds*, 368(1-2):22–24, April 2004.

[97] Tyler A. Cain, Adam P. Kajdos, and Susanne Stemmer. La-doped $SrTiO_3$ films with large cryogenic thermoelectric power factors. *Applied Physics Letters*, 102(18):182101, May 2013.

[98] Christian R. Ast and Hartmut HÃűchst. Fermi Surface of Bi(111) Measured by Photoemission Spectroscopy. *Physical Review Letters*, 87(17), October 2001.

[99] V F Gantmakher. The experimental study of electron-phonon scattering in metals. *Reports on Progress in Physics*, 37(3):317–362, March 1974.

[100] Carl A. Kukkonen. T 2 electrical resistivity due to electron-phonon scattering on a small cylindrical Fermi surface: Application to bismuth. *Physical Review B*, 18(4):1849–1853, August 1978.

[101] Lei Feng, Takuma Shiga, and Junichiro Shiomi. Phonon transport in perovskite $SrTiO_3$ from first principles. *Applied Physics Express*, 8(7):071501, July 2015.

[102] Neil W. Ashcroft and N. David Mermin. *Solid State Physics*. Cengage Learning, 1 edition, 1976.

[103] Philip B Allen and William H Butler. Electrical conduction in metals. *PHYSICS TODAY*, page 7, 1978.

[104] Nathan Wiser. The electrical resistivity of the simple metals. *Contemporary Physics*, 25(3):211–249, 1984.

[105] A Duran, F Morales, L Fuentes, and J M Siqueiros. Specific heat anomalies at 37, 105 and 455 K in $SrTiO_3$:Pr. *Journal of Physics: Condensed Matter*, 20(8):085219, February 2008.

[106] Walter A. Harrison. *Electronic Structure and the Properties of Solids: The Physics of the Chemical Bond*. Dover Publications, 1989.

[107] P. A. Cox. *The Electronic Structure and Chemistry of Solids*. Oxford University Press, 2002.

[108] Jeremy K. Burdett. From bonds to bands and molecules to solids. *Progress in Solid State Chemistry*, 15(3):173–255, January 1984.

[109] Roald Hoffmann. How Chemistry and Physics Meet in the Solid State. *Angewandte Chemie International Edition in English*, 26(9):846–878, September 1987.

[110] P. Vogl, Harold P. Hjalmarson, and John D. Dow. A Semi-Empirical Tight-Binding Theory of the Electronic Structure of Semiconductors. *J. Phys. Chem. Solids*, 44(5):365–378, 1983.

[111] Wolfgang G. Zeier, Alex Zevalkink, Zachary M. Gibbs, Geoffroy Hautier, Mercouri G. Kanatzidis, and G. Jeffrey Snyder. Thinking Like a Chemist: Intuition in Thermoelectric Materials. *Angewandte Chemie International Edition*, 55(24):6826–6841, June 2016.

[112] P. Bogusawski and I. Gorczyca. Influence of Chemistry on the Energy Band Structure: AlAs Versus GaAs. *Acta Physica Polonica A*, 80(3):433–436, September 1991.

[113] B. M. Askerov. *Electron transport phenomena in semiconductors*. World Scientific, Singapore ; River Edge, NJ, 1994.

[114] Jiawei Zhou, Hangtian Zhu, Te-Huan Liu, Qichen Song, Ran He, Jun Mao, Zihang Liu, Wuyang Ren, Bolin Liao, David J. Singh, Zhifeng Ren, and Gang Chen. Large thermoelectric power factor from crystal symmetry-protected non-bonding orbital in half-Heuslers. *Nature Communications*, 9(1), December 2018.

[115] Hangtian Zhu, Jun Mao, Yuwei Li, Jifeng Sun, Yumei Wang, Qing Zhu, Guannan Li, Qichen Song, Jiawei Zhou, Yuhao Fu, Ran He, Tian Tong, Zihang Liu, Wuyang Ren, Li You, Zhiming Wang, Jun Luo, Andrei Sotnikov, Jiming Bao, Kornelius Nielsch, Gang Chen, David J. Singh, and Zhifeng Ren. Discovery of TaFeSb-based half-Heuslers with high thermoelectric performance. *Nature Communications*, 10(1), December 2019.

[116] Hangtian Zhu, Ran He, Jun Mao, Qing Zhu, Chunhua Li, Jifeng Sun, Wuyang Ren, Yumei Wang, Zihang Liu, Zhongjia Tang, Andrei Sotnikov, Zhiming Wang, David Broido, David J. Singh, Gang Chen, Kornelius Nielsch, and Zhifeng Ren. Discovery of ZrCoBi based half Heuslers with high thermoelectric conversion efficiency. *Nature Communications*, 9(1), December 2018.

[117] Chenguang Fu, Tiejun Zhu, Yintu Liu, Hanhui Xie, and Xinbing Zhao. Band engineering of high performance p-type FeNbSb based half-Heusler thermoelectric materials for figure of merit zT > 1. *Energy & Environmental Science*, 8(1):216–220, 2015.

[118] Chenguang Fu, Tiejun Zhu, Yanzhong Pei, Hanhui Xie, Heng Wang, G. Jeffrey Snyder, Yong Liu, Yintu Liu, and Xinbing Zhao. High Band Degeneracy Contributes to High Thermoelectric Performance in p-Type Half-Heusler Compounds. *Advanced Energy Materials*, 4(18):1400600, 2014.

[119] A. Tavassoli, F. Failamani, A. Grytsiv, G. Rogl, P. Heinrich, H. Miller, E. Bauer, M. Zehetbauer, and P. Rogl. On the Half-Heusler compounds Nb1-x{Ti,Zr,Hf}xFeSb: Phase relations, thermoelectric properties at low and high temperature, and mechanical properties. *Acta Materialia*, 135:263–276, August 2017.

[120] Elisabeth Rausch, Benjamin Balke, Siham Ouardi, and Claudia Felser. Enhanced thermoelectric performance in the p-type half-Heusler (Ti/Zr/Hf)CoSb $_{0.8}$ Sn $_{0.2}$ system via phase separation. *Phys. Chem. Chem. Phys.*, 16(46):25258–25262, 2014.

[121] Ran He, Hee Seok Kim, Yucheng Lan, Dezhi Wang, Shuo Chen, and Zhifeng Ren. Investigating the thermoelectric properties of p-type half-Heusler Hf $_{x}$ (ZrTi) $_{1-x}$ CoSb $_{0.8}$ Sn $_{0.2}$ by reducing Hf concentration for power generation. *RSC Adv.*, 4(110):64711–64716, 2014.

[122] Slade R. Culp, J. W. Simonson, S. Joseph Poon, V. Ponnambalam, J. Edwards, and Terry M. Tritt. (Zr,Hf)Co(Sb,Sn) half-Heusler phases as high-temperature (>700C) p-type thermoelectric materials. *Applied Physics Letters*, 93(2):022105, July 2008.

[123] Slade R. Culp, S. Joseph Poon, Nicoleta Hickman, Terry M. Tritt, and J. Blumm. Effect of substitutions on the thermoelectric figure of merit of half-Heusler phases at 800 C. *Applied Physics Letters*, 88(4):042106, January 2006.

[124] Junjie Yu, Chenguang Fu, Yintu Liu, Kaiyang Xia, Umut Aydemir, Thomas C. Chasapis, G. Jeffrey Snyder, Xinbing Zhao, and Tiejun Zhu. Unique Role of Refractory Ta Alloying in Enhancing the Figure of Merit of NbFeSb Thermoelectric Materials. *Advanced Energy Materials*, 8(1):1701313, January 2018.

[125] P. G. Klemens. Thermal Resistance due to Point Defects at High Temperatures. *Physical Review*, 119(2):507–509, July 1960.

[126] J. Yang, G. P. Meisner, and L. Chen. Strain field fluctuation effects on lattice thermal conductivity of ZrNiSn-based thermoelectric compounds. *Applied Physics Letters*, 85(7):1140–1142, August 2004.

[127] Heng Wang, Aaron D. LaLonde, Yanzhong Pei, and G. Jeffery Snyder. The Criteria for Beneficial Disorder in Thermoelectric Solid Solutions. *Advanced Functional Materials*, 23(12):1586–1596, March 2013.

[128] Ian T. Witting, Thomas C. Chasapis, Francesco Ricci, Matthew Peters, Nicholas A. Heinz, Geoffroy Hautier, and G. Jeffrey Snyder. The Thermoelectric Properties of Bismuth Telluride. *Advanced Electronic Materials*, 5(6):1800904, June 2019.

[129] Max Wood, Umut Aydemir, Saneyuki Ohno, and G. Jeffrey Snyder. Observation of valence band crossing: the thermoelectric properties of CaZn $_2$ Sb $_2$ - CaMg $_2$ Sb $_2$ solid solution. *Journal of Materials Chemistry A*, 6(20):9437–9444, 2018.

[130] Kazuki Imasato, Stephen Dongmin Kang, Saneyuki Ohno, and G. Jeffrey Snyder. Band engineering in Mg $_3$ Sb $_2$ by alloying with Mg $_3$ Bi $_2$ for enhanced thermoelectric performance. *Materials Horizons*, 5(1):59–64, 2018.

[131] Wen Li, Linglang Zheng, Binghui Ge, Siqi Lin, Xinyue Zhang, Zhiwei Chen, Yunjie Chang, and Yanzhong Pei. Promoting SnTe as an Eco-Friendly Solution for p-PbTe Thermoelectric via Band Convergence and Interstitial Defects. *Advanced Materials*, 29(17):1605887, May 2017.

[132] Jiawei Zhang, Lirong Song, Georg K. H. Madsen, Karl F. F. Fischer, Wenqing Zhang, Xun Shi, and Bo B. Iversen. Designing high-performance layered thermoelectric materials through orbital engineering. *Nature Communications*, 7(1), April 2016.

[133] Jun He, Xiaojian Tan, Jingtao Xu, Guo-Qiang Liu, Hezhu Shao, Yajie Fu, Xue Wang, Zhu Liu, Jiaqiang Xu, Haochuan Jiang, and Jun Jiang. Valence band engineering and thermoelectric performance optimization in SnTe by Mn-alloying via a zone-melting method. *Journal of Materials Chemistry A*, 3(39):19974–19979, 2015.

[134] Yanzhong Pei, Heng Wang, and G. J. Snyder. Band Engineering of Thermoelectric Materials. *Advanced Materials*, 24(46):6125–6135, December 2012.

[135] Shashwat Anand, Kaiyang Xia, Vinay I. Hegde, Umut Aydemir, Vancho Kocevski, Tiejun Zhu, Chris Wolverton, and G. Jeffrey Snyder. A valence balanced rule for discovery of 18-electron half-Heuslers with

defects. *Energy & Environmental Science*, 11(6):1480–1488, 2018.

[136] P. E. BlÃČÂűchl. Projector augmented-wave method. *Physical Review B*, 50(24):17953–17979, December 1994.

[137] G. Kresse and J. Furthmuller. Efficiency of ab-initio total energy calculations for metals and semiconductors using a plane-wave basis set. *Computational Materials Science*, 6(1):15–50, July 1996.

[138] Neil W. Ashcroft and N. David Mermin. *Solid State Physics*. Brooks/Cole, 1976.

[139] Maxwell Thomas Dylla, Stephen Dongmin Kang, and G. Jeffrey Snyder. Effect of Two-Dimensional Crystal Orbitals on Fermi Surfaces and Electron Transport in Three-Dimensional Perovskite Oxides. *Angewandte Chemie*, 131(17):5557–5566, April 2019.

[140] Nicola Marzari, Arash A. Mostofi, Jonathan R. Yates, Ivo Souza, and David Vanderbilt. Maximally localized Wannier functions: Theory and applications. *Reviews of Modern Physics*, 84(4):1419–1475, October 2012.

[141] Jifeng Sun and David J. Singh. Thermoelectric properties of n -type $SrTiO_3$. *APL Materials*, 4(10):104803, October 2016.

[142] Koun Shirai and Kazunori Yamanaka. Mechanism behind the high thermoelectric power factor of $SrTiO_3$ by calculating the transport coefficients. *Journal of Applied Physics*, 113(5):053705, February 2013.

[143] Anubhav Jain, Shyue Ping Ong, Geoffroy Hautier, Wei Chen, William Davidson Richards, Stephen Dacek, Shreyas Cholia, Dan Gunter, David Skinner, Gerbrand Ceder, and Kristin A. Persson. Commentary: The Materials Project: A materials genome approach to accelerating materials innovation. *APL Materials*, 1(1):011002, July 2013.

[144] Weishu Liu, Zhifeng Ren, and Gang Chen. Nanostructured Thermoelectric Materials. In Kunihito Koumoto and Takao Mori, editors, *Thermoelectric Nanomaterials: Materials Design and Applications*, pages 255–285. Springer Berlin Heidelberg, Berlin, Heidelberg, 2013.

[145] Jing-Feng Li, Wei-Shu Liu, Li-Dong Zhao, and Min Zhou. High-performance nanostructured thermoelectric materials. *NPG Asia Materials*, 2(4):152–158, October 2010.

[146] A. J. Minnich, M. S. Dresselhaus, Z. F. Ren, and G. Chen. Bulk nanostructured thermoelectric materials: current research and future prospects. *Energy & Environmental Science*, 2(5):466, 2009.

[147] M. P. Harmer. The Phase Behavior of Interfaces. *Science*, 332(6026):182–183, April 2011.

[148] Shen J. Dillon, Ming Tang, W. Craig Carter, and Martin P. Harmer. Complexion: A new concept for kinetic engineering in materials science. *Acta Materialia*, 55(18):6208–6218, October 2007.

[149] Christoph Freysoldt, Blazej Grabowski, Tilmann Hickel, JÃűrg Neugebauer, Georg Kresse, Anderson Janotti, and Chris G. Van de Walle. First-principles calculations for point defects in solids. *Reviews of Modern Physics*, 86(1):253–305, March 2014.

[150] C. B. Vining and G. D. Mahan. The *B* factor in multilayer thermionic refrigeration. *Journal of Applied Physics*, 86(12):6852–6853, December 1999.

[151] Xanthippi Zianni and Dario Narducci. Parametric modeling of energy filtering by energy barriers in thermoelectric nanocomposites. *Journal of Applied Physics*, 117(3):035102, January 2015.

[152] Roger A De Souza. The formation of equilibrium space-charge zones at grain boundaries in the perovskite oxide SrTiO3. *Physical Chemistry Chemical Physics*, 11:9939–9969, 2009.

[153] C. T. Koch. Determination of grain boundary potentials in ceramics: Combining impedance spectroscopy and inline electron holography. *International Journal of Materials Research*, 101(1):43–49, January 2010.

[154] Venkataraman Ravikumar, Richard P. Rodrigues, and Vinayak P. Dravid. Space-Charge Distribution across Internal Interfaces in Electroceramics Using Electron Holography: II, Doped Grain Boundaries. *Journal of the American Ceramic Society*, 80(5):1131–1138, January 2005.

[155] Y. G Wang and V. P Dravid. Determination of electrostatic characteristics at a 24 deg, [001] tilt grain boundary in a SrTiO $_3$ bicrystal by electron holography. *Philosophical Magazine Letters*, 82(8):425–432, August 2002.

[156] Kevin D. Johnson and Vinayak P. Dravid. Grain boundary barrier breakdown in niobium donor doped strontium titanate using *in situ* electron holography. *Applied Physics Letters*, 74(4):621–623, January 1999.

[157] H. Trabelsi, M. Bejar, E. Dhahri, M. Sajieddine, K. Khirouni, P.R. Prezas, B.M.G. Melo, M.A. Valente, and M.P.F. Graca. Effect of oxygen vacancies on SrTiO electrical properties. *Journal of Alloys and Compounds*, 723:894–903, November 2017.

[158] Stefan Rodewald, Jurgen Fleig, and Joachim Maier. Microcontact Impedance Spectroscopy at Single Grain Boundaries in Fe-Doped SrTiO $_3$ Polycrystals. *Journal of the American Ceramic Society*, 84(3):521–530, March 2001.

[159] Rainer Waser. Electronic properties of grain boundaries in SrTi03 and BaTiO, ceramics. *Solid State Ionics*, 75:89–99, 1995.

[160] Markus Vollman and Rainer Waser. Grain Boundary Defect Chemistry of Acceptor-Doped Titanates: Space Charge Layer Width. *Journal of the American Ceramic Society*, 77(1):235–243, January 1994.

[161] Roger A. De Souza, Veronika Metlenko, Daesung Park, and Thomas E. Weirich. Behavior of oxygen vacancies in single-crystal SrTiO 3 : Equilibrium distribution and diffusion kinetics. *Physical Review B*, 85(17), May 2012.

[162] H.-S. Lee, T. Mizoguchi, J. Mistui, T. Yamamoto, S.-J. L. Kang, and Y. Ikuhara. Defect energetics in SrTiO 3 symmetric tilt grain boundaries. *Physical Review B*, 83(10), March 2011.

[163] M. Imaeda, T. Mizoguchi, Y. Sato, H.-S. Lee, S. D. Findlay, N. Shibata, T. Yamamoto, and Y. Ikuhara. Atomic structure, electronic structure, and defect energetics in [001] (310) sigam-5 grain boundaries of SrTiO 3 and BaTiO 3. *Physical Review B*, 78(24), December 2008.

[164] Hak-Sung Lee, Teruyasu Mizoguchi, Takahisa Yamamoto, Suk-Joong L. Kang, and Yuichi Ikuhara. First-principles calculation of defect energetics in cubic-BaTiO3 and a comparison with SrTiO3. *Acta Materialia*, 55(19):6535–6540, November 2007.

[165] Peng-an Zong, Riley Hanus, Maxwell Dylla, Yunshan Tang, Jingcheng Liao, Qihao Zhang, G. Jeffrey Snyder, and Lidong Chen. Skutterudite with graphene-modified grain-boundary complexion enhances zT enabling high-efficiency thermoelectric device. *Energy & Environmental Science*, 10(1):183–191, 2017.

[166] Wei-Lung Tzeng, Hung-Wei Yen, Wen-Chin Lin, and Shao-Ju Shih. Grain boundary engineering for improving conductivity of polycrystalline SrTiO3. *Ceramics International*, 43(2):2361–2367, February 2017.

[167] M Leonhardt, J Jamnik, and J Maier. In Situ Monitoring and Quantitative Analysis of Oxygen Diffusion Through Schottky-Barriers in SrTiO3 Bicrystals. *Electrochemical and Solid-State Letters*, 2(7):333–335, 1999.

[168] S Hutt, S Kostlmeier, and C Elsasser. Density functional study of the sigma-3 (111) [110] symmetrical tilt grain boundary in SrTiO3. *J. Phys. Condens. Matter*, 13:3949–3960, 2001.

[169] Anubhav Jain, Geoffroy Hautier, Charles J. Moore, Shyue Ping Ong, Christopher C. Fischer, Tim Mueller, Kristin A. Persson, and Gerbrand Ceder. A high-throughput infrastructure for density functional theory calculations. *Computational Materials Science*, 50(8):2295–2310, June 2011.

[170] James E. Saal, Scott Kirklin, Muratahan Aykol, Bryce Meredig, and C. Wolverton. Materials Design and Discovery with High-Throughput Density Functional Theory: The Open Quantum Materials Database (OQMD). *JOM*, 65(11):1501–1509, November 2013.

[171] Scott Kirklin, James E Saal, Bryce Meredig, Alex Thompson, Jeff W Doak, Muratahan Aykol, Stephan Ruhl, and Chris Wolverton. The Open Quantum Materials Database (OQMD): assessing the accuracy of DFT formation energies. *npj Computational Materials*, 1(1), December 2015.

[172] Nils E. R. Zimmermann, Matthew K. Horton, Anubhav Jain, and Maciej Haranczyk. Assessing Local Structure Motifs Using Order Parameters for Motif Recognition, Interstitial Identification, and Diffusion Path Characterization. *Frontiers in Materials*, 4, November 2017.

[173] Logan Ward, Alexander Dunn, Alireza Faghaninia, Nils E.R. Zimmermann, Saurabh Bajaj, Qi Wang, Joseph Montoya, Jiming Chen, Kyle Bystrom, Maxwell Dylla, Kyle Chard, Mark Asta, Kristin A. Persson, G. Jeffrey Snyder, Ian Foster, and Anubhav Jain. Matminer: An open source toolkit for materials data mining. *Computational Materials Science*, 152:60–69, September 2018.

[174] Wolfgang G. Zeier, Shashwat Anand, Lihong Huang, Ran He, Hao Zhang, Zhifeng Ren, Chris Wolverton, and G. Jeffrey Snyder. Using the 18-Electron Rule To Understand the Nominal 19-Electron Half-Heusler NbCoSb with Nb Vacancies. *Chemistry of Materials*, 29(3):1210–1217, February 2017.

[175] Lauryn L. Baranowski, G. Jeffrey Snyder, and Eric S. Toberer. Response to comment on effective thermal conductivity in thermoelectric materials [j. appl. phys. 113, 204904 (2013)]. *Journal of Applied Physics*, 115(12):126102, 2014.

[176] Daniel I. Bilc, Calin G. Floare, Liviu P. ZÃćrbo, Sorina Garabagiu, Sebastien Lemal, and Philippe Ghosez. First-Principles Modeling of $SrTiO_3$ Based Oxides for Thermoelectric Applications. *The Journal of Physical Chemistry C*, 120(45):25678–25688, November 2016.

[177] J.W. Sharp, S.J. Poon, and H.J. Goldsmid. Boundary Scattering and the Thermoelectric Figure of Merit. *physica status solidi (a)*, 187(2):507–516, October 2001.

[178] Matthias T. Agne, Riley Hanus, and G. Jeffrey Snyder. Minimum thermal conductivity in the context of *diffuson* -mediated thermal transport. *Energy & Environmental Science*, 11(3):609–616, 2018.

[179] Nicola Marzari and David Vanderbilt. Maximally localized generalized Wannier functions for composite energy bands. *Physical Review B*, 56(20):12847–12865, November 1997.

[180] Koichi Momma and Fujio Izumi. *VESTA* : a three-dimensional visualization system for electronic and structural analysis. *Journal of Applied Crystallography*, 41(3):653–658, June 2008.

[181] Anton Kokalj. XCrySDen-a new program for displaying crystalline structures and electron densities. *Journal of Molecular Graphics and Modelling*, 17(3-4):176–179, June 1999.

[182] Toshio Fukushima. Precise and fast computation of Fermi-Dirac integral of integer and half integer order by piecewise minimax rational approximation. *Applied Mathematics and Computation*, 259:708–729, May 2015.

[183] Peter E. Blochl, O. Jepsen, and O. K. Andersen. Improved tetrahedron method for Brillouin-zone integrations. *Physical Review B*, 49(23):16223–16233, June 1994.

[184] Shyue Ping Ong, William Davidson Richards, Anubhav Jain, Geoffroy Hautier, Michael Kocher, Shreyas Cholia, Dan Gunter, Vincent L. Chevrier, Kristin A. Persson, and Gerbrand Ceder. Python Materials Genomics (pymatgen): A robust, open-source python library for materials analysis. *Computational Materials Science*, 68:314–319, February 2013.

[185] Fabian Pedregosa, Gael Varoquaux, Alexandre Gramfort, Vincent Michel, Bertrand Thirion, Olivier Grisel, Mathieu Blondel, Peter Prettenhofer, Ron Weiss, Vincent Dubourg, Jake Vanderplas, Alexandre Passos, and David Cournapeau. Scikit-learn: Machine Learning in Python. *MACHINE LEARNING IN PYTHON*, page 6.

APPENDIX A

Power from a Thermoelectric Device

Thermoelectric materials are used in both Peltier coolers and thermoelectric generators; as a case study, we will investigate power generation from a material with resistance R_{TE} connected to a load resistor R_{L}. The power at the load resistor is generated from a current I_{TE} driven by the thermoelectric voltage $V_{\text{TE}} = \alpha\Delta T$, where ΔT is the temperature drop across the thermoelectric material. The generated power $P = I_{\text{TE}}^2 R_{\text{L}}$ becomes

$$P = \frac{\alpha^2 \Delta T^2}{(R_{\text{TE}} + R_{\text{L}})^2} R_{\text{L}}. \tag{A.1}$$

By being able to freely adjust the R_{L} to R_{TE} ratio ($m = R_{\text{L}}/R_{\text{TE}}$), the power becomes

$$P \propto \alpha^2 \sigma \Delta T^2 \cdot \frac{m}{(1+m)^2}. \tag{A.2}$$

The power is maximized when the power dissipated by joule heating in the thermoelectric material is matched by the power dissipated by the load resistor ($m = 1$). We see that the maximum power is proportional to the power factor $\alpha^2\sigma$ and that low thermal conductivity is inherently needed for power generation, because it determines the magnitude of the achievable temperature drop (ΔT) in the thermoelectric material. For optimizing power in an actual device, considering the heat exchanger and thermal impedance matching introduce interdependencies that make the optimization problem more than just optimizing power factor[175].

APPENDIX B

Heat Transport from Electrons and Lattice Vibrations

The general current density equation (Eq. 1.3) can be adopted for heat transport by exchanging the charge per particle with the energy per particle ($q \to \partial Q/\partial c$). Since the heat carried per particle depends on energy, it is pulled into the integral,

$$J_Q = -\int_{-\infty}^{\infty} \frac{\partial Q}{\partial c} G(E) \nabla f dE \ . \tag{B.1}$$

The heat carried by a fermion is referenced to its chemical potential, while the heat carried by a boson is on an absolute energy scale

$$\frac{\partial Q_f}{\partial c} = E - \mu \ , \tag{B.2}$$

$$\frac{\partial Q_b}{\partial c} = E \ . \tag{B.3}$$

We can now derive the heat transport induced from electric fields and temperature gradients. The derivations will follow the same flow as the sections on charge transport. Chain rules will relate voltage and temperature gradients to gradients in occupation statistics; then, Onsager relations will elucidate measurable quantities. We will encounter two new *selection functions* for heat transport

B.0.0.1. Electronic thermal conductivity. In the sections on charge transport, we derived the current densities induced from voltage and temperature gradients (Eqs. 1.4, 1.6). We can apply these results to heat transport by converting the charge carried per-particle to the heat carried per-particle ($q \to E - \mu$). Notice that one unit of charge remains in the voltage equation from converting a chemical potential gradient to a voltage gradient ($\nabla \mu = q \nabla V$),

$$J_{Q,\nabla V} = -q \nabla V \int_{-\infty}^{\infty} G(E) \left(E - \mu\right) \frac{-\partial f}{\partial E} dE \ , \tag{B.4}$$

$$J_{Q,\nabla T} = -\nabla T \int_{-\infty}^{\infty} G(E) \frac{\left(E - \mu\right)^2}{T} \frac{-\partial f}{\partial E} dE \ . \tag{B.5}$$

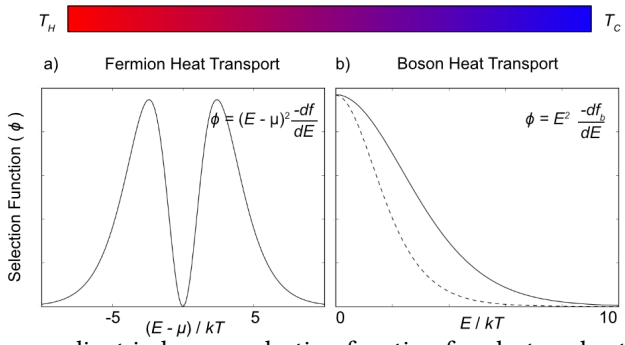

Figure B.1. a) A temperature gradient induces a selection function for electron heat transport, and for b) heat-carrying bosons. The selection function can be interpreted as the per-mode specific heat for phonons. The boson selection function is broader than $-\partial f/\partial E$ (dashed curve).

We have already seen the upper *selection function* when we examined temperature-driven charge transport. The selection function indicates that electrons above the chemical potential carry heat down a voltage gradient, while electrons below the chemical potential oppose this heat-flow. The lower selection function $(E-\mu)^2 \cdot (-\partial f/\partial E)$ is an even function around the electron chemical potential, so heat carried by electrons always flows down a temperature gradient (see Fig. B.1).

Another Onsager coefficient relates the heat current density to an applied temperature gradient ($J_Q = -\kappa_e \nabla T$) at *open-circuit* conditions; this coefficient is the electronic contribution to the thermal conductivity, κ_e,

$$\kappa_e = \left.\frac{J_{Q,\nabla T}}{\nabla T}\right|_{J=0} + \left.\frac{J_{Q,\nabla V}}{\nabla T}\right|_{J=0} . \tag{B.6}$$

There are thus two contributions to κ_e: one driven by a temperature gradient and one driven by a voltage gradient. The temperature term is κ_0,

$$\kappa_0 = \int_{-\infty}^{\infty} G(E) \frac{(E-\mu)^2}{T} \frac{-\partial f}{\partial E} dE, \tag{B.7}$$

and is independent of an applied voltage. We refer to the voltage driven term as κ_1,

$$\kappa_1 = q \left.\frac{\nabla V}{\nabla T}\right|_{J=0} \int_{-\infty}^{\infty} G(E) (E-\mu) \frac{-\partial f}{\partial E} dE . \tag{B.8}$$

We can see that the origin of κ_1 is heat driven by a voltage gradient. Electronic thermal conductivity is defined at *open-circuit* conditions where $\nabla V/\nabla T$ is related to the Seebeck coefficient,

$$\kappa_e = \kappa_0 - \alpha^2 \sigma T \ . \tag{B.9}$$

We can understand Peltier heat currents and heat pumps by relaxing the zero-current condition. Running current through a material decreases ∇V in Eq. B.8. Decreasing the magnitude of the voltage gradient tends to increase the effective electronic thermal conductivity. The voltage driven term allows thermoelectric devices to be used as heat pumps or Peltier coolers. In one configuration, heat is actively pumped across the device whereas reversing the applied voltage results in Peltier cooling.

B.0.0.2. Lattice thermal conductivity. In addition to electrons, atomic vibrations also transport heat. Since vibrational quanta have no charge associated with them, they do not respond to an electric field; the only driving force for heat-flux (barring the formation of a polaron) is a temperature gradient. Landauer theory for heat transport (Eq. B.1) relates the heat flux to the gradient of the carrier statistics. A chain rule relates the spacial gradient of Bose-Einstein statistics with the spacial gradient of the temperature ($\nabla f_b = \partial f_b/\partial T \cdot \nabla T = \frac{E}{T} \cdot -\partial f_b/\partial E \cdot \nabla T$). The Landauer solution for bosonic heat-flux induced from a temperature gradient is

$$J_{Q,\nabla T} = -\nabla T \int_0^\infty G(E) \left(\frac{E^2}{T}\right) \frac{-\partial f_b}{\partial E} dE. \tag{B.10}$$

Notice that the lower limit of the integral is zero, since vibrational quanta energies are measured on an absolute energy scale. Remarkably, the *selection function* for heat carrying bosons ($E^2 \cdot -\partial f_b/\partial E$) is similar to electrons driven by an electric field ($-\partial f/\partial E$); while the boson selection function is the same shape, it is about twice as broad (see Fig. B.1). Therefore, heat carried by bosons always travels down a temperature gradient.

Lattice thermal conductivity relates heat flux to an applied temperature gradient ($J_Q = -\kappa_l \nabla T$),

$$\kappa_l = \int_0^\infty G(E) \left(\frac{E^2}{T}\right) \frac{-\partial f_b}{\partial E} dE \ , \tag{B.11}$$

Expanding the derivative of Bose-Einstein statistics is instructive, since it reveals the per-mode specific heat,

$$\kappa_l = \int_0^\infty G(E) \frac{E^2}{kT^2} \frac{e^{E/kT}}{\left(e^{E/kT} - 1\right)^2} dE \ . \tag{B.12}$$

Readers will typically find lattice thermal conductivity formulated as the product of the energy-dependent transport function $G(E)$ and the per-mode specific heat, though you may need to infer $G(E)$. The non-zero energy span for $G(E)$ in the case of phonons or vibrational modes is smaller than that of fermions, which means that most or all vibrational modes will be active in transport above 300 K. We stress that this derivation applies to more than just phonons, which only exist in crystalline materials; this theory treats vibrational quanta in amorphous materials equally well.

APPENDIX C

A Generaral Formulation of the Relaxation Time

The relaxation time is an important quantity for transport. In essence, it is the time constant that determines how quickly a system returns to the equilibrium distribution function f_0 when an external stimulus is removed. We will be concerned with the distribution function for Fermions.

$$f_0 = \left[\exp\left(\frac{\varepsilon(\mathbf{k}) - \mu}{k_B T}\right) + 1\right]^{-1} \tag{C.1}$$

This chapter will develop a general form of the relaxation time that makes no assumptions on the nature of the scatterer or the electronic states. Then, the influence of electron-phonon processes on the relaxation time will be explored. Particular attention will be turned to the results of scattering by long wavelength acoustic modes for anisotropic electron dispersions. In principle, we will find that longitudinal and shear displacements by phonons can contribute to scattering.

C.1. A general description of the relaxation time

According to the Boltzmann equation, the rate-of-change of the non-equilibrium distribution function f is the sum of occupational changes from diffusion, field-driven, and scattering processes.

$$\partial f/\partial t = (\partial f/\partial t)_{diff} + (\partial f/\partial t)_{field} + (\partial f/\partial t)_{scat} \tag{C.2}$$

For the influence of scattering on the distribution function, consider the probability $W(\mathbf{k}, \mathbf{k}')$ that an initial state $\mathbf{k}$ scatters into a final state $\mathbf{k}'$. The total change in the occupation is a sum of possible scattering processes (both in-to and out-of a state $\mathbf{k}$) weighted by the occupation of the initial and final states, which reflects the Pauli

exclusion principle for Fermions.

$$\left(\partial f/\partial t\right)_{scat} = \sum_{\mathbf{k}'} \left\{ W\left(\mathbf{k}', \mathbf{k}\right) f\left(\mathbf{k}'\right) \left[1 - f\left(\mathbf{k}\right)\right] - W\left(\mathbf{k}, \mathbf{k}'\right) f\left(\mathbf{k}\right) \left[1 - f\left(\mathbf{k}'\right)\right] \right\} \tag{C.3}$$

For the remaining terms of the Boltzmann equation, the diffusion term is proportional to the particle velocity $\mathbf{v}\left(\mathbf{k}\right)$ and the spacial gradient of f, while the field term is proportional to the external driving force $\mathbf{F}$ and the state-dependent gradient of f. We have now established the form for each term of the Boltzmann equation.

$$\left(\partial f/\partial t\right)_{diff} = -\mathbf{v}\left(\mathbf{k}\right) \nabla_{\mathbf{r}} f \tag{C.4}$$

$$\left(\partial f/\partial t\right)_{field} = -\hbar^{-1} \mathbf{F} \nabla_{\mathbf{k}} f \tag{C.5}$$

In the linear regime, when the perturbing stimuli are weak, the non-equilibrium distribution function can be defined as an additive perturbation from the equilibrium distribution function f_0.

$$f\left(\mathbf{k}\right) = f_0\left(\mathbf{k}\right) + f_1\left(\mathbf{k}\right) \tag{C.6}$$

The additive form of the non-equilibrium distribution function (f) allows us to separate contributions from the equilibrium distribution function (f_0) from non-equilibrium terms (f_1) in the scattering expression. The mathematical details of this simplification can be found in Askerov, but the result is an expression formulated in terms of the relaxation time (τ) notation. The relaxation time can be interpreted as the time constant that controls how fast the non-equilibrium distribution function evolves into the equilibrium distribution function when the perturbing stimulus is turned off.

$$\left(\partial f/\partial t\right)_{scat} = -f_1\left(\mathbf{k}\right)/\tau\left(\mathbf{k}\right). \tag{C.7}$$

The relaxation time is formulated in terms of transition probabilities and the equilibrium and non-equilibrium terms of the distribution function. Knowledge of the non-equilibrium distribution function is required to specify the relaxation time; the relaxation time does not merely depend on transition probabilities.

$$\frac{1}{\tau\left(\mathbf{k}\right)} = \sum_{\mathbf{k}'} W\left(\mathbf{k}, \mathbf{k}'\right) \left\{ \frac{1 - f_0\left(\varepsilon'\right)}{1 - f_0\left(\varepsilon\right)} - \frac{f_0\left(\varepsilon\right)}{f_0\left(\varepsilon'\right)} \frac{f_1\left(\mathbf{k}'\right)}{f_1\left(\mathbf{k}\right)} \right\} \tag{C.8}$$

Thus far, we have only assumed that the perturbation from the equilibrium distribution function is small so that we need to only deal in linear terms of f_1. We will now need to solve for the non-equilibrium distribution function to completely specify the relaxation time.

To solve for the non-equilibrium distribution function, we need to consider the diffusion and field terms of the Boltzmann equation. The additive form of the non-equilibrium distribution function (Eq. C.6) simplifies the diffusion and field terms; since f_1 is small, it can be neglected so that the spacial/state-dependent gradients are functions of f_0 only.

$$\nabla_{\mathbf{k}} f \approx \left(\partial f_0/\partial \varepsilon\right)\left(\partial \varepsilon/\partial \mathbf{k}\right) \tag{C.9}$$

$$\nabla_{\mathbf{r}} f \approx k_B T\left(\partial f_0/\partial \varepsilon\right)\nabla_{\mathbf{r}} \frac{\varepsilon-\mu\left(\mathbf{r}\right)}{k_B T\left(\mathbf{r}\right)} \tag{C.10}$$

In the steady state, where the non-equilibrium distribution function is not evolving with time, the solution to the Boltzmann equation is now a function of a generalized disturbing force Φ, which is responsible for the deviation from the equilibrium distribution function.

$$f\left(\mathbf{k}\right) = f_0\left(\mathbf{k}\right) - \tau\left(\mathbf{k}\right)\left[\mathbf{v}\left(\mathbf{k}\right)\Phi\left(\varepsilon\right)\right]\left(\partial f_0/\partial \varepsilon\right), \tag{C.11}$$

In the absence of a magnetic field, the disturbing force depends on both the electrochemical potential gradient ($\tilde{\mu} = \mu - e\phi$, where ϕ is the electrostatic potential), and the temperature gradient. In specifying Φ, we have made the assumption that we are in a linear regime, where the spacial gradients of chemical potential and temperature (Eq. C.10) are linearly separable.

$$\Phi\left(\varepsilon\right) = -\nabla\tilde{\mu} - \frac{\varepsilon-\mu}{T}\nabla T \tag{C.12}$$

Having determined the non-equilibrium distribution function, we can now write the relaxation time in terms of the generalized disturbing force. Notice that this expression only depends on the equilibrium distribution function, but may require an iterative method to solve since it depends on the relaxation time itself.

$$\frac{1}{\tau\left(\mathbf{k}\right)} = \sum_{\mathbf{k}'} W\left(\mathbf{k},\mathbf{k}'\right)\frac{1-f_0\left(\varepsilon'\right)}{1-f_0\left(\varepsilon\right)}\left\{1-\frac{\tau\left(\mathbf{k}'\right)}{\tau\left(\mathbf{k}\right)}\frac{\mathbf{v}\left(\mathbf{k}'\right)\Phi\left(\varepsilon'\right)}{\mathbf{v}\left(\mathbf{k}\right)\Phi\left(\varepsilon\right)}\right\} \tag{C.13}$$

This form of the relaxation time is general for any disturbance that is weak, so the non-equilibrium distribution function must be only a small perturbation from the equilibrium distribution function. Besides that they are Fermions, no assumptions of the nature of the electronic states have been made.

C.2. Calculating transition probabilities

From the preceding analysis, it can be seen that calculating the transition probabilities between quantum states is intrinsic to the problem of calculating the relaxation time. The transition probability during unit time is given by a matrix element that depends on the perturbing Hamiltonian $\hat{\mathcal{H}}'$. Energy of the quantum states before (n) and after (n') the transition must be conserved. This result is derived from time-dependent perturbation theory and is colloquially known as Fermi's golden rule.

$$W\left(n,n'\right)=\frac{2\pi}{\hbar}\left|\left\langle n'|\hat{\mathcal{H}}'|n\right\rangle\right|^{2}\delta\left(\varepsilon_{n'}-\varepsilon_{n}\right) \tag{C.14}$$

The matrix elements are calculated as spacial integrals of the initial and final (unperturbed) wave functions.

$$\left\langle n'|\hat{\mathcal{H}}'|n\right\rangle=\int\psi_{n'}^{*}\hat{\mathcal{H}}'\psi_{n}d\mathbf{r} \tag{C.15}$$

To begin calculating transition probabilities, forms for the unperturbed states and the perturbing Hamiltonian must be found. The form of the perturbing Hamiltonian will depend on the scattering source.

C.3. Electronic scattering by acoustic phonons

In principle, the atomic displacement vector $\mathbf{u}_{nk}$ for the kth atom in the nth cell of a crystal with N total cells is a sum of the displacements from all phonon wave vectors $\{\mathbf{q}\}$ from all branches $\{j\}$.

$$\mathbf{u}_{nk}=\frac{1}{\sqrt{N}}\sum_{\mathbf{q}j}\left\{\mathbf{e}_{kj}\left(\mathbf{q}\right)b_{j}\left(\mathbf{q}\right)\exp\left(i\mathbf{q}\mathbf{a}_{n}\right)+\mathbf{e}_{kj}^{*}\left(\mathbf{q}\right)b_{j}^{*}\left(\mathbf{q}\right)\exp\left(-i\mathbf{q}\mathbf{a}_{n}\right)\right\} \tag{C.16}$$

Here, $\mathbf{e}_{kj}\left(\mathbf{q}\right)$ is the oscillation direction of the kth atom, and $\mathbf{a}_{n}$ is the lattice vector of the nth cell. Furthermore, $b_{j}\left(\mathbf{q}\right)$ is the complex time dependent coordinates of phonon $\mathbf{q}$ from branch j with energy $\omega_{j}\left(\mathbf{q}\right)$.

$$b_{j}\left(\mathbf{q}\right)\sim\exp\left(-i\omega_{j}\left(\mathbf{q}\right)t\right) \tag{C.17}$$

It is convenient to disregard the effect of individual atomic positions and investigate electron-phonon scattering in the continuum limit. This simplification is especially applicable when considering long wavelength acoustic phonons; the phonon wavelength is much larger than the atomic spacing, and all k atoms oscillate in phase. There is now no explicit dependence on k and n in the displacement vector, and the unit cell vector $\mathbf{a}_n$ is replaced by a continuous position vector $\mathbf{r}$. Furthermore $\mathbf{e}_j$ is now a unit vector ($\mathbf{e}_j \rightarrow \hat{\mathbf{e}}_j$). When only counting acoustic modes, the sum over the branches $\{j\}$ will run from 1-3.

$$\mathbf{u}_{ac} = \frac{1}{\sqrt{N}} \sum_{\mathbf{q}j} \hat{\mathbf{e}}_j \left(\mathbf{q}\right) \left\{ b_j \left(\mathbf{q}\right) \exp\left(i\mathbf{q}\mathbf{r}\right) + b_j^* \left(\mathbf{q}\right) \exp\left(-i\mathbf{q}\mathbf{r}\right) \right\} \tag{C.18}$$

In the deformation potential method, the perturbing Hamiltonian is a tensor quantity related to the linear shift in energy $E_{1\alpha\beta}$ with changing deformation $u_{\alpha\beta}$. Note that element-wise multiplication is implied.

$$\hat{\mathcal{H}}'_{ac} = \sum_{\alpha\beta} \hat{\mathcal{H}}'_{\alpha\beta} = \sum_{\alpha\beta} \sum_{j} E^j_{1\alpha\beta} u^j_{\alpha\beta} \tag{C.19}$$

In the limit of small displacements, the deformation tensor elements are given by the derivatives of the displacement components ($u\left(\mathbf{r}\right) = u\left(\sum_{i=1}^{3} a_i \hat{\mathbf{x}}_i\right)$) with respect to the component directions.

$$u_{\alpha\beta} = \frac{1}{2} \left(\frac{\partial u_\alpha}{\partial x_\beta} + \frac{\partial u_\beta}{\partial x_\alpha} \right) \tag{C.20}$$

Calculating the deformation tensor informs the functional dependence of the perturbing Hamiltonian. In principle, both diaganal and shear components of the tensor should be considered.

$$\hat{\mathcal{H}}'_{\alpha\beta} = \frac{iE_{1\alpha\beta}}{2\sqrt{N}} \sum_{\mathbf{q}j} \left\{ q_\alpha \hat{\mathbf{x}}_\beta \hat{\mathbf{e}}_j \left(\mathbf{q}\right) + q_\beta \hat{\mathbf{x}}_\alpha \hat{\mathbf{e}}_j \left(\mathbf{q}\right) \right\} \left\{ b_j \left(\mathbf{q}\right) \exp\left(i\mathbf{q}\mathbf{r}\right) - b_j^* \left(\mathbf{q}\right) \exp\left(-i\mathbf{q}\mathbf{r}\right) \right\} \tag{C.21}$$

The total purturbation is given by a sum over the perturbations from every deformation mode.

$$\hat{\mathcal{H}}'_{ac} = \sum_{\alpha\beta} \frac{iE_{1\alpha\beta}}{2\sqrt{N}} \sum_{\mathbf{q}j} \left\{ q_\alpha \hat{\mathbf{x}}_\beta \hat{\mathbf{e}}_j \left(\mathbf{q}\right) + q_\beta \hat{\mathbf{x}}_\alpha \hat{\mathbf{e}}_j \left(\mathbf{q}\right) \right\} \left\{ b_j \left(\mathbf{q}\right) \exp\left(i\mathbf{q}\mathbf{r}\right) - b_j^* \left(\mathbf{q}\right) \exp\left(-i\mathbf{q}\mathbf{r}\right) \right\} \tag{C.22}$$

In addition, when the scattering source is itself part of the quantum system, its wave function must be included in the specification of initial and final states. For example the initial and final states for electron-phonon

scattering are given by a product of the electron ($\psi_{\mathbf{k}}$) and phonon ($\phi_{N_{\mathbf{q}j}}$) wave functions.

$$\psi_n = \psi_k \prod_{\mathbf{q}j} \phi_{N_{\mathbf{q}j}} \tag{C.23}$$

In the case of phonons, the initial and final quantum states are specified by quantum numbers related to both the electron and phonon states. $\mathbf{k}$ is used to specify the electron states, while $N_{\mathbf{q}j}$ specifies the number of phonons at wave vector $\mathbf{q}$ in branch j. Therefore the electron-phonon quantum system is specified by the quantum state $n \implies (\mathbf{k}, N_{\mathbf{q}j})$. The transition frequency from one quantum state to another depends on both the electron and phonon states.

$$W\left(\mathbf{k}N_{\mathbf{q},j}, \mathbf{k}'N'_{\mathbf{q},j}\right) = \frac{2\pi}{\hbar}\left|\left\langle \mathbf{k}'N'_{\mathbf{q},j}|\hat{\mathcal{H}}'|\mathbf{k}N_{\mathbf{q},j}\right\rangle\right|^2 \delta\left(\varepsilon_{k'} - \varepsilon_k + \sum_{\mathbf{q}j}\left(N'_{\mathbf{q}j} - N_{\mathbf{q}j}\right)\hbar\omega_j\left(\mathbf{q}\right)\right) \tag{C.24}$$

Total energy conservation considers both the electron energies ε and phonon energies $\hbar\omega$. Since computing the relaxation time for electrons concerns the transitions from state $\mathbf{k}$ to $\mathbf{k}'$, we must sum over all the phonon states of the system.

$$W\left(\mathbf{k}, \mathbf{k}'\right) = \sum_{N'_{\mathbf{q}j}} W\left(\mathbf{k}N_{\mathbf{q},j}, \mathbf{k}'N'_{\mathbf{q},j}\right) \tag{C.25}$$

APPENDIX D

Transport from Low-Dimensional Carrier Pockets

D.1. Anisotropic limit of ellipsoidal pockets: cylinders

Consider a prolate, ellipsoidal carrier pocket. The dispersion of this pocket is characterized by a light mass (m_l^*) in two directions and a heavy mass in the third direction (m_h^*).

$$\varepsilon = \hbar^2 \left(\frac{k_x^2 + k_y^2}{2m_l^*} + \frac{k_z^2}{2m_h^*} \right) \tag{D.1}$$

The band edge of this carrier pocket is the point ($k_x = k_y = k_z = 0$) in k-space, and Fermi surfaces of the carrier pocket are prolate ellipsoids. In the limit of an extremely heavy mass ($m_h^* \to \infty$) there is no dispersion in the heavy direction.

$$\varepsilon = \frac{\hbar^2 \left(k_x^2 + k_y^2 \right)}{2m^*} = \frac{\hbar^2 r^2}{2m^*} \tag{D.2}$$

The band edge of this carrier pocket is now the *line* ($k_x = k_y = 0$), and Fermi surfaces of this carrier pocket are *cylinders*. The length of the cylinder is restricted by the size of the first Brillouin zone. Since the electron group velocity in zero in the heavy mass direction, the conductivity tensor has only two non-zero elements (σ^*) they are in the directions perpendicular to the cylindrical axis.

$$\sigma_{ij} = \begin{bmatrix} \sigma^* & 0 & 0 \\ 0 & \sigma^* & 0 \\ 0 & 0 & 0 \end{bmatrix} \tag{D.3}$$

The transport tensor ν (which is the numerator of the Seebeck coefficient for isotropic systems) is also anisotropic.

$$\nu_{ij} = \begin{bmatrix} \nu^* & 0 & 0 \\ 0 & \nu^* & 0 \\ 0 & 0 & 0 \end{bmatrix} \tag{D.4}$$

We will see that three orthogonal cylindrical pockets give isotropic transport coefficients.

D.2. Three orthogonal cylindrical pockets

The total conductivity tensor from multiple carrier pockets is given by element-wise addition[40]. The conductivity from three pockets is now isotropic.

$$\sigma_{ij} = \sum_k \sigma_{ij,k} = 2\sigma^* \begin{bmatrix} 1 & 0 & 0 \\ 0 & 1 & 0 \\ 0 & 0 & 1 \end{bmatrix} \tag{D.5}$$

Likewise, ν adds element-wise for multiple carrier pockets.

$$\nu_{ij} = \sum_k \nu_{ij,k} = 2\nu^* \begin{bmatrix} 1 & 0 & 0 \\ 0 & 1 & 0 \\ 0 & 0 & 1 \end{bmatrix} \tag{D.6}$$

The total seebeck coefficient for multiple carrier pockets is then given in terms of σ and ν.

$$\alpha_{ij} = \sigma_{\alpha i}^{-1} \nu_{\alpha j} = \frac{\nu^*}{\sigma^*} \begin{bmatrix} 1 & 0 & 0 \\ 0 & 1 & 0 \\ 0 & 0 & 1 \end{bmatrix} = \alpha^* \tag{D.7}$$

Since both the conductivity and Seebeck coefficient are isotropic, we need to only compute one of the tensor elements from a single cylindrical pocket (σ^* and α^*) to determine the overall transport from three cylindrical pockets.

D.3. The conductivity tensor element

The conductivity tensor is computed by integrals over the Brillouin zone[40].

$$\sigma_{ij} = e^2 \int \frac{d\mathbf{k}}{4\pi^3} \tau(\varepsilon)\, \mathbf{v}_i(\mathbf{k}) \mathbf{v}_j(\mathbf{k}) \left(-\frac{\partial f}{\partial \varepsilon}\right)_{\varepsilon=\varepsilon(\mathbf{k})}, \tag{D.8}$$

where $\mathbf{v}_i(\mathbf{k}) = \frac{1}{\hbar}\frac{\partial \varepsilon(\mathbf{k})}{\partial k_i}$ is the group velocity, τ is the relaxation time, and f is the Fermi-Dirac distribution function. We will first evaluate the conductivity tensor element σ^* for a cylindrical pocket.

$$\sigma^* = \sigma_{xx} = e^2 \int \frac{d\mathbf{k}}{4\pi^3} \tau(\varepsilon)\, \mathbf{v}_x(\mathbf{k}) \mathbf{v}_x(\mathbf{k}) \left(-\frac{\partial f}{\partial \varepsilon}\right)_{\varepsilon=\varepsilon(\mathbf{k})}, \tag{D.9}$$

where

$$\mathbf{v}_x(\mathbf{k}) = \frac{1}{\hbar}\frac{\partial \varepsilon(\mathbf{k})}{\partial k_x} \tag{D.10}$$

$$= \frac{1}{\hbar}\frac{\partial}{\partial k_x}\left[\frac{\hbar^2\left(k_x^2 + k_y^2\right)}{2m^*}\right] \tag{D.11}$$

$$= \frac{1}{\hbar}\frac{2\hbar^2 k_x}{2m^*} \tag{D.12}$$

$$= \frac{\hbar k_x}{m^*}. \tag{D.13}$$

$$\implies \sigma^* = e^2 \int \frac{d\mathbf{k}}{4\pi^3} \tau(\varepsilon) \left(\frac{\hbar k_x}{m^*}\right)^2 \left(-\frac{\partial f}{\partial \varepsilon}\right)_{\varepsilon=\varepsilon(\mathbf{k})} \tag{D.14}$$

The integration over all of k-space is easiest in cylindrical coordinates with the z-axis orientated along the cylindrical axis.

$$\implies \sigma^* = e^2 \int\int\int \frac{r\,dr\,d\theta\,dz}{4\pi^3} \tau(\varepsilon) \left(\frac{\hbar r\cos\theta}{m^*}\right)^2 \left(-\frac{\partial f}{\partial \varepsilon}\right)_{\varepsilon=\varepsilon(r)} \tag{D.15}$$

$$= \frac{e^2\hbar^2}{4\pi^3 m^{*2}} \int_{r=0}^{\infty} dr\ \tau(\varepsilon)\, r^3 \left(-\frac{\partial f}{\partial \varepsilon}\right)_{\varepsilon=\varepsilon(r)} \int_{\theta=0}^{2\pi} d\theta \cos^2\theta \int_{z=0}^{l} dz \tag{D.16}$$

$$= \frac{e^2\hbar^2 l}{4\pi^2 m^{*2}} \int_{r=0}^{\infty} dr\ \tau(\varepsilon)\, r^3 \left(-\frac{\partial f}{\partial \varepsilon}\right)_{\varepsilon=\varepsilon(r)} \tag{D.17}$$

The energy ε is directly related to r through the $\varepsilon - k$ relationship (Eq. D.2).

$$r = \sqrt{\frac{2m^*}{\hbar^2}}\varepsilon^{1/2} \implies dr = \frac{1}{2}\sqrt{\frac{2m^*}{\hbar^2}}\varepsilon^{-1/2}d\varepsilon \tag{D.18}$$

$$\implies \sigma^* = \frac{e^2\hbar^2 l}{4\pi^2 m^{*2}} \int_{\varepsilon=0}^{\infty} \left(\frac{1}{2}\sqrt{\frac{2m^*}{\hbar^2}}\varepsilon^{-1/2}d\varepsilon\right) \tau(\varepsilon) \left(\sqrt{\frac{2m^*}{\hbar^2}}\varepsilon^{1/2}\right)^3 \frac{-\partial f}{\partial \varepsilon} \tag{D.19}$$

$$= \frac{e^2\hbar^2 l}{4\pi^2 m^{*2}} \int_0^{\infty} \frac{1}{2} \left(\sqrt{\frac{2m^*}{\hbar^2}}\right)^4 \left(\varepsilon^{1/2}\right)^2 \tau(\varepsilon) \frac{-\partial f}{\partial \varepsilon} d\varepsilon \tag{D.20}$$

$$\boxed{\sigma^* = \frac{e^2 l}{2\pi^2\hbar^2} \int_0^{\infty} \varepsilon\, \tau(\varepsilon) \frac{-\partial f}{\partial \varepsilon} d\varepsilon} \tag{D.21}$$

Provided an expression for the relaxation time τ is given, we now have an expression for the conductivity tensor element σ^*.

D.4. The Seebeck tensor element

By calculating the conductivity tensor element σ^*, we are now able to infer the Seebeck tensor element α^*. The Seebeck coefficient is the ratio of two transport integrals. The numerator is the conductivity convoluted with $(\varepsilon - \mu)$, which is ν^*. The denominator is expressly conductivity. There is an addition factor of $1/eT$ that comes from the numerator[40].

$$\boxed{\alpha^* = \frac{1}{eT} \frac{\int_0^{\infty} \varepsilon(\varepsilon - \mu)\, \tau(\varepsilon) \frac{-\partial f}{\partial \varepsilon} d\varepsilon}{\int_0^{\infty} \varepsilon\, \tau(\varepsilon) \frac{-\partial f}{\partial \varepsilon} d\varepsilon}} \tag{D.22}$$

We now have equations for commonly measured transport coefficient (conductivity and Seebeck) from a cylindrical carrier pocket.

D.5. Density of states and carrier concentration

The number of states N in a cylindrical volume of k-space is

$$N = 2\frac{\pi l r^2}{(2\pi)^3}, \tag{D.23}$$

where r is the radius of the cylinder and l is its length. We have expressly included the electron spin degeneracy. With the $\varepsilon - k$ relationship (Eq. D.2) we convert radius to energy:

$$\implies N = \frac{2\pi l}{(2\pi)^3} \frac{2m^*\varepsilon}{\hbar^2} \tag{D.24}$$

$$= \frac{2lm^*}{(2\pi)^2 \hbar^2} \varepsilon. \tag{D.25}$$

The density of states $\mathcal{N}$ is the number of states dN within an energy window $d\varepsilon$.

$$\boxed{\mathcal{N}(\varepsilon) = \frac{dN}{d\varepsilon} = \frac{lm^*}{2\pi^2\hbar^2}} \tag{D.26}$$

The density of states for a cylindrical pocket is independent of energy, which is like the density of states for a 2D, quantum-confined system. The convolution of $\mathcal{N}$ with the Fermi-Dirac distribution function determines the number of carriers n.

$$n = \int_0^\infty \mathcal{N}(\varepsilon) f(\varepsilon) \, d\varepsilon \tag{D.27}$$

$$= \int_0^\infty \frac{lm^*}{2\pi^2\hbar^2} f(\varepsilon) \, d\varepsilon \tag{D.28}$$

$$\boxed{n = \frac{lm^*}{2\pi^2\hbar^2} \int_0^\infty f(\varepsilon) \, d\varepsilon} \tag{D.29}$$

D.6. Carrier relaxation time

The goal of this section is to derive an energy-dependent relaxation time in a deformation potential framework from Fermi's golden rule. Fermi's golden rule determines the transition frequency W from initial state $\mathbf{k}$ to final state $\mathbf{k}'$. Each initial and final state are connected by a matrix element M, and energy must be conserved.

$$W_{\mathbf{k},\mathbf{k}'} = \frac{2\pi}{\hbar} \left| M_{\mathbf{k},\mathbf{k}'} \right|^2 \delta(E_{\mathbf{k}} - E_{\mathbf{k}'}) \tag{D.30}$$

The matrix element M is represented as a convolution of the initial and final states with a perturbing potential V, which is (in general) position ($\mathbf{r}$) dependent. The initial and final states are represented as plane waves

$\left(|\mathbf{k}\rangle \leftrightarrow e^{i\mathbf{k}\cdot\mathbf{r}}\right)$.

$$M_{\mathbf{k},\mathbf{k}'} = \langle \mathbf{k}'|H'|\mathbf{k}\rangle = \int V(\mathbf{r}) e^{i\left(\mathbf{k}-\mathbf{k}'\right)\cdot\mathbf{r}} dV \tag{D.31}$$

Each final state $\mathbf{k}'$ additively contributes to the total scattering frequency Γ for a particular initial state $\mathbf{k}$; the energy-conserving δ-function in Eq. D.30 heavily restricts the number of allowed final states $\{\mathbf{k}'\}$. In addition, scattering events are weighed by a forward scattering factor. The scattering frequency is inversely related to the relaxation time τ.

$$\Gamma(\mathbf{k}) = \frac{1}{\tau(\mathbf{k})} = \int \frac{d\mathbf{k}'}{(2\pi)^3} W_{\mathbf{k},\mathbf{k}'} \left(1 - \hat{\mathbf{k}}\cdot\hat{\mathbf{k}}'\right) \tag{D.32}$$

$$= \frac{2\pi}{\hbar} \int \frac{d\mathbf{k}'}{(2\pi)^3} \left|M_{\mathbf{k},\mathbf{k}'}\right|^2 \left(1 - \hat{\mathbf{k}}\cdot\hat{\mathbf{k}}'\right) \delta(E_{\mathbf{k}} - E_{\mathbf{k}'}) \tag{D.33}$$

The allowed final states lie on the same isoenergy surface as the initial state (Fermi surface, S). In addition, when scattering is by non-polar phonons, the matrix element squared is proportional to the phonon wavevector, which induces the transition ($|M|^2 \sim q = \left|\mathbf{k}' - \mathbf{k}\right|$)[90].

$$\frac{1}{\tau(\mathbf{k})} \sim \frac{2\pi}{\hbar} \int_S \frac{d\mathbf{k}'}{(2\pi)^3} q \left(1 - \hat{\mathbf{k}}\cdot\hat{\mathbf{k}}'\right) \tag{D.34}$$

However, at finite temperature, the occupation of phonons is described by the Bose-Einstein distribution function $n_q(q) = 1/\left(e^{E(q)/kT} - 1\right)$. The distribution function weights each individual scattering event (from the initial state $\mathbf{k}$ to the final state $\mathbf{k}'$) by the number of phonons which can cause that transition.

$$\frac{1}{\tau(\mathbf{k})} \sim \frac{2\pi}{\hbar} \int_S \frac{d\mathbf{k}'}{(2\pi)^3} n_q q \left(1 - \hat{\mathbf{k}}\cdot\hat{\mathbf{k}}'\right) \tag{D.35}$$

With knowledge of the electron Fermi surface (which sets $\{\mathbf{k}'\}$, the set of final states) and the phonon dispersion (which sets n_q, the phonon occupation), the relaxation time can be computed numerically.

$$\boxed{\frac{1}{\tau(\mathbf{k})} \sim \sum_{\{\mathbf{k}'\}\in S} n_q q \left(1 - \hat{\mathbf{k}}\cdot\hat{\mathbf{k}}'\right)} \tag{D.36}$$

Scattering times were computed with Equation D.36 for spherical and cylindrical Fermi surfaces. A Debye phonon dispersion ($\hbar\omega = v_s q$) was used to illustrate how the shape of the Fermi surface impacts the temperature

dependence of the relaxation time. The results are shown in Figure D.1. At very low temperatures, both Fermi surfaces show Block T^5 behavior in the relaxation time. However, near 10 K, the two relaxation times diverge from one another. The scattering frequency rises faster in the cylindrical (2D) case, because additional scattering states along the Fermi surface became accessible in this temperature range, while the final states in the spherical (3D) case are all accessible (because the Fermi surface is not elongated). This model predicts that the T^2 behavior in the cylindrical case should become T^1 at very high temperatures.

The temperature dependencies of relaxation times are directly controlled through the occupation function n_q. However, it is not immediately obvious what this temperature dependency is, because the occupation is a complicated function. The description is significantly simplified by decoupling the occupation statistics into two terms, following the discussion of T^2 resistivity in Bi[100]. These two terms represent the fact that low energy phonons are increasing their occupation linearly (n_{q}), while higher energy phonons are only just becoming occupied at higher temperatures (n_{final}). For a Debye model dispersion, the front of the final states moves linearly with temperature ($q_{\mathrm{thermal}} = kT/v_s$, where v_s is the speed of sound). Decoupling the occupation statistics into these two terms illustrates how finite temperature influences the relaxation time (see the discussion of temperature-squared resistivity in the main text). These terms make it clear why low-dimensional Fermi surfaces could have additional temperature dependencies in the relaxation time at elevated temperatures (from the n_{final}).

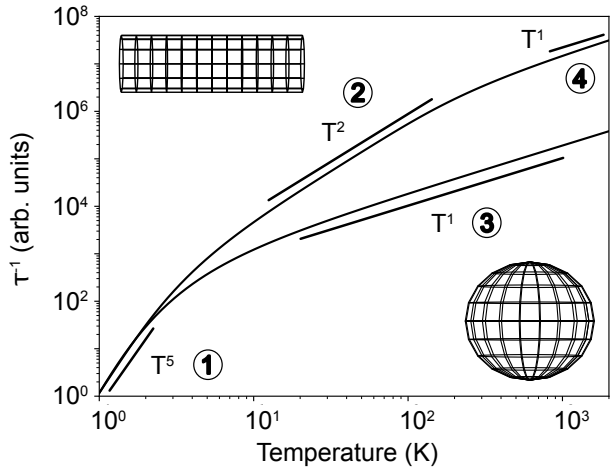

Figure D.1. The scattering frequency for electrons on 3D and 2D Fermi surfaces are qualitatively different and explained by the same scattering model. **1)** At low temperatures both types of electrons follow the Block T^5 law. **2)** When the phonon Bose sphere exceeds the radius of the 2D Fermi surface but is smaller than Fermi surface length, T^2 behavior is observed. **3)** When the phonon Bose sphere exceeds the radius of the 3D Fermi surface, T^1 behavior is observed. **4)** The 2D case is also expected to recover T^1 behavior when all phonon modes are saturated.

APPENDIX E

Meta-Stable Half-Heusler Electronic Structures

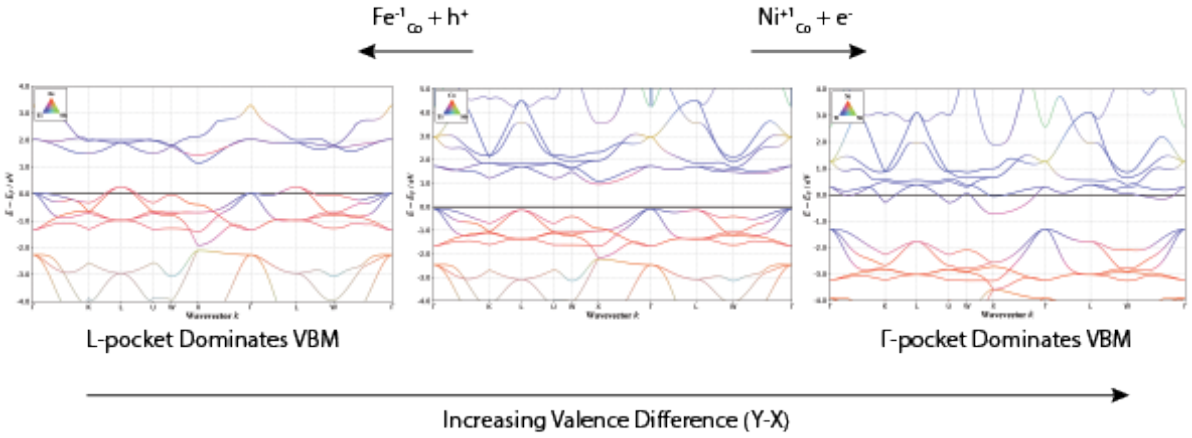

Figure E.1. Calculating metastable 17e- and 19e- compounds confirms that valence difference rules control the relative positions of the valence band Γ- and L-energies. Substituting Fe on the Co site of TiCoSb dopes the material p-type and raises the energy of the L-point relative to Γ. Substituting Ni on the Co site dopes the material n-type and raises the energy of the Γ-point relative to the L-point. The relative energies of Γ and L appear to be primarily controlled by the valence difference between the X- and Y-sites and not affected by the location of the Fermi level. This virtual experiment indicates that the effect of dopants on the band structure can be predicted from the valence difference rule.

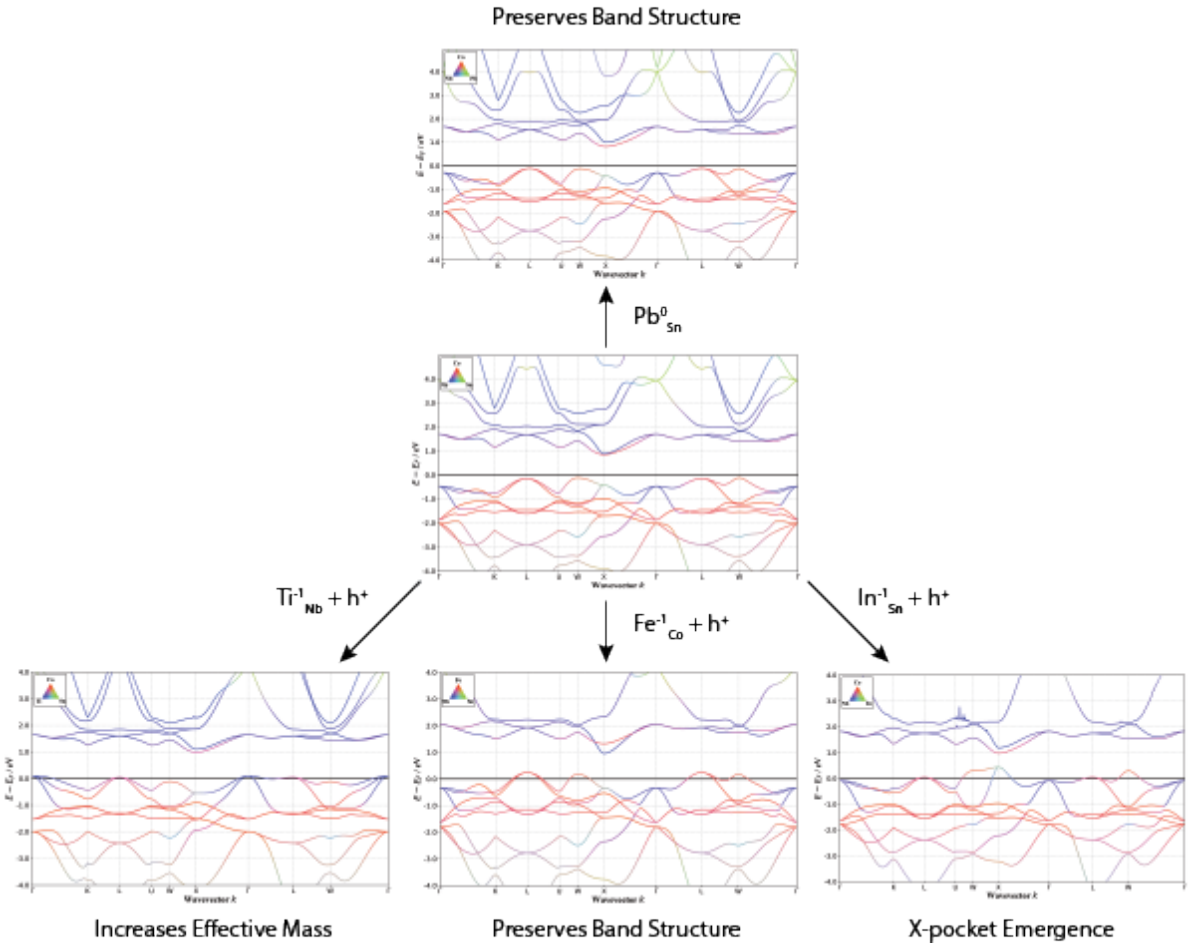

Figure E.2. We explore the effects of site-substitution on NbCoSn. The iso-valent substitution of Pb on the Sn site does not significantly affect the band structure. Solid-solutions between the Sn- and Pb-analogs could lower the thermal conductivity through phonon alloy scattering without significantly impacting the electronic structure. P-type, aleo-valent substitutions on each of the different sites have different effects on the electronic structure. Ti on the Nb-site raises the energy of the Γ point per the valence difference rule, and increases the effective mass of the hole-pockets. Substituting Fe on the Co-site raises the energy of the L-point, but has less of an impact on the electronic structure compared to substituting Ti. In on the Sn-site has remarkable changes to the electronic structure, raising the energy of the X-point. This is a class of electronic structure not observed in the stable 18e- materials, so In may be an interesting dopant to consider. Experiments should investigate the effects of different site-dopings on the thermoelectric transport properties.

APPENDIX F

Outlook for the Thermoelectric Performance of SrTiO3

Analyzing the mean free path of electrons in single crystals of $SrTiO_3$ indicates that nanostructuring could be an effective strategy for improving the thermoelectric performance, even near room temperature. In this analysis, the mean free path ($l = v \cdot \tau$) is the product of the average particle velocity (v) and relaxation time (τ), and should be shorter than any micro-structural feature (the grain size) introduced to lower the lattice thermal conductivity. The relaxation time for electrons in single crystals (which is dominated by electron-phonon scattering) is near ∼10 fs at 300 K[89], and the average electron velocity can be estimated from the thermal energy ($v = \sqrt{3k_bT/m^*}$), also at 300 K. For electrons with an inertial effective mass of 0.5 m_e[176] (estimated from the curvature of the band structure), the mean free path is estimated to be ∼1.5 nm. Therefore, the linear density of micro-structural defects (grain boundaries) should be much less than ∼1/nm to avoid lowering the electron mobility[177].

The thermal conductivity of La-doped $SrTiO_3$ can be as low as 1.2 W/mK (at room temperature) when the grain size is 24 nm[22]. Since 24 nm is much larger than the mean free path of electrons, ∼1 W/mK might be achieved in nanostructured samples without sacrificing the electron mobility (so long as there is no grain boundary potential and depletion of free carriers at the boundary). However, the lattice thermal conductivity should not be expected to be less than ∼1 W/mK, because this is near the diffusive limit of the lattice thermal conductivity (an estimation of the minimum thermal conductivity[178]) as estimated from the number-density of atoms (n) and the transverse (v_t) and longitudinal (v_l) speeds of sound ($\kappa_{diff} \sim 0.76n^{2/3}k_b\frac{1}{3}(2v_t + v_l) \sim 1$ W/mK). The transverse and longitudinal speeds of sound are ∼4900 and ∼7900 m/s, respectively, and do not change significantly with electronic doping[11].

The performance outlook of $SrTiO_3$ can be estimated from the power factors measured in single crystals[7] and the minimum lattice thermal conductivity estimate using an effective mass model[1]. This analysis (at a carrier concentration optimized for 450 K and a constant lattice thermal conductivity) indicates that the average zT between 300 and 1000 K would be higher than 0.5—with a peak zT approaching 0.7—in the diffusive limit of the

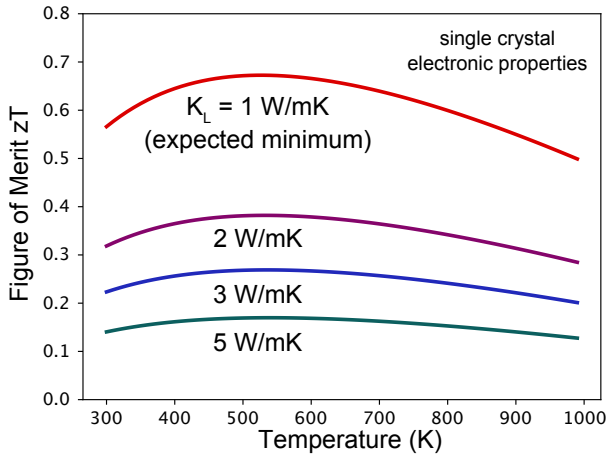

Figure F.1. The figure of merit of $SrTiO_3$ could be higher than 0.5 at room temperature if polycrystalline samples can be synthesized with both electronic properties similar to single crystals and low lattice thermal conductivities. Samples with a grain size of ∼20 nm should achieve ∼1 W/mK[22] and not degrade the electron mobility, since the electron mean free path (limited by phonons at 300 K) is ∼1.5 nm.

lattice thermal conductivity (Figure F.1). However, simultaneously achieving low lattice thermal conductivity and high electronic performance will require precise control of the interface structure, so as to minimize the role of grain boundary resistance. Given the success of grain boundary engineering to control grain boundary depletion regions, the outlook for $SrTiO_3$ as a nanostructured thermoelectric material is promising, even near room temperature.

APPENDIX G

Calculation Methods

G.1. Calculations of SrTiO3

A plane-wave electronic structure calculation [137] was projected onto Wannier functions for three sets of isolated bands [179] with Wannier90. The electronic structure calculation was carried out using a plane-wave basis (cutoff energy of 520 eV) in the VASP package with a 12x12x12 Monkhorst-pack k-point mesh, PAW psudopotential, and PBE functional. The nine top-most valence bands were initially projected onto Oxygen-p orbitals, conduction bands 1-3 onto Titanium-d t_{2g} orbitals, and conduction bands 4-5 onto Titanium-d e_g orbitals. The obtained Wannier functions were visualized using crystallographic software. [180,181] Analytic transport coefficients were derived for a cylindrical band model using the Boltzmann transport framework. [40] Tensor quantities for conductivity and the Seebeck coefficient were obtained and implemented numerically in Python utilizing a package that implements precise approximations to the Fermi-Dirac integrals. [182] The Boltzmann transport coefficients were used to extract the Seebeck mass and relaxation time. The relaxation time model was implemented numerically in Python. Temperature-dependent convergence with k-point mesh density was obtained. The shape of the model relaxation time was set by the relative scattering strength of acoustic to optical phonons and the scale by the absolute magnitude of the acoustic scattering strength.

G.2. Calculations of half-Heuslers

Electronic structure calculations were carried out using a plane-wave basis (cutoff energy of 520 eV) in the VASP package with with PAW psudopotentials and the PBE functional. [137] The structural degrees of freedom were relaxed using 12x12x12 Monkhorst-Pack k-point meshes, followed by relaxation of the electronic degrees of freedom using 15x15x15 meshes. Finally, a non-self-consistent field calculation with 20x20x20 gamma-centered meshes was used to calculate quantitatively accurate density of states with tetrahedron smearing. [183] In addition, effective masses were calculated using the BoltzTraP package. This set of calculations were performed with

the atomate workflow software. The projected density of states were quantified in the matminer package using the SiteDOS featurizer.[173] The Fermi surfaces of the electronic structures were visualized using the pymatgen package.[184] The most important atomic features for modeling the Γ-L energy offset were determined by ridge-regression.[185]

Vita

Published Works and Contributions

[1] Dylla, Maxwell T., Alexander Dunn, Shashwat Anand, Anubhav Jain, and Gerald Jeffrey Snyder. "Chemical Guidelines for Engineering Valley Degeneracy in p-type half-Heusler Thermoelectric Materials." In preparation.

Developed calculation work-flow, developed analysis method, analyzed calculation results, wrote manuscript.

[2] Dylla, Maxwell T., Jimmy Jiahong Kuo, Ian Witting, and Gerald Jeffrey Snyder. 2019. "Grain Boundary Engineering Nanostructured SrTiO 3 for Thermoelectric Applications." Advanced Materials Interfaces, May, 1900222. https://doi.org/10.1002/admi.201900222.

Scraped the data, analyzed data, and wrote the manuscript.

[3] Dylla, Maxwell Thomas, Stephen Dongmin Kang, and G. Jeffrey Snyder. 2019. "Effect of Two-Dimensional Crystal Orbitals on Fermi Surfaces and Electron Transport in Three-Dimensional Perovskite Oxides." Angewandte Chemie 131 (17): 5557-66. https://doi.org/10.1002/ange.201812230.

Developed the model, performed calculations, scraped data, analyzed results, and wrote the manuscript.

[4] Kang, Stephen Dongmin, Maxwell Dylla, and G. Jeffrey Snyder. 2018. "Thermopower-Conductivity Relation for Distinguishing Transport Mechanisms: Polaron Hopping in CeO 2 and Band Conduction in SrTiO 3." Physical Review B 97 (23). https://doi.org/10.1103/PhysRevB.97.235201.

Developed the Fermi-surface model.

[5] Miller, Samuel A., Maxwell Dylla, Shashwat Anand, Kiarash Gordiz, G. Jeffrey Snyder, and Eric S. Toberer. 2018. “Empirical Modeling of Dopability in Diamond-like Semiconductors.” Npj Computational Materials 4 (1). https://doi.org/10.1038/s41524-018-0123-6.

Helped develop the modeling procedures and reviewed the manuscript.

[6] Cook, Seyoung, Maxwell T. Dylla, Richard A. Rosenberg, Zachary R. Mansley, G. Jeffrey Snyder, Laurence D. Marks, and Dillon D. Fong. 2018. “The Vacancy-Induced Electronic Structure of the SrTiO3 Surface.” Advanced Electronic Materials, November, 1800460. https://doi.org/10.1002/aelm.201800460.

Developed the model, analyzed the results, assisted in writing the manuscript.

[7] Ward, Logan, Alexander Dunn, Alireza Faghaninia, Nils E.R. Zimmermann, Saurabh Bajaj, Qi Wang, Joseph Montoya, et al. 2018. “Matminer: An Open Source Toolkit for Materials Data Mining.” Computational Materials Science 152 (September): 60-69. https://doi.org/10.1016/j.commatsci.2018.05.018.

Helped develop the code-base.

[8] Zevalkink, Alex, David M. Smiadak, Jeff L. Blackburn, Andrew J. Ferguson, Michael L. Chabinyc, Olivier Delaire, Jian Wang, et al. 2018. “A Practical Field Guide to Thermoelectrics: Fundamentals, Synthesis, and Characterization.” Applied Physics Reviews 5 (2): 021303. https://doi.org/10.1063/1.5021094.

Helped develop the section on Landauer theory for bulk-systems.

[9] Zhang, Qihao, Zhenxing Zhou, Maxwell Dylla, Matthias T. Agne, Yanzhong Pei, Lianjun Wang, Yunshan Tang, et al. 2017. “Realizing High-Performance Thermoelectric Power Generation through Grain Boundary Engineering of Skutterudite-Based Nanocomposites.” Nano Energy 41 (November): 501-10. https://doi.org/10.1016/j.nanoen.2017.10.003.

Analyzed the data, modeled the thermal conductivity.

[10] Zong, Peng-an, Riley Hanus, Maxwell Dylla, Yunshan Tang, Jingcheng Liao, Qihao Zhang, G. Jeffrey Snyder, and Lidong Chen. 2017. "Skutterudite with Graphene-Modified Grain-Boundary Complexion Enhances ZT Enabling High-Efficiency Thermoelectric Device." Energy & Environmental Science 10 (1): 183-91. https://doi.org/10.1039/C6EE02467J.

Developed the series circuit model.